UNIVERSIDADE D
COIMBRA

Henrique Daniel Galvão Martins Almeida

Studies of double electron capture in ^{124}Xe with the LUX-ZEPLIN detector

Dissertação no âmbito do Mestrado em Física, ramo de Física Nuclear e de Partículas orientada pelo Professor Doutor Alexandre Miguel Ferreira Lindote e pelo Professor Doutor Cláudio Frederico Pascoal da Silva e apresentada ao Departamento de Física da Faculdade de Ciências e Tecnologia.

Setembro de 2022

Studies of double electron capture in ^{124}Xe with the LUX-ZEPLIN detector

Henrique Daniel Galvão Martins Almeida

A thesis submitted for the degree of
Master in Physics

Department of Physics
University of Coimbra
Portugal

September 2022

Abstract

The pursuit for the most elusive particle ever searched for, dark matter, requires an experiment with a very low background. Therefore, besides these studies, it is possible to look for other rare processes. An excellent example of this kind of search is the one carried out during this thesis for the double electron capture of the ^{124}Xe isotope. We studied the normal decay mode, during which two neutrinos are emitted. This represents the first step for the search of neutrinoless processes, where no neutrinos are emitted, which, if true, would prove that neutrinos are Majorana particles. The Majorana nature of neutrinos could help solve two main concerns in Particle Physics: the mass hierarchy problem and the fact that neutrinos are massive, which can not be explained by the Standard Model (SM).

In this work, we use data from the LUX-ZEPLIN (LZ) experiment to search for this decay. We will start by understanding how this type of detector works, followed by the analysis of detailed Monte Carlo simulations to construct a background model and to predict the required time to reach the discovery potential (5σ) for the KK mode (simultaneous electron capture from the K shell), as well as the observation (3σ) and discovery potential for the KL mode (electron capture from the K and L shells). Using the best estimates for the backgrounds during the Science Run 1 (SR1), we obtain that the LZ experiment will be able to claim a discovery in the KK mode after 44 days of exposure, whereas it could claim an observation and a discovery in the KL mode after 117 and 329 days, respectively. However, the LZ experiment will not be able to observe the LL mode during its 1000 days of exposure. Finally, after doing a removal time study following the production of ^{125}I isotope, a very important background for our search, it was established that the last 50 days of the SR1 were safe to use for our work. Using that data set with 46.7 days of live time, we were able to obtain the half-life for this decay, $T_{1/2}^{2\nu 2EC} = (1.4 \pm 0.1(stat.) \pm 0.2(sys.)) \times 10^{22}$ yr, with a statistical significance of 6.1σ.

Keywords: The Standard Model of particles physics, the LUX-ZEPLIN experiment, double electron capture, rare decays, neutrinoless processes, double beta decay, neutrino nature.

Resumo

A procura pela partícula mais elusiva de sempre, matéria escura, requer uma experiência com um fundo muito reduzido. Portanto, para além destes estudos, outros processos raros são também possíveis de procurar. Um exemplo excelente deste tipo de procura é este realizado durante esta tese para a captura electrónica dupla para o isótopo ^{124}Xe, onde dois neutrinos são emitidos neste processo. Isto representa o primeiro passo para uma procura por processos sem emissao de neutrinos, que, se observados, irão provar que os neutrinos são partículas de Majorana. A natureza de Majorana dos neutrinos pode ajudar a resolver dois problemas fundamentais da Física de Partículas: o problema da hierarquia de massas e o facto de os neutrinos terem massa, que o Modelo Padrão não consegue explicar.

Neste trabalho, usamos os dados provenientes da experiência LZ na procura por este decaimento. Iremos começar por perceber como é que este tipo de detector funciona, seguido pela análise de simulações de Monte Carlo do detector que foram usadas para gerar um modelo de background e para prever o tempo necessário para alcançar um nível estatístico de descoberta (5σ) para o modo KK (captura simultânea de eletrões da camada K), bem como os níveis estatísticos de observação (3σ) e descoberta para o modo KL (captura de eletrões das camadas K e L). Usando a melhor estimativa para os backgrounds durante a primeira campanha de aquisição de dados da experiência (SR1), estimamos que a experiência LZ será capaz de alegar uma descoberta no modo KK depois de 44 dias de exposição, enquanto que para alegar uma observação e uma descoberta no modo KL serão necessários 117 e 329 dias, respectivamente. Contudo, a experiência de LZ não será capaz de observar o modo LL durante os seus 1000 dias. Finalmente, depois de fazermos um estudo do tempo de remoção do isótopo ^{125}I gerado durante a calibração do detector com neutrões, um fundo bastante importante para a nossa procura, estabeleceu-se que os últimos 50 dias da SR1 eram seguros para usar no nosso trabalho. Usando esse conjunto de dados com 46.7 dias de tempo efectivo, conseguimos obter o tempo de meia-vida para este decaimento, $T_{1/2}^{2\nu 2EC} = (1.4 \pm 0.1(stat.) \pm 0.2(sys.)) \times 10^{22}$ yr, com uma significância estatística de 6.1σ.

Palavras-chave: O Modelo Padrão de física de partículas, a experiência de LUX-ZEPLIN, captura electrónica dupla, decaimentos raros, processos sem emissão de neutrinos, decaimento beta duplo, natureza dos neutrinos.

Acknowledgements

I would like to begin by thanking my supervisors, Dr. Alexandre Lindote and Dr. Cláudio Silva, for always elucidating me in every question I raised and for their patience in doing so. Thank you for all the insight in these difficult topics and for the hard work that they have to make so that I was able to write this dissertation.

I would also like to thank the Dark Matter group from the LIP-Coimbra for their help during the realization of this dissertation. They are a very welcoming group with very smart and hard-working people always able to help when it is needed.

To my grandparents, Isilda and António, a very special thank you. I will always be grateful for the way that they also raised me and love me during my life.

I would like to thank my parents, Fátima and António, my path until this point was impossible if were not for you. You help me in every step, understood me and you always give me confidence, if not for this I was not able to arrive here.

A thank you is not enough for what I owe to my brother, David, you have always been my role model growing up and you were always there for me. You showed me what is right and wrong and I love growing up next to you, it was one of the happiest times in my life.

Finally, to you Susana I hope to thank you for the rest of my life. I can not put in words what you mean to me and how did you help me not only during this dissertation but also during all these years we have been together. Before you found me I had lost my love and interest in Physics, but with you I found that spark that I had when I was a little boy. You encouraged me and made me a better man during these 5 years, and I can not ask for anyone better. I just want to say: Thank you.

Contents

Abstract i

Resumo iii

Acknowledgements v

Contents viii

List of Figures xv

List of Tables xvi

Acronyms xvii

1 Introduction 1

2 Standard Model, Neutrino Physics and Double Beta Decays 3
- 2.1 The Standard Model . . . 3
- 2.2 Neutrino Physics . . . 6
- 2.3 Double Beta Decay . . . 13
  - 2.3.1 $2\nu\beta^-\beta^-$ decay . . . 17
  - 2.3.2 $2\nu\beta^+\beta^+$ decay . . . 17
  - 2.3.3 $2\nu ECEC$ decay . . . 17
  - 2.3.4 $2\nu EC\beta^+$decay . . . 18
- 2.4 Neutrinoless Double Beta Decay . . . 18
  - 2.4.1 $0\nu\beta^-\beta^-$ decay . . . 20
  - 2.4.2 $0\nu\beta^+\beta^+$ decay . . . 21
  - 2.4.3 $0\nu ECEC$ decay . . . 21
  - 2.4.4 $0\nu EC\beta^+$decay . . . 22

3 The LUX-ZEPLIN Experiment 23
- 3.1 Particle interaction in a liquid Xenon TPC . . . 23
- 3.2 The LZ detector . . . 28
  - 3.2.1 Dual-phase TPC . . . 30
  - 3.2.2 Xenon Skin . . . 31
  - 3.2.3 Outer detector . . . 32
- 3.3 Detector calibrations . . . 34
  - 3.3.1 Internal sources . . . 35
  - 3.3.2 Gamma-ray external sources . . . 35

3.3.3 Neutron sources . . . 36
3.4 Science Run 1 . . . 38

4 Background in the LZ experiment **39**
4.1 Signal of the ^{124}Xe isotope . . . 39
4.2 Background overview . . . 42
4.2.1 External backgrounds . . . 42
4.2.2 Internal backgrounds . . . 45
4.2.3 Background simulations . . . 48
4.3 The Rolke Method . . . 51
4.4 Sensitivity studies . . . 53

5 The ^{125}I isotope as a background for the 2ν2EC ^{124}Xe decay search **60**
5.1 Signal of the ^{125}I isotope . . . 60
5.2 The ^{125}I isotope in the TPC . . . 61
5.2.1 Event selection . . . 62
5.2.2 Population selection . . . 63
5.2.3 Removal time . . . 66
5.2.4 Search period selection . . . 68
5.3 Position distribution of the ^{125}I isotope in the TPC . . . 69

6 2νECEC decay search for the ^{124}Xe isotope **72**
6.1 Background model . . . 72
6.2 ^{124}Xe double electron capture (KK mode) search . . . 75

7 Conclusion **79**

References **81**

List of Figures

2.1 Pictorial representation of the Standard Model of Elementary Particles. On the left, are presented the three generations of matter, the fermions, while the force carriers, bosons, are represented on the right. The constituents of matter are further subdivided in two groups: quarks, in purple, and leptons, in green. The force carriers are subdivided considering their spin value. Particles with spin equal to one are vector bosons, represented in red, whereas the ones with spin equal to zero are scalar bosons. In this last category we have the particle that provides mass to the remaining particles, the Higgs boson. Figure from [5]. 4

2.2 Quark model representation of an atom. Protons and neutrons, constituents of the nucleus, are made of up quarks (smallest yellow circles) and down quarks (green circles). Protons have two up quarks and one down quark, while neutrons have two down quarks and one up quark. These quarks are held together by the strong force, which is mediated by the gluon. Around these particles we have another elementary particle, the electron (big orange circles). Figure from [15]. 5

2.3 Comparison between the observed beta decay spectrum, in black, and the expected spectrum if that decay occurred without the emission of an neutrino (or antineutrino in the case of the beta minus decay), in red. Figure from [26]. 7

2.4 Solar neutrinos flux from ^{8}B. Through the three neutrino reactions in Sudbury Neutrino Observatory (SNO), was obtained this flux for the neutrinos with muon and tau flavors, identified by $\phi_{\mu\tau}$, as a function of the neutrino flux with electron flavor, denoted by ϕ_e. The diagonal dashed lines show the total ^{8}B flux as predicted by the Standard solar model. Figure from [43]. 10

2.5 Distinct possibilities in the neutrino mass hierarchy problem: on the left, we have the normal ordering, where m_3 is greater than m_2, whereas on the right we have the inverted ordering with m_3 lighter than m_2 (the mass is growing upward). Each mass eigenstate is a mixing of different neutrino flavors, where the electron, muon and tau flavors are represented by the red, orange and blue colors, respectively. Figure from [53]. 13

2.6 An electron shell diagram: through this, it is possible to understand the reason for the higher likelihood of the electron absorbed during electron capture coming from the shells closest to the nucleus. Figure from [62]. . 14

2.7 Representation of the mass obtained using the semi-empirical mass formula as a function of the proton number, Z. The two lines identify the two mass parabolas for isobaric nuclei, with an even mass number, A, for odd-odd (O-O) and even-even (E-E) nuclei. An odd-odd nucleus is constituted by an odd number of neutrons and an odd number of protons. In the even-even case, we have an even number of neutrons and an even number of protons. Due to the neighbour nuclei masses, Double Beta Decay can occur from (a) to (c) and from (d) to (c). However the atom in (a) can not decay to the atom in (b), by beta minus decay, since it is not energetically accessible. Figure from [66]. 16

2.8 Feynman diagrams for the $2\nu\beta^-\beta^-$, on the left, and for the $0\nu\beta^-\beta^-$, on the right. In the latter, because in that case neutrinos are Majorana particles and so they are their own antiparticles, there are no emission of neutrinos. Figure from [71]. 18

2.9 Effective Majorana mass as a function of the lightest neutrino mass at 99.7% CL, comparing inverted ordering, in blue, and normal ordering, in red, of the three active neutrinos. The green band represents the 90% CL bounds from KamLAND-Zen. Figure from [75]. 19

2.10 The energy spectrum for the $2\nu\beta^-\beta^-$ and the $0\nu\beta^-\beta^-$ decays: an event excess in the end of the spectrum represents the signature of the $0\nu\beta^-\beta^-$ decay with the two emitted electrons carrying the entire Q-value energy. Figure from [77]. 20

2.11 Decay scheme of ^{124}Xe. The other Double Beta Decay modes other than neutrinoless double electron capture decay most likely to the ground state of ^{124}Te, whereas in the resonant neutrinoless double electron capture the ^{124}Xe nucleus decays to the excited state of ^{124}Te with (2790.41$\pm$0.09) keV. Figure from [79]. 21

3.1 Schematic representation for the processes that occur after an interaction in xenon. The inner transformation that can happen in each of the processes leading to the scintillation light and to the ionization electrons is also represented. From the three possible processes only excitation and ionization can be detected, so the energy dissipated by heat is lost in these detectors. Figure from [86]. 24

3.2 Representation of the working principle of a dual-phase Time Projection Chamber (TPC). From the interaction of an incoming particle with a xenon atom, a prompt scintillation signal, S1, will be measured. Alongside that, ionization electrons will be also produced and will drift in the upward direction due to the electric field. They will drift until they arrive to the liquid/gas frontier, where a stronger electric field will extract them to the gas phase. They will accelerate in the gas phase creating electroluminescence, and thus the S2 signal. Figure from [90]. 26

3.3 Representation of $\log_{10}$(S2/S1) as a function of the S1 signal obtained with LUX calibration. In the a) graph the electron recoil (ER) response was calibrated using a tritium source, whereas in the b) graph it is shown the nuclear recoil (NR) calibration using a deuterium-deuterium neutron source. The median for both bands are represented with solid line, blue for the ER and red for the NR. The dashed lines indicate the 80% population contours of the bands, again with the same colors as the median. The vertical gray lines are the contours of constant energy deposition, whereas the pink line represents the S2 threshold in that analysis. Figure from [90]. 27

3.4 Diagram of the LZ detector. The main xenon detector (TPC) and the skin are in the center observed by a total of 625 PhotoMultiplier Tubes (PMTs). They are surrounded by the outer detector in green and further by the water tank. Figure from [87]. 29

3.5 Fully assembled TPC with the four different grids identified. The two arrays of PMTs are represented, with the light purple representing the gaseous phase and the dark representing the liquid phase. The three different regions with different fields are also depicted. Figure from [88]. . . 30

3.6 Assembly of the PMTs in the lower side and dome skin regions. Figure from [90]. 32

3.7 Illustration of the outer detector, with its constituents: 3 vessels on the bottom and the 2 on top all in blue, the 4 larger vessels on the sides in green and finally water displacers in red. Figure from [90]. 33

3.8 Energy scale study as a function of the number of photons detected, for three different z values, using a ^{228}Th source for the outer detector on the left. Number of photons detected versus z position, using a ^{57}Co source in the skin. Figure from [90]. 36

3.9 Setup of the deuterium-deuterium neutron source with its two neutron conduits. Using the leaning conduit, the neutrons with 2.45 MeV go directly from the generator to the detector, on the left image. On the right, we have the alternative layout where the initial 2.45 MeV beam will be reflected in deuterium oxide, D_2O, thus resulting in 272 keV quasi monoenergetic neutrons. Figure from [90]. 37

4.1 Graphical representation of the stability band as a function of the number of protons and neutrons in blue, as well as the 1.5:1 and 1:1 ratios in green and red, respectively. Figure from [102]. 40

4.2 Representation of the decay chain for the ^{238}U (above) and for the ^{232}Th (below). It is illustrated their principal decay modes and their half-lives decay time. Figure from [105]. 43

4.3 Representation of the event rate as a function of energy caused by the proton-proton chain (blue) and from ^{7}Be (red). In dashed lines the contribution of electron neutrinos are shown, whereas the other flavors are in dotted lines. The total contribution is shown in the solid lines. Figure from [108] 44

4.4 Graphical representation of the $S2_b$ vs S1 signals before (left) and after (right) a calibration using a deuterium-deuterium neutron source: the color scale represents the correspondent event density. Populations of activated isotopes are visible after the neutrons calibration, as indicated in the figure. ^{131m}Xe is injected regularly as a calibration source, and is thus visible in both periods. 47

4.5 Different processing chains for the simulation used to generate data for the sensitivity analyses and Mock Data Challenges analysis. Figure from [84]. 48

4.6 Background rate for the individual components and total background with only the region of interest cut applied. Figure from [116]. 49

4.7 Spatial distribution of all ER backgrounds that get through both the single scatter and veto cuts, with energy less than 100 keV. The dashed black line identifies the fiducial region. Figure from [85]. 50

4.8 Background rate for the individual components and total background after all cuts applied. Figure from [116]. 51

4.9 The expected rate for the observed signal plus the background sources for the double electron capture of the ^{124}Xe isotope is represented as the black line. In blue, pink, and green it is depicted the expected individual signal for the LL, KL, and KK modes, respectively. It was used the same values as in the previous graph, 1.8 μBq/kg and 0.09 μBq/kg for the activities of ^{222}Rn, and ^{220}Rn, respectively, and 300 ppq g/g for the ^{nat}Kr/Xe concentration. 53

4.10 Time evolution for the 90% confidence level sensitivity, the observation potential, a statistical significance of 3σ, and discovery potential, a statistical significance of 5σ, for the 1000 days of exposure in the LZ experiment in the KK decay mode represented by the blue, green, and red lines. The bands, which have the same color as their lines, illustrate the uncertainty band at 68% of confidence level, that means a uncertainty of $\pm\sigma$. The dashed black line represents the half-life, measured by Xenon1T, for the KK mode. Its uncertainty is also depicted by the gray area. 54

4.11 Time evolution for the 90% confidence level sensitivity, the observation potential, a statistical significance of 3σ, and discovery potential, a statistical significance of 5σ, for the 1000 days of exposure in the LZ experiment in the KL decay mode represented by the blue, green, and red lines. The bands, which have the same color as their lines, illustrate the uncertainty band at 68% of confidence level, that means a uncertainty of $\pm\sigma$. The dashed black line represents the expected half-life for the KL mode, obtained through the method described in the main text. Its uncertainty is also depicted by the gray area. 55

4.12 Time evolution for the 90% confidence level sensitivity, the observation potential, a statistical significance of 3σ, and discovery potential, a statistical significance of 5σ, for the 1000 days of exposure in the LZ experiment in the LL decay mode represented by the blue, green, and red lines. The bands, which have the same color as its lines, illustrate the uncertainty band at 68% of confidence level, that means a uncertainty of $\pm\sigma$. The dashed black line represents the expected half-life for the LL mode, obtained through the method described in the main text. Its uncertainty is also depicted by the gray area. 56

4.13 Exposure time required for the LZ experiment to reach the discovery potentials for the KK mode, in blue, and the observation and discovery potentials for the KL modes, in green and red, respectively, as a function of the activity of the ^{222}Rn isotope. In the vertical dashed black line it is shown the best estimate, 3.2μBq/kg, for the activity of the ^{222}Rn isotope during the SR1 of the LZ experiment. 57

4.14 Exposure time required for the LZ experiment to reach the discovery potentials for the KK mode, in blue, and the observation and discovery potentials for the KL modes, in green and red, respectively, as a function of the activity of the ^{85}Kr isotope. The vertical dashed black line shows the best estimate, 0.144 ppt, for the activity of the ^{85}Kr isotope during the SR1 of the LZ experiment. The result from using 3.2 μBq/kg for the activity of the ^{222}Rn isotope is represented by the full lines, whereas the one obtained by using 1.8 μBq/kg for the activity of the same isotope is represented by the dashed lines. 59

5.1 Decay scheme of the ^{125}I isotope: ^{125}I decays to the 35.5 keV excited state of the ^{125}Te isotope with a half-life of 59.4 days, which in turn will decay, almost instantly, to its ground state. Figure from [125]. 61

5.2 Graphical representation of the $S2_b$ vs S1 signals after the calibration that used a deuterium-deuterium neutron source. The correspondent event density is also represented. 64

5.3 Graphical representation of the energy spectrum after the calibration that used a deuterium-deuterium neutron source. 64

5.4 Graphical representation of the $S2_b$ vs S1 signal after the calibration alongside of the 2σ cut to the iodine population in blue. 65

5.5 Graphical representation of the energy spectrum after the calibration, with the 2σ cut to the iodine population also represented in red. 65

5.6 Variation of the rate in the ^{125}I isotope region with time after the DD calibration. Exponential fit in orange using the parameters in Equation 5.4, which allowed us to discover the half-life of this removal using the getter and the background present in this region, as we can see in blue. The moments where the ^{125}I isotope is equal to, is 50%, and 10% of the background are also identified, and this happens after 15.5, 19.1, and 27.4 days, respectively. 66

5.7 Comparison between the rate in the ^{125}I isotope region before and after the DD calibration: the red line is the mean background before that calibration, and it shows that this value is higher than the value obtained for the end part of the events after the calibration. 67

5.8 Variation of the rate in the ^{125}I isotope region with time for intervals with 10 days starting at the end of SR1. Horizontal bars indicate the bin width, whereas the vertical ones indicate the error associated with the mean background value. The moment where the ^{125}I isotope is 10%, 5%, and 1% of the total background is represented in the red, black, and green dotted lines, respectively, whereas the end of the calibrations is in the blue dotted line. 68

5.9 Variation of the rate in the ^{125}I isotope region with time for intervals starting with 10 days and increasing 10 days steps until we reach the calibration point, starting at the end of SR1.The vertical lines represent the error associated with the mean background value. The moment where the ^{125}I isotope is 10%, 5%, and 1% of the total background is represented in the red, black, and green dotted lines, respectively, whereas the end of the calibration is in the blue dotted line. 69

5.10 Position distribution of the ^{125}I population inside of the detector as a function of the radial and vertical components. The data obtained throughout the SR1 were separated into 5 different intervals. The population obtained previously to the calibration is represented by the magenta crosses, whereas the population for the intervals up to 3.5 days, between 3.5 and 14 days, up to 14 days, and after 20 days is represented by the red down triangle, the blue square, the empty circle, and the grey diamond, respectively. The boundaries of the fiducial volume and the TPC are represented by the dotted black line, and by the blue line, respectively. 70

6.1 Graphical representation of the energy spectrum using the 5-day period after the calibration that used a deuterium-deuterium neutron source, in blue. The gaussian fit to the ^{125}I population is represented in magenta. . 73

6.2 Reconstructed energy spectrum of the best fit background model. Data points from the WIMP search are shown in black. The blue line shows the total summed background. Background components are shown in colors as given in the legend. Figure from [127]. 74

6.3 Graphical representation of the energy spectrum for the 50-day period. The data are shown in the black line. The background coming from the double beta decay of the ^{136}Xe isotope, in blue, the solar neutrinos, in orange, the betas from the ^{222}Rn, the ^{220}Rn, and the ^{85}Kr isotopes, in green, and finally, the total background, in red, are also shown. The systematic uncertainty in the background is shown by the red band around the mean, and the statistic uncertainty by the green band. The magenta line is a gaussian fit to the excess of events in the signal region, representing the observed ^{124}Xe signal. 76

6.4 Graphical representation of the energy spectrum for the 50-day period. The data are shown in the black line. The background coming from the double beta decay of the ^{136}Xe isotope, in blue, the solar neutrinos, in orange, the betas from the ^{222}Rn, the ^{220}Rn, and the ^{85}Kr isotopes, in green, and finally, the total background scaled with a factor of 0.8, in red, are also shown. The magenta line is a gaussian fit to the excess of events in the signal region, representing the observed ^{124}Xe signal. 77

List of Tables

2.1 Most recent values of neutrino mixing parameters. The emphasis goes to the Δm^2_{Atm} value, it is positive in the normal hierarchy and negative in the inverted hierarchy. Data from [55]. 14

3.1 Different calibrations sources used in LZ, alongside its deployment strategy, type of emitted particles and half-life decay time. Table adapted from [90]. 34

4.1 Different background used for the ^{222}Rn isotope in order to obtain the required exposure time to claim different potentials as a function of its background. 57

4.2 Different contamination levels used for the ^{85}Kr isotope in order to obtain the required exposure time to claim different potentials as a function of its background. 58

Acronyms

ER electron recoil

LUX Large Underground Xenon

LXe liquid Xenon

LZ LUX-ZEPLIN

NR nuclear recoil

PMNS Pontecorvo–Maki–Nakagawa–Sakata

PMTs PhotoMultiplier Tubes

PTFE Polytetrafluoroethylene

SM Standard Model

SNO Sudbury Neutrino Observatory

SR1 Science Run 1

SURF Sanford Underground Research Facility

TPC Time Projection Chamber

WIMPs Weakly Interacting Massive Particles

ZEPLIN ZonEd Proportional scintillation in LIquid Noble gases

Chapter 1

Introduction

Neutrinos are one of the most mysterious particles in the Universe, and we do not have as much information about this kind of particle as we would like after nearly 70 years of its discovery. The SM is the most successful model to describe the fundamental particles and their behaviour. It assumed the form we do know now in the mid-1970s, nevertheless, a lot of theories had tested this model and try to change it and failed. However, neutrinos caused the first big blow to this model. Since only left-handed neutrinos are seen in nature, due to the Higgs mechanism, neutrinos in the SM are supposed to be massless. Yet, it was experimentally proven that there is neutrino flavors oscillation, therefore neutrinos must have a mass different from zero.

The nature of neutrinos would, indeed, open possibilities to solve this problem. If neutrinos are Majorana particles, they are their own antiparticle, and a Majorana mass term could resolve this issue. However, if they are Majorana particles, this would also mean that we could observe decay processes where neutrinos are not emitted, thus violating the conservation of the lepton number, namely, the Neutrinoless Double Beta Decay.

The observation of Neutrinoless Double Beta Decay could help solve some of the biggest questions in cosmology and physical particles, like the matter-antimatter asymmetry problem, and the neutrino mass hierarchy problem. However, these processes have a long half-life decay time, therefore, they are very difficult to observe. A first step in this search is to study the processes with the emission of neutrinos, which would allow us to improve the theoretical models for the neutrinoless case.

In this thesis, a search for the KK mode of the double electron capture of the ^{124}Xe isotope was performed using data from the first SR1 of the LZ experiment. This is the longest decay ever observed directly. To achieve this, it is required that we study the necessary time for the xenon circulation system to remove the ^{125}I isotope created during neutron calibrations of the detector, which, if not removed, would represent a significant background to our search. Therefore, after that study, we will be able to select a period with a much lower background. Several sensitivity studies were made in this work, which allowed us to know the required time necessary to reach the half-life measured by the XENON1T experiment.

The underlying physics of the search conducted during this work, namely the SM, neutrino physics, and Double Beta Decays[1] with and without emission of neutrinos, is

[1]It will be used capital letters in this class of processes, in order to distinguish it from the individual decay processes with the same name.

presented in Chapter 2. The LZ detector, its constituents, and the working principle of this kind of detector are covered in Chapter 3. Since backgrounds are essential in these searches, in Chapter 4, we explore the more important backgrounds to our search, and in the final part of this chapter several sensitivity studies were performed using the Rolke method. Since the ^{125}I isotope created during neutron calibrations would represent such a dangerous background if not well removed, Chapter 5 is entirely dedicated to studying the removal time of this isotope from the TPC. We start by seeing the observed signal due to the decay of the ^{125}I isotope, followed by the necessary steps to make this study, namely, the event and population selections. After that, the removal time was studied, allowing us to choose a search period for the double electron capture of the ^{124}Xe isotope. In Chapter 6, the search for the KK mode of the double electron capture of the ^{124}Xe isotope is done. Chapter 7 is reserved for some final conclusion drawn from the work done.

Chapter 2

Standard Model, Neutrino Physics and Double Beta Decays

In this chapter we will be giving an overview of the physics of relevance to this work, mainly we will be discussing the SM of particle physics, followed by neutrino physics, and finally, the different double beta decay processes both with the emission of neutrinos or without it. This last process is called Neutrinoless Double Beta Decay, and it is very important as we shall see. During this chapter, we will also understand the reasons behind the study of Double Beta Decay processes, as we will do in this thesis.

2.1 The Standard Model

The Standard Model of particle physics is the accepted model nowadays to describe the fundamental particles and their behaviour[1] [1]. It summarizes this long journey of physicists, from the discovery of the electron, in 1897, by J.J. Thomson [2] to the final piece of this model (maybe not), the long-awaited observation of the Higgs boson at the Large Hadron Collider in 2012 [3]. The fundamental particles of the standard model are represented in Figure 2.1. As we can see, they are divided into two subgroups depending on their spin. Particles with a half-integer spin are fermions obeying the Fermi-Dirac statistics, while particles with an integer spin are bosons following the Bose-Einstein statistics [4]. The latter particles can still be subdivided into vector bosons if they have a spin equal to one, and scalar bosons if they have zero spins.

In order to understand what is everything made of and how does it hold together we need to dive deeper in the SM. If we start by the "What is everything made of" part of this problem, then the fermions are what we need to study in more detail. There are 12 fermions: 6 quarks and 6 leptons. All the matter that we know is made of these particles. For instance, the protons and neutrons are formed by a combination of up and down quarks [6], and if we join an electron to them, the oldest known lepton, then we have an atom, as illustrated in Figure 2.2. Within the lepton subgroup, we have some of the most mysterious particles, the neutrinos, which raised one of the biggest late discoveries in the SM: The Neutrino Oscillations[2] [7]. Furthermore, there are two other particles similar to the electron but with a far greater mass, the muon and the tau.

[1] This model has also its shortcomings, that will be discussed later

[2] We will discuss a little bit more about what was the problem caused by this oscillation in the SM when we address the neutrino physics

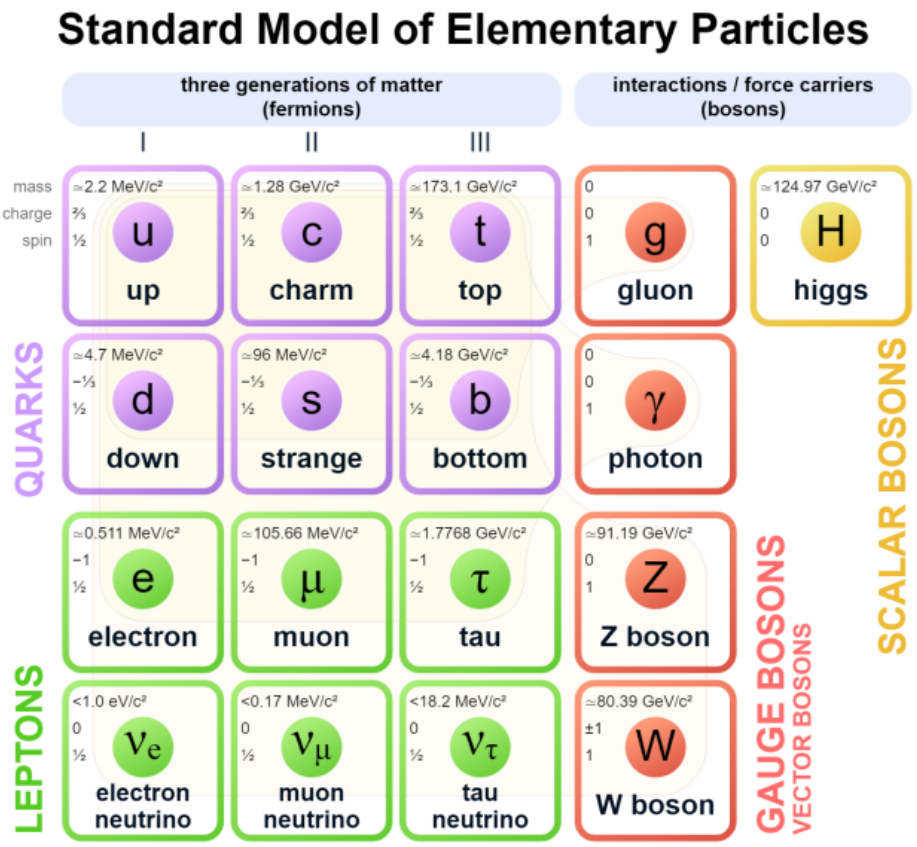

Figure 2.1: Pictorial representation of the Standard Model of Elementary Particles. On the left, are presented the three generations of matter, the fermions, while the force carriers, bosons, are represented on the right. The constituents of matter are further subdivided in two groups: quarks, in purple, and leptons, in green. The force carriers are subdivided considering their spin value. Particles with spin equal to one are vector bosons, represented in red, whereas the ones with spin equal to zero are scalar bosons. In this last category we have the particle that provides mass to the remaining particles, the Higgs boson. Figure from [5].

Regarding the second part of the question above, the 5 bosons present in the SM are responsible for all the interactions of matter that the SM can explain, that is, they are the carriers of 3 of the 4 fundamental forces, namely the strong force, the weak force and electromagnetism[3] [9]. Again, returning to the example of the nuclear atom: the strong force, mediated by the gluons [10], is responsible for holding quarks together to form larger particles as protons and neutrons. The Z and W bosons are known for mediating the weak force [10], due to which the beta decay occurs. One of the best known cases of this is the beta minus decay, where one neutron decays to one proton with the emission of an electron and an antineutrino [11]. Probably the most recognized boson by the majority of people is the photon, responsible for the electromagnetic force [10], which is present in our everyday life in the form of electric and magnetic fields. Looking at the SM, one boson remains to be discussed, the most famous and last to be discovered, the

[3]One of the SM shortcomings is that it does not include gravity [8]

Higgs boson. Before this particle was known, the scientific community struggled with a fundamental question, why do some fundamental particles have mass but others do not? The answer to this question was the Higgs boson. A Higgs field, which is a set of virtual Higgs bosons, has to fill all the space [12]. The particles that interact with this boson have mass different from zero; the stronger the interaction, the more massive the particles are [13]. So the photons and the gluons, which are the known massless particles, ignore this Higgs field. Since only left-handed neutrinos have ever been observed, then their mass term in the Lagrangian would not be a gauge invariant [14], thus neutrinos must also be massless particles in the SM. The neutrinos' mass will be further discussed in Section 2.2. The process in which the W and Z bosons acquire mass is known as the Higgs mechanism.

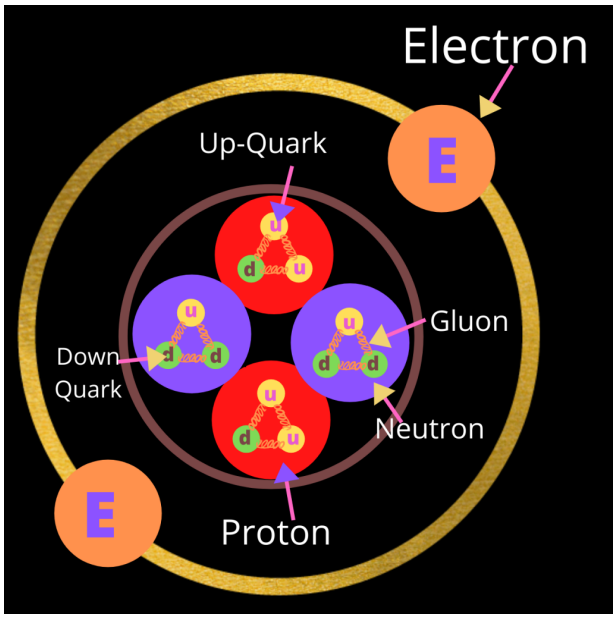

Figure 2.2: Quark model representation of an atom. Protons and neutrons, constituents of the nucleus, are made of up quarks (smallest yellow circles) and down quarks (green circles). Protons have two up quarks and one down quark, while neutrons have two down quarks and one up quark. These quarks are held together by the strong force, which is mediated by the gluon. Around these particles we have another elementary particle, the electron (big orange circles). Figure from [15].

Up to this point in this discussion it seems that this model is almost perfect in describing the fundamental particles and their behaviour, which is far from the truth. Nevertheless, it stood almost every test and it is nearly the same for a long time, despite the many attempts to break it. However, the SM also has some shortcomings, as we mentioned earlier. One of these problems can be clearly seen from what was said previously: gravity is missing in this model [8]. Although gravity is the ruling force in our macro-scale life, its power is almost nonexistent on the subatomic scale. However, we can not disregard this force because if we are talking about massive bodies such as black holes, then gravity becomes very important. This problem arises from the incompatibility between general relativity, the theory which describes gravity, and quantum mechanics, the theory that describes the subatomic world [16]. In general relativity, gravity is characterized as a property of spacetime [17], which is inconsistent with the

other forces.

The SM is a very good model to describe the tangible Universe, and by this we mean the normal matter that consists approximately 5% of the matter-energy of the Universe [18], but what about the remaining 95%? This problem is also one of the biggest problems with the SM, because there are no viable candidates within this model to explain dark matter and dark energy [19]. There are several other problems, but we want to mention a final big problem with this theory[4]. According to the SM, after the Big Bang, equal amounts of matter and antimatter should have been created [21], and then annihilated leaving only leftover energy and no matter. The Universe that we know of is solely constituted by matter, therefore something else must have happened during the Big Bang in order to some of that matter created during that moment still exists now.

2.2 Neutrino Physics

Neutrinos are leptons with $\frac{1}{2}$ spin that only interact through weak interactions or gravity [22]. The first has a very short range [23], and the latter is extremely weak [24], so these particles interact very weakly with matter. As such, after so many years of their discovery, we do not have as much information about these particles as we would like. Due to their extraordinary properties, like their mass and parity, they are one of the most exciting particles in the Universe. Lets rewind a bit in history and see the search on one of the most mysterious particles.

In the beginning of the twentieth century, the beta minus decay, β^-, was thought to be expressed through the following expression [25],

$$ {}^{\mathrm{A}}_{\mathrm{Z}}\mathrm{X} \rightarrow {}^{\mathrm{A}}_{\mathrm{Z+1}}\mathrm{Y} + e^-, \tag{2.1} $$

and if we think in energy conservation rules, then the electron should be emitted with an energy equal to the difference between the energies of the mother and daughter nuclei [26]. When the electron energy spectrum was measured, it was found to be continuous rather than a monoenergetic peak, as shown in Figure 2.3. Wolfgang Pauli, in 1930, addressed this problem by postulating a new particle, which he named neutron[5] [27]. This particle would have a very specific set of properties in order to resolve this issue [27]:

- Zero electric charge;
- Zero mass (or at least a mass close to zero);
- Being able to pass through matter without interacting, and thus being impossible to detect[6].

[4] Actually this is not a big problem, it is a giant one, because if this was true life was not supposed to exist, nor the Universe as we know it [20]

[5] In 1932, when James Chadwick discovered the chargeless counterpart of the proton, the neutron of today, the Italian physicist Enrico Fermi renamed this particle for the name we know it by today, the neutrino

[6] Very naively Pauli thought that this particle would penetrate a lead material with 10 centimeters of thickness very easily. Nowadays, it is estimated that it is necessary a lead material with a thickness of many light-years in order to stop this particle

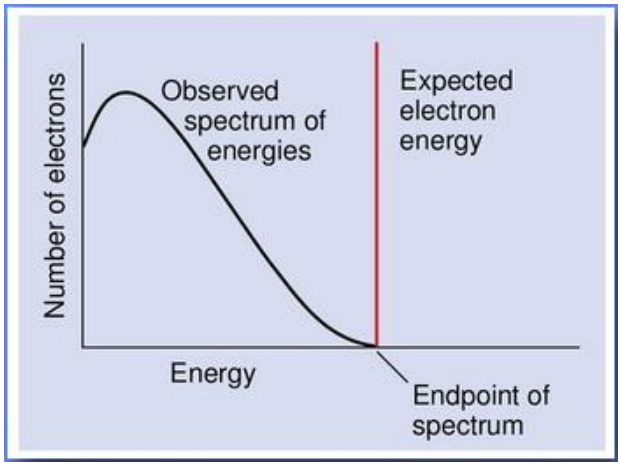

Figure 2.3: Comparison between the observed beta decay spectrum, in black, and the expected spectrum if that decay occurred without the emission of an neutrino (or antineutrino in the case of the beta minus decay), in red. Figure from [26].

The idea for the neutrinos was not solely due to this energy conservation problem but also because of the Spin-Statistic problem [27]. The Spin-Statistic theorem [28] states that a semi-integer spin particle obeys the Fermi-Dirac statistics, whereas an integer spin particle obeys the Bose-Einstein statistics. However, at the time, some nuclei did not behave as predicted. The more known one was the ^{14}N, which was thought to have 14 protons and 7 electrons [27], and each had a $\frac{1}{2}$ spin. Thus, this particle should have followed the Fermi-Dirac statistics, but despite this prediction, the ^{14}N obeys the Bose-Einstein. So then, Pauli postulated that the electrons and protons could not be the only constituents of the nucleus, and another fermion particle should also reside within the nucleus so that the full particle has a integer spin. Pauli thought nobody would ever detect this particle due to the characteristics that it must have. However, in 1956, Frederick Reines and Clyde Cowan proved him wrong and finally observed neutrinos experimentally using nuclear reactor neutrinos [29].

After this discussion, we need to take a step back and ask ourselves: Where do neutrinos come from? Are they created on Earth? Or are they coming from other places of the Universe? For the last two questions the answer is yes, the neutrinos can be subdivided into two groups:

- Terrestrial neutrinos: if they are produced on Earth either in an artificial way, such as reactors neutrinos, accelerator neutrinos, or neutrinos produced by nuclear weapons[7], or in a natural way alongside the natural radiation due to the decay of radioactive isotopes present in nature. The latter are called geoneutrinos;

- Extraterrestrial neutrinos: they are produced out of the Earth as we can understand by the name. There are many sources generating neutrinos outside of the Earth that eventually arrive to us. Examples of these are atmospheric neutrinos, solar neutrinos, neutrinos created in the Big Bang and in a Supernovae.

After reading this chapter, a reader with no previous knowledge of neutrino physics would have almost the same insight into this subject as a physicist in the 1960s. Then, it

[7]Before deciding for the nuclear reactors, Fred Reines and Clyde Cowan first considered studying neutrinos originated in a nuclear bomb [30].

is important to do a path coming from that time until now. At that time, they already knew what neutrinos were, and from where they came, so the next step was measuring the solar neutrino flux, which was achieved for the first time in the Homestake experiment[8] headed by Raymond Davis and John Bahcall [32]. Their experiment consisted of a tank filled with 380 m^3 of perchloroethylene, a compost rich in chlorine, installed 1478 meters deep underground in the Homestake gold mine, in South Dakota [33]. Through Equation 2.2 [9] [33] , we can understand the physics behind this experiment. Essentially, there was an electron neutrino originated in the sun that would react with an atom of chlorine, thus creating an electron and an argon atom. The latter would be later collected and counted, hence obtaining the neutrino flux,

$$\nu_e + {}^{37}\mathrm{Cl} \rightarrow {}^{37}\mathrm{Ar}^{+} + e^{-}. \tag{2.2}$$

I said before that two scientists led this experiment; John Bahcall was responsible for the theoretical calculation of the solar neutrino flux [33]. Using the Solar Model, he obtained the value of 7.6 SNU for the flux [33], where SNU is a unit used for Solar Neutrino Flux equal to the neutrino flux producing 10^{-36} captures per target atom per second. Raymond Davis designed the experiment and obtained 2.56 SNU [33] through the process described above. Therefore, the experiment obtained only about $\frac{1}{3}$ of the theoretical prediction, originating what became known as the Solar neutrino problem [34]. The physicists at the time did not understand the apparent disappearance of the neutrinos that were supposed to arrive to Earth. This problem took a long time to be solved and was only resolved in 2002 [35], more than 30 years after the Homestake experiment.

After this experiment, two others were crucial for our understanding of neutrinos and, more specifically, for the thematic of neutrino oscillations[10]: the SNO [36] and Super-Kamiokande [37] experiments. The former was the first to resolve this Solar neutrino problem [35], and the latter was the first one to prove neutrino oscillations [38].

In the Super-Kamiokande, this detection was carried out using electron elastic scattering events in a water medium [39],

$$\nu_x + e^{-} \rightarrow \nu_x + e^{-}. \tag{2.3}$$

If we look carefully at this process' equation, it shows that this experiment is sensitive to all three neutrino flavors. Unfortunately, this problem is not completely solved because due to the charged current process [40] contribution to the electron elastic scattering, there is an interaction probability of 6.5 to 1 in favor of electron neutrinos regarding the other ones [36]. Then, it would be difficult to obtain conclusive results from this. That proved to be the case when they obtained their results and got only 45% of the theoretically predicted flux [39], which assumed that they all were still electron neutrinos. So, if they had oscillated to other flavors, the flux would be much higher due to the interaction probability problem. However, the Solar neutrino problem remained since there was no way to determine how much higher this flux was. Although, that was not

[8]The LZ experiment is conducted in the Davis Cavern [31], which as can be inferred by the name is where the Homestake experiment was also performed.

[9]One thing that is obvious to us today, but at the time was not yet known is the fact that this experiment was only sensitive to one type of neutrinos.

[10]After this experimental discussion, the more theoretical aspect of neutrino oscillation will also be approached.

the case regarding the big picture of neutrino oscillation. Atmospheric neutrinos, which are originated from the collision of cosmic rays with particles in the upper atmosphere, proved to be crucial in this experiment. The interaction of the neutrinos in the water form Cherenkov rings, which enable us to calculate the direction of the incoming neutrino [39], and this number of detected neutrinos were supposed to be independent of this azimuthal angle[11] [39] since the flux of cosmic rays is almost isotropic [41]. Through this analysis, they proved that the number of neutrinos that traveled directly from the atmosphere to the detector (about 10 km) coincide with the expected number without oscillation [39]. Whereas the neutrinos that traveled a longer distance, from the other side of the Earth (about 10000 km), arrived in a much smaller number compared to the expected [39]. This means that the neutrinos traveling a longer distance were oscillating to other flavors, and the others would not because they did not travel enough distance to do so. Therefore, the neutrino oscillation was finally proven.

Despite this, the Solar neutrino problem was not yet solved. This was achieved by the SNO experiment. Instead of using water as Super-Kamiokande [39], they use heavy water, D_2O [36]. This compost is created by substituting the hydrogen atoms for deuterium. Due to this, two more processes become available beyond the one in Equation 2.3, and they are represented in Equations 2.4 (Neutral Current) [36] and 2.5 (Charged Current) [36],

$$\nu_x + d \rightarrow p + n + \nu_x, \tag{2.4}$$

$$\nu_e + d \rightarrow p + p + e^-. \tag{2.5}$$

In order to study the Solar neutrino problem it is necessary to measure the flux of each of the three processes mentioned. It is exactly that what we have in Figure 2.4, where this flux was measured for the ^{8}B chain [42]. It represents the flux of the neutrinos with μ or τ flavor as a function of the electron neutrino flux. Through that, values for the flux of each individual process were obtained in the moment where $\phi_{\mu\tau} = 0$. Then, we have the following values $\Phi_{CC} = 1.76^{+0.06}_{-0.05}(stat.)^{+0.09}_{-0.09}(syst.)$, $\Phi_{ES} = 2.39^{+0.24}_{-0.23}(stat.)^{+0.12}_{-0.12}(syst.)$, $\Phi_{NC} = 5.09^{+0.44}_{-0.43}(stat.)^{+0.46}_{-0.43}(syst.)$ [36]. These flux values were all presented in units of $10^6\, cm^{-2}\, s^{-1}$. Through the previous equations, we understand instantly that the Charged Current process measures the flux for the electron neutrinos. Then, if the total flux is obtained using the Neutral Current process, we can subtract the electron neutrino flux, thus obtaining the flux for the neutrinos with μ or τ flavor. Making use of that one can obtain the following values,

- $\Phi_{\nu_e} = 1.76^{+0.06}_{-0.05}(stat.)^{+0.09}_{-0.09}(syst.)$
- $\Phi_{\nu_{\mu\tau}} = 3.33^{+0.45}_{-0.45}(stat.)^{+0.48}_{-0.45}(syst.)$

From this we can withdraw a big conclusion, the total flux of ^{8}B solar neutrinos[12] has a huge contribution from neutrinos without electronic flavor. Therefore, we need to see if this was predicted theoretically. In order to achieve this, it is essential that we consider Equation 2.6 [42] that expresses this process,

[11] Where this is the angle between the incoming neutrino and the vertical.

[12] The neutrinos from ^{8}B are the more energetic, therefore they are the ones detected due to the energetic threshold of the detectors.

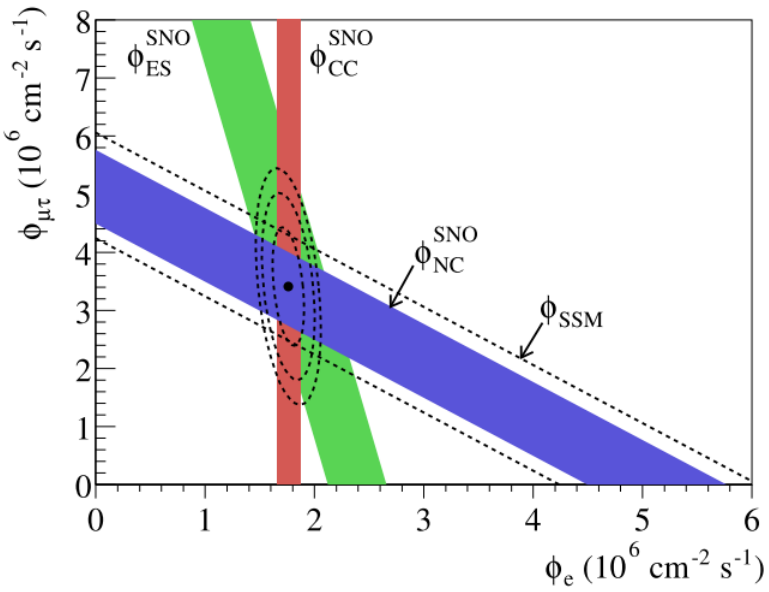

Figure 2.4: Solar neutrinos flux from ^{8}B. Through the three neutrino reactions in SNO, was obtained this flux for the neutrinos with muon and tau flavors, identified by $\phi_{\mu\tau}$, as a function of the neutrino flux with electron flavor, denoted by ϕ_e. The diagonal dashed lines show the total ^{8}B flux as predicted by the Standard solar model. Figure from [43].

$$^8\mathrm{B} \rightarrow {}^8\mathrm{Be}^* + e^+ + \nu_e. \tag{2.6}$$

Through this, it is possible to see that the ^{8}B chain only emits electron neutrinos, thus we expect $\Phi_{\nu_{\mu\tau}} = 0$. However, this does not correspond to the measured value. For that reason, the neutrinos originating in the Sun must oscillate in flavor in their journey to Earth. This was the missing proof in order to resolve the Solar neutrino problem.

After discussing the experimental part of this oscillation, it is now time to address the theoretical component, which will lead us to some conclusions I have somewhat spoiler before regarding the supposed massless neutrinos.

This idea of neutrino oscillations first came around in 1957, when Bruno Pontecorvo [44, 45], considering the oscillations in mesons [46], for instance, in the neutral Kaon mixing, proposed that neutrino-antineutrino transitions can be possible. Later, in 1962, from this idea, Maki, Nakagawa and Sakata developed the first quantitative theory of neutrino flavor oscillation [47]. Finally in 1967, Bruno Pontecorvo refined this theory and ended it [48].

In this theory, the flavor eigenstates, ν_a, propagate in space-time as linear combinations of mass eigenstates, ν_i [49]

$$|\nu_\alpha\rangle = \sum_{i=1}^{N=3} U^*_{\alpha i} \, |\nu_i\rangle \, , \tag{2.7}$$

where in this relationship we have $U_{\alpha i}$, which is the Pontecorvo–Maki–Nakagawa–Sakata (PMNS) matrix [49], and its form is shown below[13]:

[13]Here I will only present the matrix form assuming that the neutrinos are Dirac particles. If they are Majorana particles, then two extra complex phases are required.

$$U_{\alpha i} = \begin{pmatrix} c_{12}c_{13} & c_{13}s_{12} & s_{13}e^{-i\delta} \\ -c_{23}s_{12} - c_{12}s_{13}s_{23}e^{i\delta} & c_{12}c_{23} - s_{12}s_{13}s_{23}e^{i\delta} & c_{13}s_{23} \\ s_{23}s_{12} - c_{12}c_{23}s_{13}e^{i\delta} & -c_{12}s_{23} - c_{23}s_{12}s_{13}e^{i\delta} & c_{13}c_{23} \end{pmatrix}, \tag{2.8}$$

where $c_{ij} = \cos\theta_{ij}$, $s_{ij} = \sin\theta_{ij}$ and δ is a single phase related to charge-parity violations.

We will now restrict ourselves to the two-flavor case. We will do this because it is a much simpler case, but it still allows us to obtain the same conclusions of the full three-flavors for the active neutrinos[14].

In this particular example, if we consider, for instance, the electron and muon flavor, we have the following expressions [49],

$$|\nu_e\rangle = \cos\theta\,|\nu_1\rangle + \sin\theta\,|\nu_2\rangle\,, \tag{2.9}$$

$$|\nu_\mu\rangle = -\sin\theta\,|\nu_1\rangle + \cos\theta\,|\nu_2\rangle\,. \tag{2.10}$$

Due to these mass eigenstates also being eigenstates of the Hamiltonian that describes the propagation of neutrinos, then these initial states will evolve with an exponential time dependence [50]. Therefore, if we consider the first one[15], the time evolution of this will be given by,

$$|\psi(t)\rangle = cos\,\theta\,|\nu_1\rangle\,e^{-iE_1t} + sin\,\theta\,|\nu_2\rangle\,e^{-iE_2t} = (cos\,\theta\,|\nu_1\rangle + sin\,\theta\,|\nu_2\rangle\,e^{-i(E_2-E_1)t})e^{-iE_1t}. \tag{2.11}$$

Regarding the term outside of the parentheses in the second equality, it will be ignored from now on. The reason behind this is that we are not really interested in the wave function, but rather in probabilities that make use of this function. In that calculation, this term would be multiplied by its conjugate and, therefore it will be cancelled. The energy term of the i-th mass eigenstate, in natural units, is expressed as $E_i = \sqrt{p^2 + m_i^2}$. This expression can be expanded in Taylor series, thus obtaining,

$$E_i \cong p\left(1 + \frac{m_i^2}{2p^2}\right) \cong p. \tag{2.12}$$

The last approximation comes from the fact that neutrinos are ultra-relativistic particles, so the term with their mass is negligible due to their velocity. Using the results obtained in Equation 2.12, on the energy difference present in the exponential of Equation 2.11, we can derive,

$$E_2 - E_1 = \frac{m_2^2 - m_1^2}{2E} = \frac{\Delta m^2}{2E}. \tag{2.13}$$

Defining $\phi \equiv \frac{\Delta m^2 t}{2E}$ and substituting the previous expressions, we can now obtain a final expression for the temporal evolution of the wave function as a function of the mass eigenstates,

$$|\psi(t)\rangle = \cos\theta\,|\nu_1\rangle + \sin\theta\,|\nu_2\rangle\,e^{-i\phi}. \tag{2.14}$$

If we now want to obtain the last expression with a dependence in the flavor eigenstates, we need to invert the Equations 2.9 and 2.10. Doing this we obtain the expressions for the mass eigenstates, therefore if we substitute that in Equation 2.14 we obtain,

$$|\psi(t)\rangle = (\cos^2\theta + \sin^2\theta\,e^{-i\phi})\,|\nu_e\rangle + \cos\theta\sin\theta(e^{-i\phi} - 1)\,|\nu_\mu\rangle\,. \tag{2.15}$$

[14]I mentioned active neutrinos because sterile neutrinos are not yet a excluded hypothesis, so they would elevate this number, but we are not going to talk about them here.

[15]Where the initial state will be equal to $|\psi(0)\rangle = |\nu_e(0)\rangle$

In a two-flavor case, if, for example, a electron neutrino is created, there are two possible outcomes after a certain time t. On one hand, the neutrino can change its flavor and, in this specific example, become a muon neutrino. The probability of this happening is given by Equation 2.16,

$$P(e \to \mu) = |\langle \nu_\mu | \psi(t) \rangle|^2 = \sin^2(2\theta) \sin^2(\frac{\Delta m^2 t}{4E}). \tag{2.16}$$

On the other hand, the previously created neutrino can remain an electron neutrino. The sum of the probabilities of the possible cases, as we can understand, must equal to 1, so we have,

$$P(e \to e) = |\langle \nu_e | \psi(t) \rangle|^2 = 1 - \sin^2(2\theta) \sin^2(\frac{\Delta m^2 t}{4E}). \tag{2.17}$$

These oscillation probabilities depend on oscillatory functions. So, if there is some mixing, $\theta \neq 0$, and if $\Delta m^2 \neq 0$, where, at least, one pair of neutrinos have different masses[16], then neutrino oscillation can occur. We previously showed that neutrino oscillations were proven experimentally. So, in fact, it is also established that the mass of all flavors of neutrinos can not be zero. Then neutrinos must have mass[17] in contrast to the prediction of the SM [51]. Due to neutrino oscillations, the lepton flavor number is no longer conserved [52], as was thought prior to this discovery. Despite this, the total lepton number is still conserved[18].

Oscillation experiments do not measure the absolute mass of the neutrino mass states being only sensitive to the three mass squared differences, Δm^2_{ij} [54]. Even though we do not know the absolute value for m_1, m_2, m_3, the mass eigenstates of ν_1, ν_2, ν_3, respectively, we know that m_2 is greater than m_1 [53]. This is possible through experiments that study solar neutrinos, because they measured a positive value for this quantity, $\Delta m^2_{12} = \Delta m^2_{\text{Sol}} = +7.42^{+0.21}_{-0.20} \times 10^{-5}$ eV^2 [55]. The values measured by atmospheric neutrinos experiments are a little bit more tricky, because they measure this mass split throughout neutrino oscillations in vacuum [56]. This oscillation depends solely on its absolute value, so we can not know if the value obtained in this type of experiment is positive or negative. Then, despite knowing that m_2 is greater than m_1, we do not know if m_3 is larger or smaller than m_2. This is known as the neutrino mass hierarchy problem [57]. If m_3 is larger than m_2, then we are considering the normal hierarchy [57]. But if m_3 is lighter than m_2, we are in the inverted hierarchy scenario [57]. The two possible ordering hierarchies are represented in Figure 2.5.

Looking at Table 2.1, we can reflect about the most recent values of the quantities previously mentioned concerning neutrinos. We can see that the mass difference obtained from solar neutrino experiments has the same signal and absolute value both in the normal or inverted hierarchies, as we said before. In contrast, the mass difference in the atmospheric neutrinos is positive in the normal hierarchy, and negative in the inverted hierarchy, as was expected, because ν_3 is heavier than ν_2 in the first case and lighter in the second one.

[16] Obviously that in this case there are only two types, but this also applies to other cases with higher number of neutrino flavors.

[17] The only requirement is that the mass difference is not zero, so there is the possibility that one type of neutrinos have mass equal to zero.

[18] Although this does not influence the total lepton number conservation, we will study a process, Neutrinoless Double Beta Decay, that if proven to exist, will violate this conservation.

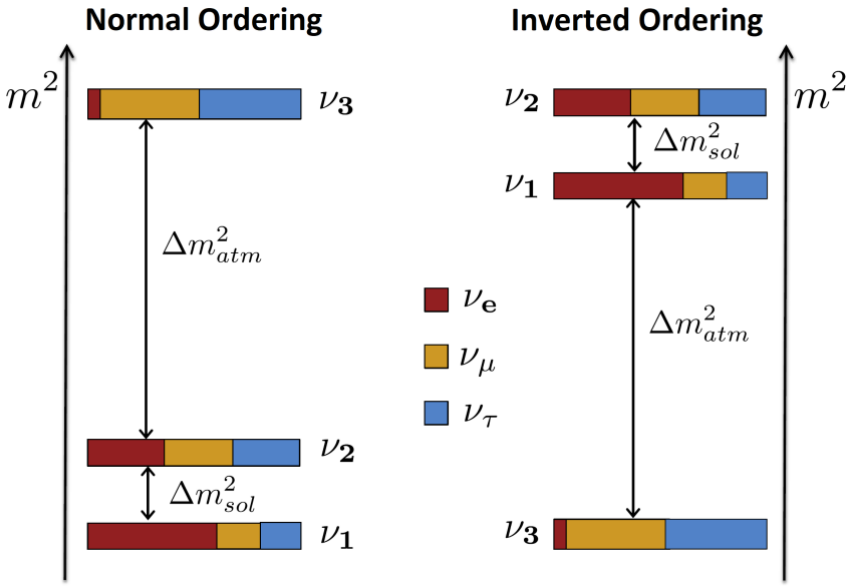

Figure 2.5: Distinct possibilities in the neutrino mass hierarchy problem: on the left, we have the normal ordering, where m_3 is greater than m_2, whereas on the right we have the inverted ordering with m_3 lighter than m_2 (the mass is growing upward). Each mass eigenstate is a mixing of different neutrino flavors, where the electron, muon and tau flavors are represented by the red, orange and blue colors, respectively. Figure from [53].

2.3 Double Beta Decay

Nowadays, physicists do not know if neutrinos are Dirac or Majorana particles[19]. Rewinding to a long time ago, neutrinos were thought to be Dirac particles, and by this we mean that they are not their own antiparticle and obey the Dirac equation. However, Ettore Majorana proved that the beta decay theory remained consistent if the neutrino were its own antiparticle [58]. If that is the case, we call it a Majorana particle, and it would allow the existence of neutrinoless processes, namely Neutrinoless Double Beta Decay. Although this was theorized, this type of process was never observed because, if they indeed exist, they are expected to have extremely long half-life decay time[20] [59]. So then, in this section, we will address the Double Beta Decay with the emission of two neutrinos, whereas the Neutrinoless Double Beta Decay will be our thematic for the next one.

Before starting to approach these processes, it is important to discuss the first-order process related to them, the Beta Decay. This is a broad term that actually encompasses three different processes, they have several features that are transversal to them. All of them occur in unstable nuclei in order to have a more stable ratio of protons to neutrons if the reaction is energetically possible. This last statement means that the Q-value of a reaction [60], this is basically the energy absorbed or released during the nuclear reaction, must be positive. Starting now from the processes with the same name of the

[19]Since neutrinos are chargeless particles, it is possible that they are their own antiparticle.

[20]It is expected that they have a half-life decay time of several orders of magnitude higher than the processes with emission of neutrinos.

Table 2.1: Most recent values of neutrino mixing parameters. The emphasis goes to the Δm^2_{Atm} value, it is positive in the normal hierarchy and negative in the inverted hierarchy. Data from [55].

Parameter	Normal hierarchy	Inverted hierarchy
	best fit $\pm 1\sigma$	best fit $\pm 1\sigma$
$\theta_{12}(^\circ)$	$33.45^{+0.77}_{-0.75}$	$33.45^{+0.78}_{-0.75}$
$\theta_{13}(^\circ)$	$8.62^{+0.12}_{-0.12}$	$8.61^{+0.14}_{-0.12}$
$\theta_{23}(^\circ)$	$42.1^{+1.1}_{-0.9}$	$49.0^{+0.9}_{-1.3}$
$\delta_{CP}(^\circ)$	230^{+36}_{-25}	278^{+22}_{-30}
$\Delta m^2_{\text{Sol}}(10^{-5}\ \text{eV}^2)$	$7.42^{+0.21}_{-0.20}$	$7.42^{+0.21}_{-0.20}$
$\Delta m^2_{\text{Atm}}(10^{-3}\ \text{eV}^2)$	$+2.510^{+0.027}_{-0.027}$	$-2.490^{+0.026}_{-0.028}$

general process, we have the beta minus decay[21], β^-, in which the atomic number of the nucleus is increased by one with the consequent emission of an electron and an electron antineutrino [61]. In other words, a neutron originates a proton, an electron and an electron antineutrino,

$$n \to p + e^- + \overline{\nu}_e. \tag{2.18}$$

The last process with the same name is the beta plus decay, β^+, in which a neutron is originated from a proton with the emission of a positron and an electron neutrino [61],

$$p \to n + e^+ + \nu_e. \tag{2.19}$$

Another process associated with positron emission is the electron capture. Electron

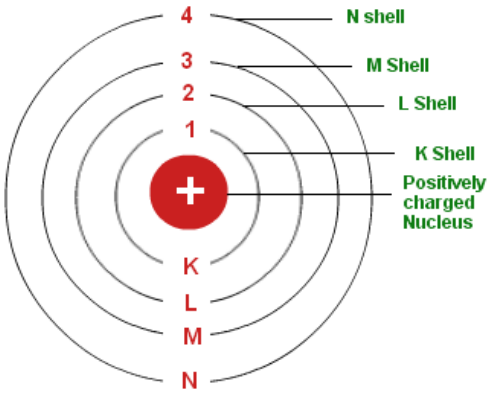

Figure 2.6: An electron shell diagram: through this, it is possible to understand the reason for the higher likelihood of the electron absorbed during electron capture coming from the shells closest to the nucleus. Figure from [62].

capture consists of the absorption of an electron, usually from the K shell, by the nucleus,

[21] This was the process previously described in the discussion of neutrino postulation.

thus changing a nuclear proton to a neutron with consequent emission of an electron neutrino [63],

$$p + e^- \rightarrow n + \nu_e. \tag{2.20}$$

In Figure 2.6 it is possible to see the different electron shells, where the K shell is the closest one to the nucleus. After the electron capture, a hole is created in an atomic shell due to the absorbed electron. Because it is in a more favorable energetic position, this vacancy will be filled by an outer electron, with emission of X-rays and/or Auger electrons [63].

It was said before that a reaction's Q-value must be positive for a beta decay to occur. This value is given by [64],

$$Q = (m_r - m_p) \times 0.9315\,\mathrm{GeV}, \tag{2.21}$$

where m_r are the sum of the mass of the reactants, including the mother nucleus, and m_p are the sum of the product masses, including the daughter nucleus. In this equation, the masses are expressed in unified atomic mass units[22]. Therefore, the requirement of Q positive can be translated to a condition of the masses. Thus, beta decay is possible if the mass of the daughter nucleus is lower than that of its mother nucleus.

Sometimes, the nucleus that would be a candidate for the beta decay of some atom has a lower mass than the daughter nucleus. Due to this, the mother atom would be thought as being stable. However, if the atom with atomic number different by two units from the mother nucleus has a smaller mass than that nucleus, a new process is possible: Double Beta Decay.

Double Beta Decay is a second-order process that results in a decay to an isobar atom, but with an atomic number higher or lower (depending on the process) by two units. It is possible in atoms where the first-order beta decay is forbidden so that atoms were previously considered stable, as was the case for ^{124}Xe [65].

In Figure 2.7, we have the two mass parabolas for isobaric nuclei, with an even mass number, A, for odd-odd (O-O) and even-even (E-E) nuclei. Where odd or even identifies the nature of the number of protons and neutrons. An odd-odd nucleus is constituted by an odd number of neutrons and an odd number of protons. In the even-even case, we have an even number of neutrons and an even number of protons.

In these two specific cases, an additional term will be added to their binding energies not present in the cases with odd-even mixtures [67]. This term is called nuclear pairing energy. Although it has the same magnitude for these two cases, it is positive for the even-even case and negative for the odd-odd case. Due to this, we have a splitting of the mass parabola, as is demonstrated in Figure 2.7, where the odd-odd will have a mass parabola higher than the even-even because the binding energy in the semi-empirical mass formula has a minus signal, as we can see in Equation 2.22 [67],

$$m = Zm_p + Nm_n - \frac{E_B}{c^2}. \tag{2.22}$$

In Figure 2.7, it is presented possible decays. From left to right, the atomic number is increasing, so we have beta minus decay, β^-, whereas coming from right to left we have the atomic number decreasing, then we have beta plus decay, β^+. Another possibility for

[22] 1u (symbol that represents the unified atomic mass units) is equivalent to 931.5 MeV/c^2, so it is necessary that we multiply the masses by 0.9315 GeV in order to have units of energy for the Q-value.

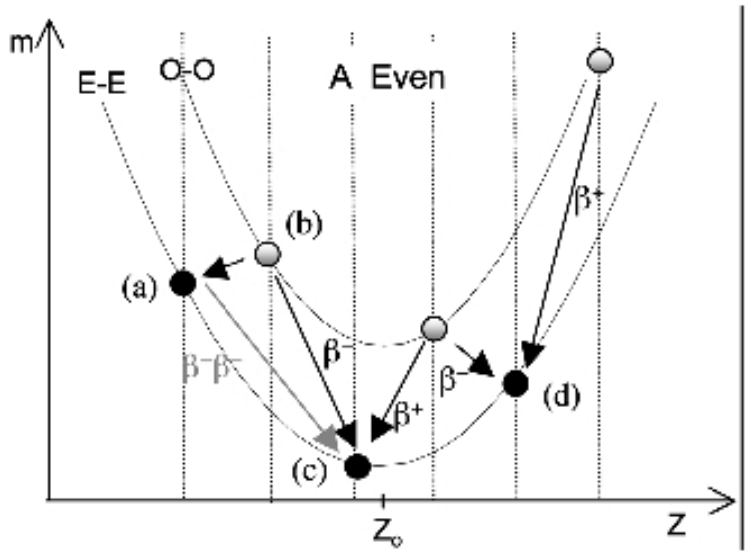

Figure 2.7: Representation of the mass obtained using the semi-empirical mass formula as a function of the proton number, Z. The two lines identify the two mass parabolas for isobaric nuclei, with an even mass number, A, for odd-odd (O-O) and even-even (E-E) nuclei. An odd-odd nucleus is constituted by an odd number of neutrons and an odd number of protons. In the even-even case, we have an even number of neutrons and an even number of protons. Due to the neighbour nuclei masses, Double Beta Decay can occur from (a) to (c) and from (d) to (c). However the atom in (a) can not decay to the atom in (b), by beta minus decay, since it is not energetically accessible. Figure from [66].

this last case would be electron capture because, as we saw in Equation 2.20, it has the same impact in the atomic number as the beta plus decay.

Due to their masses, the atom in (a) can not decay to (b) because its mass is lower, so it decays to the second neighbour, in (c), via double beta decay. The same is happening in (d), because it is impossible to him to decay via, β^+, so it will decay to (c) by double beta decay. All of these atoms are decaying to (c) because it is the stable nucleus, due to being the atom with the lowest mass in this parabola. Then, in summary, if m(Z, A) $<$ m(Z+1, A) beta minus decay is forbidden, and it is required that m(Z, A) $<$ m(Z+2, A), in order to double beta decay minus occur.

The Q-value of a reaction dictates which modes are possible. If that value is higher than 1.022 MeV, the equivalent of two electron masses, then double beta decay minus (or plus) is possible. If that value is higher than 511 keV, electron capture with coincident positron emission is a possibility, whereas the double electron capture is accessible if the Q-value is positive [68]. It is time to address all the possibilities of Double Beta Decay in more detail.

2.3.1 $2\nu\beta^-\beta^-$ decay

Double beta decay minus is a nuclear transition[23] where, as we can see by Equation 2.23 [66], a nucleus with mass number A and atomic number Z decays to a nucleus with the same mass number A and atomic number Z+2. In this process, where in fact, two neutrons transform into two protons, two electrons and two electron antineutrinos are also emitted,

$$(A,\ Z) \rightarrow (A,\ Z+2) + 2\,e^- + 2\,\overline{\nu}_e. \tag{2.23}$$

As can be seen, in Figure 2.7, a natural candidate for this process is an even-even nucleus (A, Z) more bounded than its (A, Z+1) neighbour, but with a second neighbour (A, Z+2) even more bounded than itself [66].

2.3.2 $2\nu\beta^+\beta^+$ decay

In the double beta decay plus, two neutrons are originated from two protons, with consequent emission of two positrons and two electron neutrinos. In this process, a nucleus with a mass number A and an atomic number Z, (A, Z) decays to a nucleus with an atomic number Z-2, (A, Z-2), emitting two positrons and two electron neutrinos [69]

$$(A, Z) \rightarrow (A,\ Z-2) + 2\,e^+ + 2\,\nu_e. \tag{2.24}$$

Like the previous process, this decay also happens to an even-even nucleus (A, Z) [66]. In order for this specific decay occur it is required that its first neighbour (A, Z-1) is less bounded, and its second neighbour (A, Z-2) is more bounded, and therefore more bounded than the first neighbour [66].

2.3.3 $2\nu ECEC$ decay

Double electron capture is the second-order process of the electron capture. A nucleus (A, Z) absorbs two atomic electrons, thus originating two neutrons from its protons, becoming the nucleus (A, Z-2) [68]. There is a possibility that this daughter nucleus is in a excited state, and it will de-excite through photon emissions with energies of hundreds of keV, more know as gammas [63],

$$(A,\ Z) + 2\,e^- \rightarrow (A,\ Z-2) + 2\,\nu_e. \tag{2.25}$$

As was seen in the first-order process, due to the capture of the electrons, vacancies appear in the shells where this happened. The shells from where those electrons originated give the different modes' name. The most likely ones are the KK, KL and LL modes. Equally to the first-order decay, this hole will be filled by an outer electron, with consequent emission of X-rays and/or Auger electrons [63].

[23] All Double Beta decays occur between isobaric atoms, because the daughter and mother nuclei have the same mass number, A.

2.3.4 $2\nu EC\beta^+$decay

In this process, a nucleus (A, Z) captures an electron and a positron will be emitted alongside two electron neutrinos [68]. For that reason, the final nucleus (A, Z-2) will have two more neutrons and two fewer protons than the mother nucleus. Due to the vacancy created in the shell, as in the previous cases of electron capture, an outer electron will fill this energetically favorable hole, thus originating a cascade of X-rays and Auger electrons,

$$e^- + (A,\ Z) \rightarrow (A,\ Z-2) + e^+ + 2\,\nu_e. \tag{2.26}$$

This process is characterized by the two back-to-back gamma-rays each with 511 keV from the annihilation of the positron with an atomic electron.

2.4 Neutrinoless Double Beta Decay

The nature of neutrinos is of the utmost importance. As was previously discussed, if neutrinos are Dirac particles, then Double Beta Decay can only occur with neutrino emission. This is the process allowed by the SM, because there is conservation of the total leptonic number. If neutrinos are Majorana particles, another mode becomes possible, Neutrinoless Double Beta Decay [70]. In this new mode, neutrinos are their own antiparticles and for that reason no neutrinos are emitted, as illustrated by Figure 2.8 for the case of the decay with emission of two electrons. This process is not allowed by

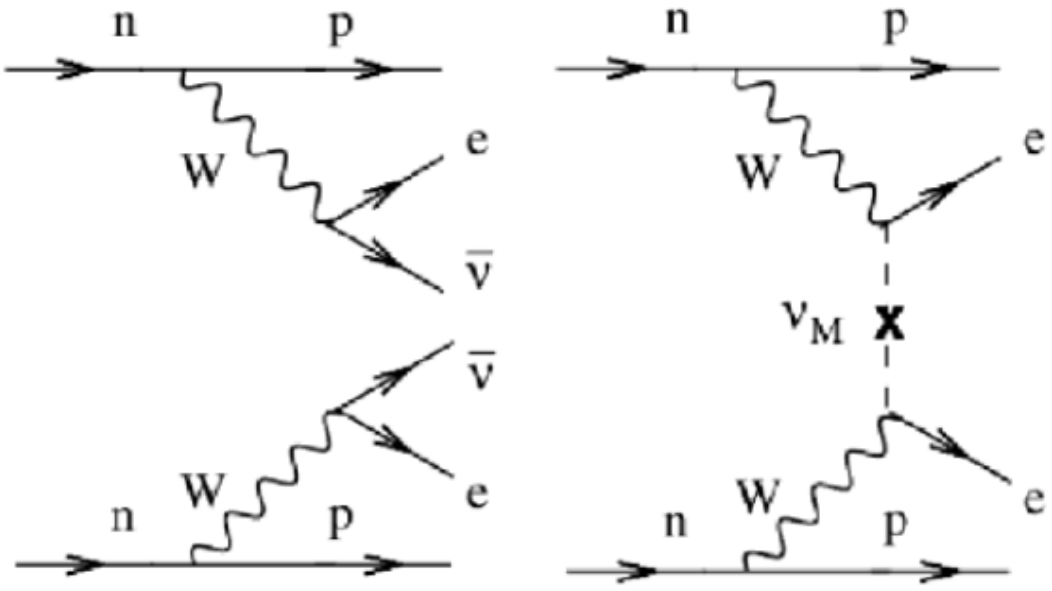

Figure 2.8: Feynman diagrams for the $2\nu\beta^-\beta^-$, on the left, and for the $0\nu\beta^-\beta^-$, on the right. In the latter, because in that case neutrinos are Majorana particles and so they are their own antiparticles, there are no emission of neutrinos. Figure from [71].

the SM since it violates the conservation of the total leptonic number by two units [70]. This prohibition does not come directly due to the violation of the conservation of the total leptonic number, which is not required in the SM, but rather due to the violation

of a fundamental symmetry of the SM, the B-L symmetry[24] [70]. It would be a severe setback to the current SM and a restructuring would be required.

We have discussed the matter-antimatter asymmetry problem before, but we can rewind a little bit and understand it better. The Big Bang should have created equal quantities of matter and antimatter. But, it is very strange that all that we see in the Universe, including life on Earth, is made only of matter, which implies this symmetry is broken for some processes, producing more matter than antimatter. Only a small portion of matter did not interact with antimatter and got destroyed in the early Universe. Leptogenesis is a class of scenarios where this asymmetry is generated from a lepton asymmetry. Leptogenesis, if true, would help to explain this asymmetry [72]. So, decays of heavy Majorana neutrinos would generate preferably matter over antimatter thus creating a lepton asymmetry, which is one the cornerstones of the neutrinoless processes. In turn, some of this asymmetry would be converted in baryon asymmetry through sphaleron processes [73, 74]. Thus, if proven to be accurate, Majorana neutrinos can explain one of the most pursued problems in Physics.

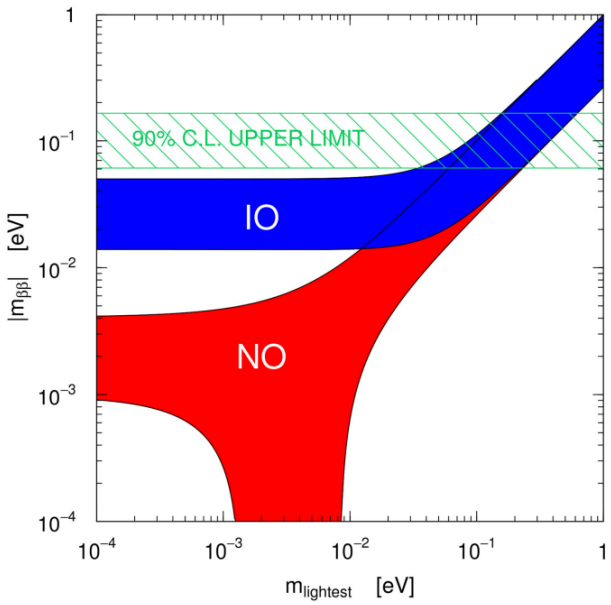

Figure 2.9: Effective Majorana mass as a function of the lightest neutrino mass at 99.7% CL, comparing inverted ordering, in blue, and normal ordering, in red, of the three active neutrinos. The green band represents the 90% CL bounds from KamLAND-Zen. Figure from [75].

Besides that, these neutrinoless channels are also very sensitive to the absolute mass scale, and consequently to the mass hierarchy of the neutrino [76]. In Figure 2.9, it is shown the dependence of the effective Majorana mass with the lightest neutrino mass for the two different orderings. The different energies intervals are depicted in that figure for the normal and inverted orderings. If that values are sufficiently constrained due to observations, namely neutrinoless processes, then we could arrive at a point of exclusion for one of the possibilities. Therefore, this kind of study and through theoretical nuclear-

[24]In every decay, the difference between the baryonic number and the leptonic number (B-L) must be constant before and after this process.

matrix-element calculations it could finally resolve this longstanding problem in neutrino physics.

In Figure 2.10, we can see the energy spectrum for the two different modes. In a $2\nu\beta^-\beta^-$ decay, the neutrinos will carry some of the energy away, so the electron will have a continuum energy spectrum which will terminate in the Q-value. In contrast, we have the $0\nu\beta^-\beta^-$ decay, where there are no neutrinos, so electrons will be emitted with energy equal to the Q-value and a monoenergetic energy spectrum peak.

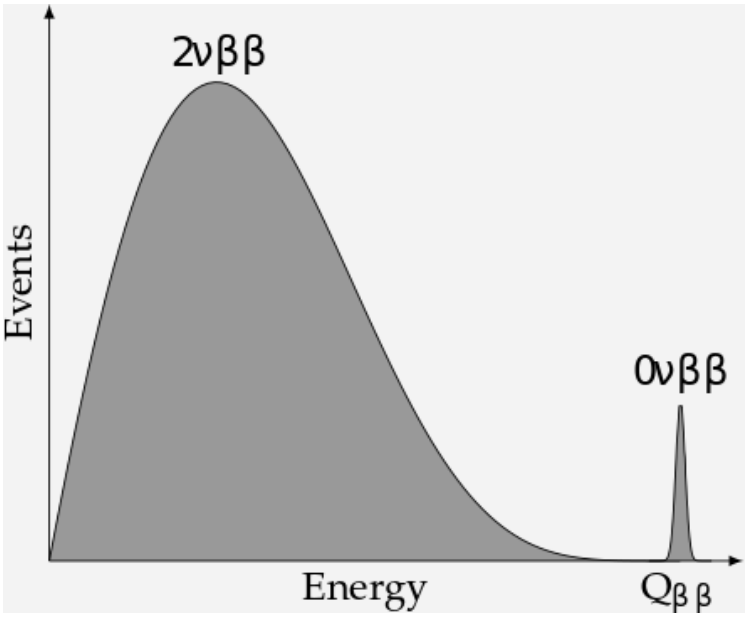

Figure 2.10: The energy spectrum for the $2\nu\beta^-\beta^-$ and the $0\nu\beta^-\beta^-$ decays: an event excess in the end of the spectrum represents the signature of the $0\nu\beta^-\beta^-$ decay with the two emitted electrons carrying the entire Q-value energy. Figure from [77].

It is now time for us to discuss each process individually, as we did for the cases with the emission of neutrinos.

2.4.1 $0\nu\beta^-\beta^-$ decay

In the neutrinoless double beta decay minus, $0\nu\beta^-\beta^-$, as in the equivalent process with neutrinos emission, the atom's atomic number will increase by two units, due to the transformation of two neutrons in protons. In this process, two electrons will also be emitted but the big difference is that in this case no neutrinos are emitted, as we can see by Equation 2.27 [68],

$$(A,\ Z) \rightarrow (A,\ Z+2) + 2\,e^-. \tag{2.27}$$

This lack of neutrino emission can also be understood in the Feynman diagrams illustrated in Figure 2.8. As we have seen before, due to the electrons being the only emitted particles, they must carry all the available energy (the Q-value of that reaction) as their kinetic energy. This is seen at the end of the spectrum in Figure 2.10.

2.4.2 $0\nu\beta^+\beta^+$ decay

In the neutrinoless double beta decay plus, the weak interaction transforms a nucleus (A, Z) into an nucleus (A, Z-2)[25]. This means that within the nucleus, two protons will transform in two neutrons with consequent emission of two positrons, but without the emission of any neutrino [68],

$$(A,\ Z) \rightarrow (A,\ Z-2) + 2\,e^+. \tag{2.28}$$

This type of decay occurs in proton rich nuclei, so that the ratio of protons to neutrons will be more stable. In this process, unlike the emitting neutrinos process, the positrons will carry all available energy, thus two monoenergetic positrons with the sum of their energies equal to the available energy are emitted. This emission is accompanied by four gamma-rays from the annihilation process.

2.4.3 $0\nu ECEC$ decay

In this mode, there are no leptons in the final state, so the energy released in this decay, in contrast to the other modes, has to be transferred to an excited nucleus [78]. This is illustrated in Figure 2.11 for the specific case of ^{124}Xe, where it is possible to see that the other modes decay most likely to the ground state of ^{124}Te. Whereas in the resonant neutrinoless double electron capture the ^{124}Xe nucleus decays to the excited state of ^{124}Te with (2790.41 ± 0.09) keV.

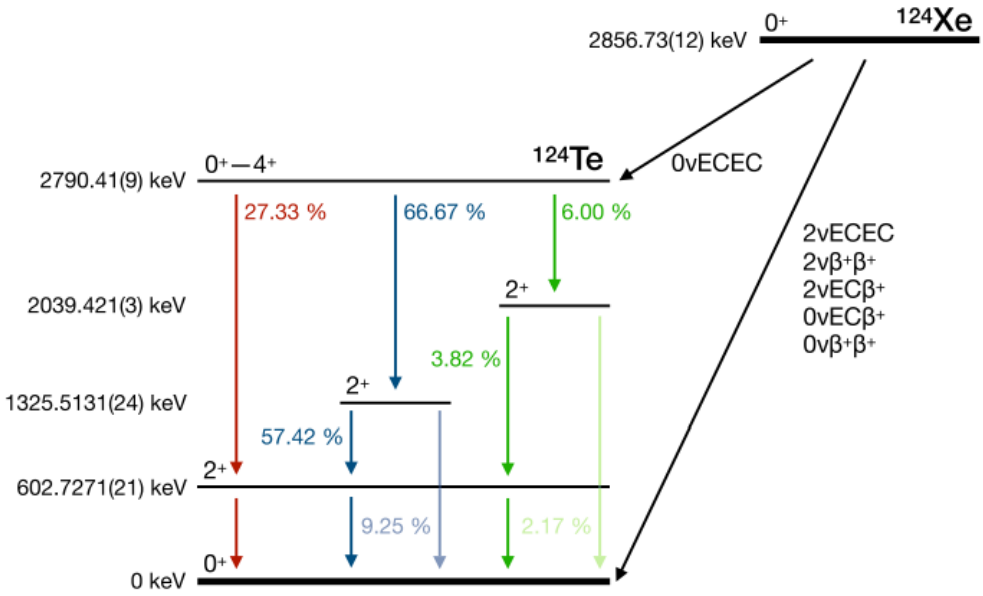

Figure 2.11: Decay scheme of ^{124}Xe. The other Double Beta Decay modes other than neutrinoless double electron capture decay most likely to the ground state of ^{124}Te, whereas in the resonant neutrinoless double electron capture the ^{124}Xe nucleus decays to the excited state of ^{124}Te with (2790.41 ± 0.09) keV. Figure from [79].

[25]Do not forget that all of these decays occur between isobar nuclei, so no exchange in the number of nucleons will happen.

Equation 2.29 [78] represents the resonant neutrinoless double electron capture, R0νECEC. The nucleus in the excited state, $(A,\ Z-2)^*$, will decay emitting gamma-rays [78]. Again, a cascade of X-rays and Auger electrons, X, will be originated due to the vacancy being filled by outer electrons,

$$2\,e^- + (A,\ Z) \rightarrow (A,\ Z-2)^* + 2X \rightarrow (A,\ Z-2) + \gamma + 2X. \tag{2.29}$$

In order for this process not to violate either energy or momentum conservation, the excited state has to fulfill the resonance condition in Equation 2.30 [78],

$$E_{exc,res} = Q - E_{e_1} - E_{e_2}, \tag{2.30}$$

where E_{e_1} and E_{e_1} are the binding energies of the two electrons absorbed by the initial nucleus (A,Z).

Usually, this mode would have an expected half-life decay time several orders higher than the neutrinoless mode with the lowest expected half-life decay time, the $0\nu\beta^-\beta^-$ decay, but the fulfillment of the resonance condition, presented in Equation 2.30, can diminish the decay half-life time up to a factor of a million [80]. Therefore, it becomes an exciting alternative channel to search for neutrinoless decay.

This process could be search by a low energy deposition, accompanied by one or more high energy gamma-rays, thus making the energy from the excited state of the tellurium.

2.4.4 $0\nu EC\beta^+$decay

In this specific mode, the treatment is almost identical as the ones presented in the previous sections. The big difference for the electron capture with coincident positron emission with neutrino emission is really that no neutrinos are emitted. If it exists, as in the other neutrinoless process, this is due to the Majorana nature of neutrinos, so they are their own antiparticle and will annihilate each other. Therefore, a nucleus will absorb an electron, again most likely from the K shell, and the two protons will transform into neutrons with the consequent emission of a positron [68],

$$(A,\ Z) + e^- \rightarrow (A,\ Z-2) + e^+. \tag{2.31}$$

Once more, due to a vacancy being created in the shell, an outer electron will fill this energetically favorable hole, thus originating a cascade of X-rays and Auger electrons. The distinction from the mode with emission of neutrinos is that the positron will carry all available energy, thus being a monoenergetic positron.

The signature of this process is a low energy deposition, accompanied by a highly energetic positron, and two gamma-rays with 511 keV.

Chapter 3

The LUX-ZEPLIN Experiment

The primary purpose of the LZ[1] experiment [83] is to study dark matter in the form of Weakly Interacting Massive Particles (WIMPs), one of the favorite candidates for dark matter. To achieve this, a very low background and a large target mass are required. So, the search for rare decays, as is the primary goal of this thesis, is also possible in this sort of experiment. The LZ experiment is located at a depth of 1478 meters, in order to diminish some of the backgrounds, namely, the cosmic ray muon flux is reduced by a factor of $\sim 10^6$ [84], at the Sanford Underground Research Facility (SURF) in Lead, South Dakota, USA [83].

3.1 Particle interaction in a liquid Xenon TPC

Before we describe the detector and the calibration processes, it is important to address an essential subject in this experiment: how particles interact with the detector medium. The dual-phase detector allows the detection of two signals, one in each phase, from the interaction of one particle with the medium. It will be measured firstly the primary scintillation signal (S1) in the liquid phase, and later the secondary scintillation signal (S2) will be measured in the gas phase [85].

When an incoming particle interacts with the detector's medium, xenon atoms in the case of LZ, either a NR or an ER can occur [85]. Before we discuss what follows these recoils we must understand these two processes, and after settling the foundations about the energy deposition and the procedures revolving the S1 and S2 signals detection, we shall discuss how can those two processes be distinguished in this experiment using those signals. The name of both the processes is very well self-explanatory, but NR is an interaction between a particle and the whole nucleus, where this interaction will cause a recoil of the nucleus. A WIMP particle is regarded as a chargeless particle, so it would not interact with an electron, therefore a NR is the expected interaction for WIMPs. An ER occurs when a particle interacts only with an electron of the medium.

We know that an interaction can cause a NR or an ER. In both cases, this energy deposition will excite or ionize the atoms that are close. However, when NR occurs another process will also consume this energy, heat, and it is due to atomic motion[2].

[1] This experiment is the result of the combination of two previous experiments, Large Underground Xenon (LUX) [81] and ZonEd Proportional scintillation in LIquid Noble gases (ZEPLIN) [82]

[2] As a matter of fact, in an ER event energy is also dissipated as heat but it is a smaller fraction than NR.

We shall discuss these processes in an isolated view regarding this experiment, and after that, it will be addressed in the context of the LZ experiment. In Figure 3.1, a scheme to illustrate these processes is presented.

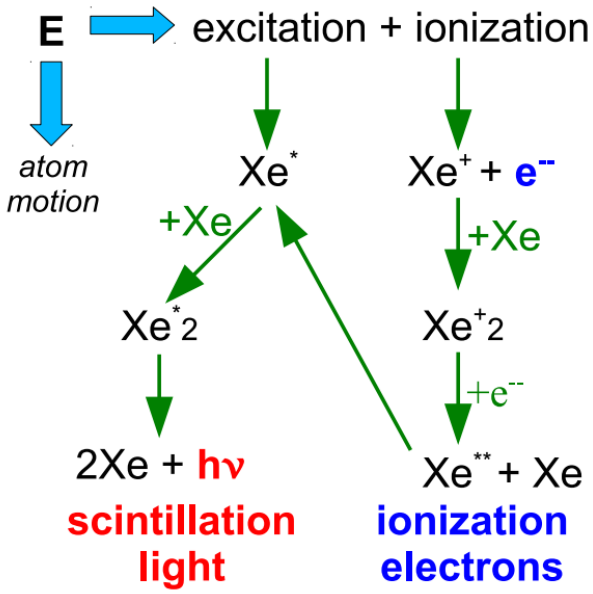

Figure 3.1: Schematic representation for the processes that occur after an interaction in xenon. The inner transformation that can happen in each of the processes leading to the scintillation light and to the ionization electrons is also represented. From the three possible processes only excitation and ionization can be detected, so the energy dissipated by heat is lost in these detectors. Figure from [86].

We will start with the process that requires less energy, which is excitation[3]. An excited dimer, Xe_2^*, results from the interaction of the excited atom with a neighbor xenon atom. From the de-excitation of this dimer to the ground state, a $\sim$ 175 nm photon (VUV) is emitted [87]. Regarding the ionization process, we can have two possible outcomes. After the ionization process, we are left with a xenon ion and an electron. Despite being separated, they still have a very strong electric attraction towards other particles nearby that have their opposite charge. It is at this step that the two possible outcomes come into play. On one hand, we have the case where the two particles do indeed recombine, where this would be remitted to the previous case of excitation. On the other hand, these particles do not recombine. The probability of the latter case is enhanced by the use of an electric field [85]. Therefore, the electrons will drift away on the contrary direction of this applied field.

With all this knowledge of xenon interaction in our mind we can now go forward, and apply this to the specific case of all xenon TPC. Through this, we will be able to understand very well the two signals detected, S1 and S2. The first signal measured is the prompt scintillation signal, denominated as S1, which is caused by the 175 nm photon emitted in the de-excitation process that makes up the excitation part of the previous analysis. Nevertheless, we know this will not be the sole contributor to the S1 signal. We

[3]From now on, heat will be disregard because the energy that was dissipated through it can not be detected with this detector technology.

have seen that when recombination between xenon ions and electrons occurs, they will be sent to the excitation path. Therefore, they will further contribute to the S1 signal.

After this, we are left only with the electrons deriving from the ionization process that do not recombine. Due to the difference in the gate and cathode grid's potential that we shall discuss in Section 3.2, a downward electric field will be created in the drift region. On a large scale, this field prevents the recombination of the electrons with the atoms, drifting them to the gas-phase frontier. At that place, they will be extracted due to a very strong extraction field between the gate and the anode. Furthermore, they will accelerate upwards, due to a electroluminescence field, and the photons originated from them will produce the electroluminescence signal [87], denominated as S2. The number of photons produced, in the gas phase, per unit distance traveled in xenon is usually parameterized as [88]:

$$\frac{dN_p}{dx} = \alpha E - \beta P - \gamma, \tag{3.1}$$

where E is the electric field, P is the pressure, and α, β, and γ are empirical constants that for xenon assume the values 0.137 V^{-1}, 177 bar^{-1} cm^{-1}, and 45.7 cm^{-1}, respectively [89]. This interaction process can be seen in Figure 3.2, where it is also shown that the S1 signal is very small relative to the S2 signal, while the delayed secondary S2 is larger and also a wider signal.

These two signals are the cornerstones of this experiment. From them, a larger part of further analysis is done, namely the position of the interaction and the energy. The depth of the event will be given by the difference in time between S1 and S2 signals, whereas the x and y positions will be achieved by analysing the pattern of the S2 signal in the top PMT array [91].

In this section remains to be discussed two brief topics. Firstly, as promised, it is time to understand how these two signals can help us distinguish an ER from a NR. Then, lastly, we shall see the application of these signals into one of the most important aspects of any physical search: energy reconstruction.

One key aspect of WIMP search experiments is the discrimination between ER and NR. This distinction is made through the S1 and S2 signals. To achieve this is essential to measure the difference in the ratio of ionization electrons to scintillation photons that emerge from the interaction with either the nucleus or an atomic electron. From this, the two signals can be obtained, and a graph like the one in Figure 3.3, that was created in the LUX experiment, can be made. When the graphic of the logarithm of the ratio of S2 over S1 as a function of S1 is done, we observe two distinct bands, therefore the position of an event in that phase space can be used to discover the nature of the recoil.

Analysing Figure 3.3, we can clearly see big differences between the two bands. Comparing both the solid blue and red lines that represent the ER and NR band medians, respectively, it is obvious that the ratio of S2/S1 for the ER is higher than the one for NR. Therefore, ER and NR can be distinguished by the separation of the bands as well as their widths. We do know how can they be discriminated one from the other, but we have not discussed yet the physical reason behind this.

If we compare two recoils, one electron and other nuclear, with the same energy it is very obvious that the ER will go further. Therefore, in an NR the local charge density will be higher, thus facilitating ion-electron recombination. If the reader has not yet forgotten, more recombination means that will exist fewer free electrons to drift

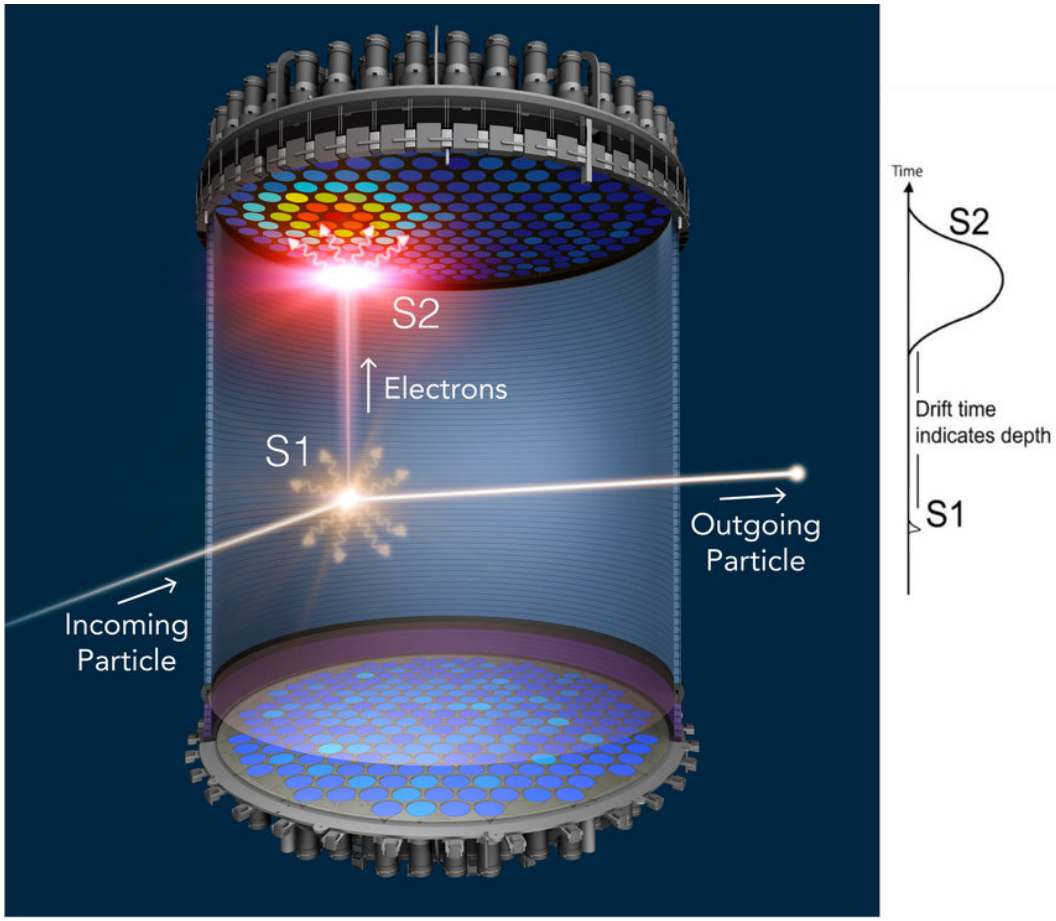

Figure 3.2: Representation of the working principle of a dual-phase TPC. From the interaction of an incoming particle with a xenon atom, a prompt scintillation signal, S1, will be measured. Alongside that, ionization electrons will be also produced and will drift in the upward direction due to the electric field. They will drift until they arrive to the liquid/gas frontier, where a stronger electric field will extract them to the gas phase. They will accelerate in the gas phase creating electroluminescence, and thus the S2 signal. Figure from [90].

upwards to the gas phase, where they will contribute to the S2 signal. Adding to that, the recombined atoms further contribute to the S1 signal, as we previously discussed. Therefore, in an NR is seen an increase in the S1 signal and a decrease in the S2 signal if compared to the ER. This means that a reduction in the S2/S1 ratio is observed in the NR, thus explaining what we observe in Figure 3.3.

In a general manner, energy is a crucial aspect of any experiment, but in experiments that allow for rare decay searches its importance increases considerably. Therefore, a good understanding of the energy dynamics in the system is essential, thus the necessity for optimized energy resolution. An excellent energy resolution is a key step in the right direction in the search for rare decays. Logically, one of the biggest applications of S1 and S2 signals is energy reconstruction.

It is necessary to introduce two factors, g_1 and g_2, to achieve this energy reconstruction. The g_1 factor [85] is the probability that the detector registers an emitted photon, or if you will it is the average fraction of S1 scintillation photons that are, indeed, de-

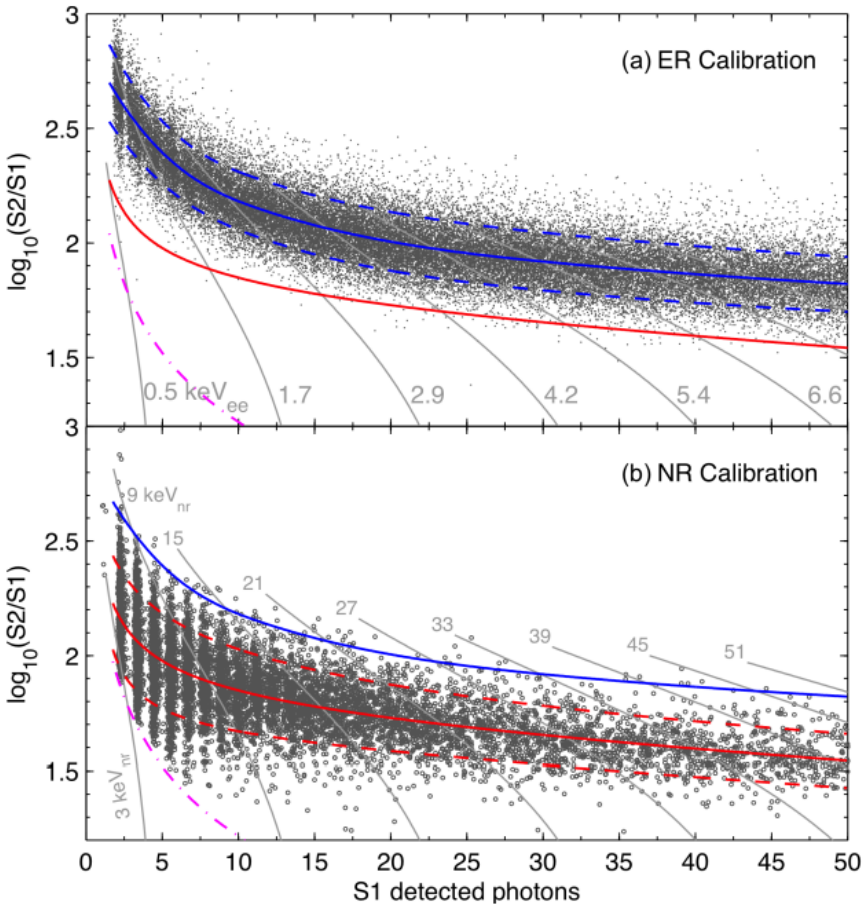

Figure 3.3: Representation of $\log_{10}$(S2/S1) as a function of the S1 signal obtained with LUX calibration. In the a) graph the ER response was calibrated using a tritium source, whereas in the b) graph it is shown the NR calibration using a deuterium-deuterium neutron source. The median for both bands are represented with solid line, blue for the ER and red for the NR. The dashed lines indicate the 80% population contours of the bands, again with the same colors as the median. The vertical gray lines are the contours of constant energy deposition, whereas the pink line represents the S2 threshold in that analysis. Figure from [90].

tected. Whereas, the g_2 factor [85] is the product of the quantity of detected light for each extracted electron from the liquid surface by the probability of extraction to the gas phase of an electron that arrives at the liquid surface. These two factors will be correlated to the S1 and S2 signals through n_γ and n_e, which represent the initial number of photons and electrons produced by the interaction in the medium, respectively. These relations are expressed by [92]:

$$\langle S1 \rangle = g_1 \, n_\gamma, \tag{3.2}$$

$$\langle S2 \rangle = g_2 \, n_e. \tag{3.3}$$

Since energy can be also expressed using n_γ and n_e [92]:

$$E = W \, (n_\gamma + n_e), \tag{3.4}$$

where W is the average required energy to create a quanta in xenon, either a photon or an ionized electron. It is now very easy to conclude a final expression to reconstruct energy using the previous equations [85]:

$$E = W \left(\frac{S1}{g_1} + \frac{S2}{g_2} \right). \tag{3.5}$$

The g_1 and g_2 factors are calibrated during the experiment normally resorting to what is called a Doke plot, where it can be seen that their values can slightly change during the acquisition period. The value used for W is 13.7 ± 0.2 eV [93]. This is the final energy expression that I will use in the next chapters to reconstruct energy, however, for a NR event, this expression will slightly change its shape. It is expressed as [94]:

$$E = \frac{W}{\mathcal{L}} \left(\frac{S1}{g_1} + \frac{S2}{g_2} \right), \tag{3.6}$$

where $\mathcal{L}$ is the Lindhard factor [95] which is an intrinsic property of xenon, that basically estimates, in a NR event, the amount of energy that will be available to produce ionization and excitation. That means the energy deposited that is not dissipated through heat. Therefore, from what was said before about ER, it is understandable the fact that this factor can be overlooked in the energy reconstruction of this type of event.

3.2 The LZ detector

LZ features a dual-phase (liquid-gas) xenon TPC filled with 7 tonnes of liquid Xenon (LXe) in the active region. Surrounding this TPC, we have elements as veto detectors, such as the skin and the outer detector, and if we go further out we have a water tank in order to suppress the background to a greater extent, as we can see in Figure 3.4.

I have been mentioning the term dual-phase, but remains to be discussed the specification of this, and more important the reason behind its use. Through this kind of detector, particle interactions produce two signals, one in the liquid phase and the other in the gas phase [83] as we previously saw, and from this a full reconstruction of the event is possible [88].

It is yet to be analysed why are we using a liquefied noble gas such as xenon as a target. It is now time to understand the reason underneath almost every experiment chasing WIMPs in higher masses today uses this type of method. Due to the high density of LXe, ∼3 g/cm^3 [90], it is possible to construct a relatively small detector with a large target mass that otherwise would not be possible. This also allows scaling to large detector masses with ease[4]. We can clearly see this from our case in specific because the LUX experiment used 300 kg of xenon [81] and in the LZ experiment we use 10 tonnes of the same element [83]. One important quality of xenon is that it has great self-shielding properties [91]. By this I mean that there will be a region within this volume of xenon where the background is considerably reduced, due to its high density and high atomic (Z=54) and mass (A=131) numbers. So, it is normal to define a fiducial volume (volume where the background is lower), with the intent of doing this kind of search with a much

[4]This is obviously if we do not consider the cost, then unfortunately it is no longer easy and quickly, but remains easier than the rest.

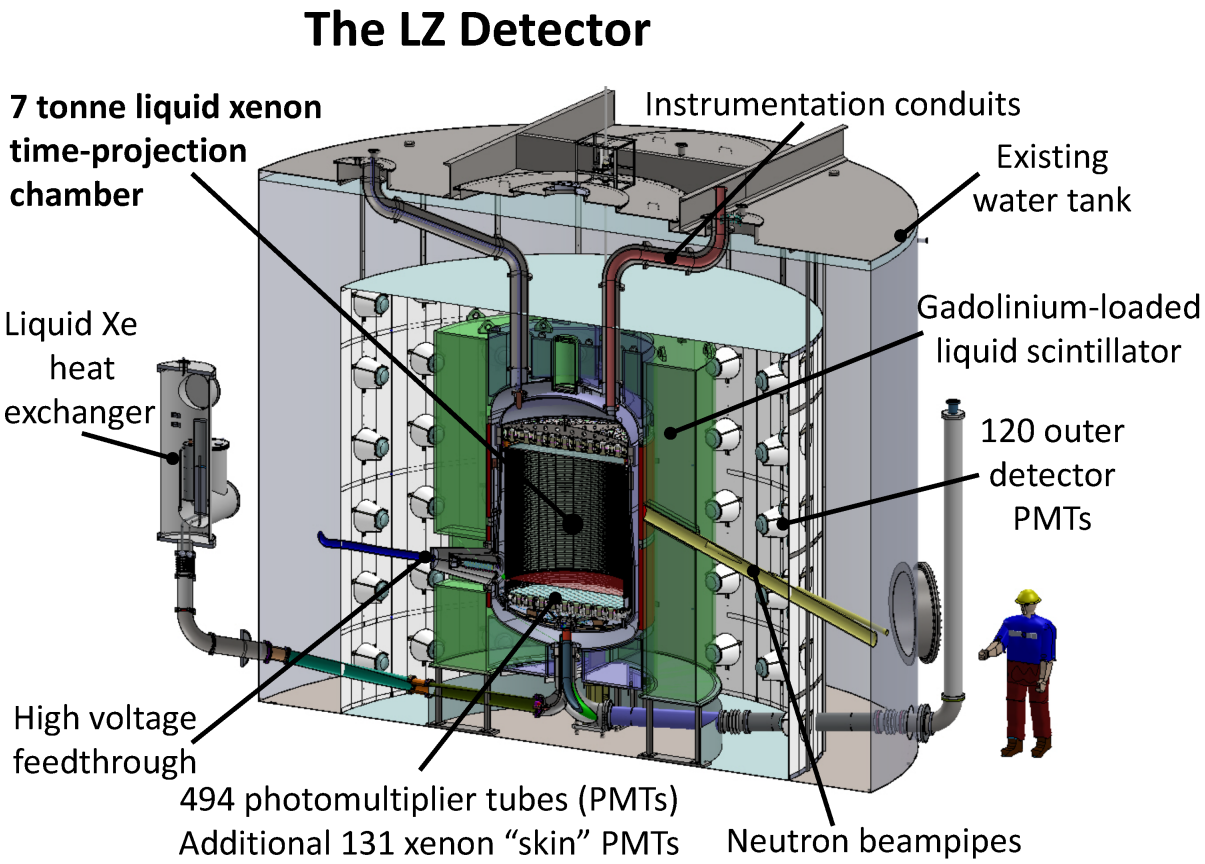

Figure 3.4: Diagram of the LZ detector. The main xenon detector (TPC) and the skin are in the center observed by a total of 625 PMTs. They are surrounded by the outer detector in green and further by the water tank. Figure from [87].

lower background. In the LZ experiment, this fiducial volume is about 5.6 tonnes for the region of low energy depositions [85].

Despite of this self-shielding, it is very important to guarantee that these ultra-sensitive experiments have a very low background. Then, it is critical that the medium where the interaction takes place, xenon, can not be very radioactive, in order to minimize the intrinsic background[5]. Natural xenon[6] is constituted by 9 isotopes; from these, 7 are stable and there are 2 unstable[7]. One of them is the focus of this work, ^{124}Xe, which, for instance, decays by double electron capture and has a measured long half-life, 1.8×10^{22} yr[8] [93]. The other one, ^{136}Xe, which was the first xenon isotope known to decay, does it through double beta minus decay with a half-life of 2.11×10^{21} yr [96]. Despite this, ^{124}Xe and ^{136}Xe only represent about 0.095% [92] and 8.857% [97] of natural xenon, respectively. So, this medium still obeys the criteria established for the background.

[5]Has we shall see, previously to the construction, there were a thorough material selection to this end.

[6]In this point, we will ignore synthetic isotopes.

[7]Actually, in reality, ^{126}Xe and ^{134}Xe are very likely to be unstable, however they decay with half-lives much longer than these ones.

[8]In the final stages of this dissertation, a new value for the half-life of this decay was released, 1.5×10^{22} yr, however it will only be used in the comparison with our final value.

These are not the only advantages of using xenon as a target mass for the TPC. Among other qualities, it can be purified very efficiently [85], thus removing contaminants. In addition, this kind of experiment is very sensitive, in part due to its very low energy threshold, which is originated from xenon being a bright scintillator.

Regarding the veto detectors in this experiment, we have the xenon skin and we have the outer detector. Through these veto systems, it is possible to reject a significant part of backgrounds. This allows us to choose a much larger fiducial volume, 5.6 tonnes, instead of the 3.2 tonnes region that would be the case if there was not this veto system [87]. Therefore, we would lose more than half of the total mass in our experiment making this search even more difficult.

After we lay down some of these aspects that were important before we start our analyses, we can now dive deeper into the constituents of this detector.

3.2.1 Dual-phase TPC

The TPC contains 7 tonnes of xenon in the active region, but after fiducialization we got a region of approximately 5.6 tonnes. The xenon contained in the TPC is the target mass for the particles, and it has 145.6 cm in height and diameter [88]. The setup of the LZ TPC that we will describe is illustrated in Figure 3.5.

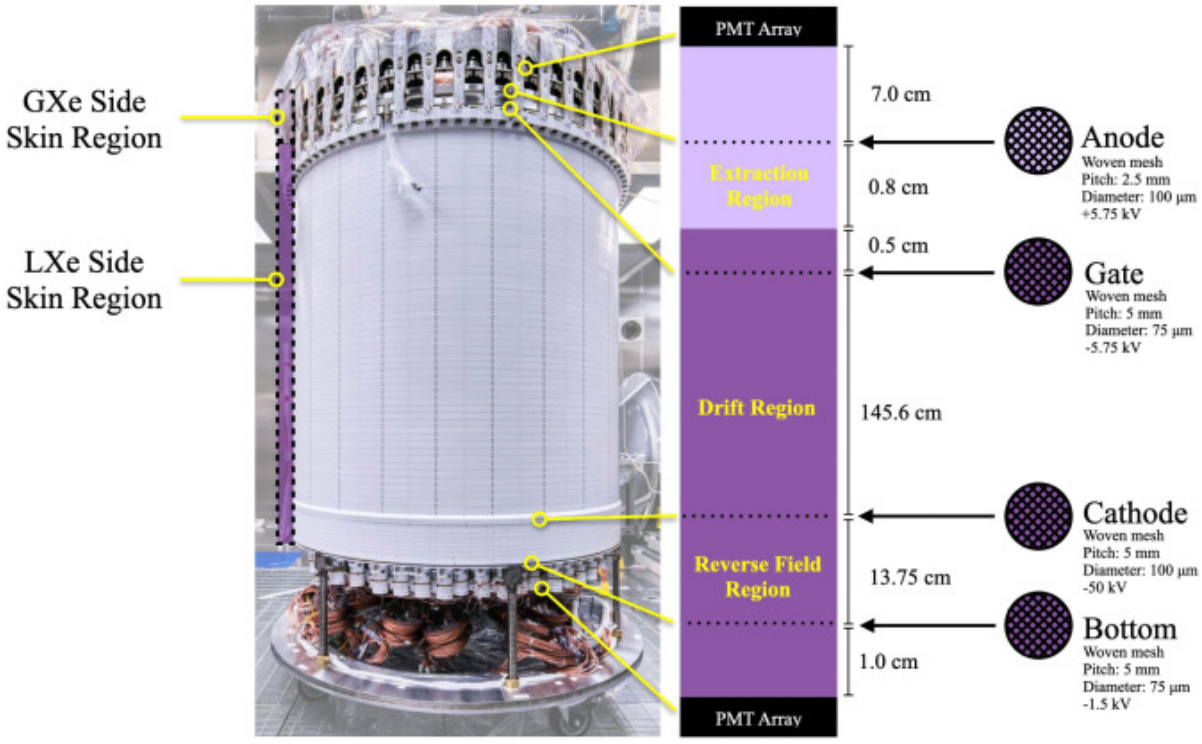

Figure 3.5: Fully assembled TPC with the four different grids identified. The two arrays of PMTs are represented, with the light purple representing the gaseous phase and the dark representing the liquid phase. The three different regions with different fields are also depicted. Figure from [88].

The scintillation signals, created in the active region by the interaction of particles with the xenon atoms, are viewed by two arrays of 3–inch diameter Hamamatsu

R11410-22 PMTs. The top array has 253 PMTs disposed in a hexagonal-circular hybrid configuration, whereas the bottom array has 241 PMTs layed out in a hexagonal pattern, making a total of 494 PMTs [87]. Due to the scintillation signal being more challenging to detect than the electroluminescence one [90], the optical design of the TPC has to maximize their detection. Therefore, the TPC and the non-sensitive detector components are covered by Polytetrafluoroethylene (PTFE). The PTFE used in this experiment was Technetics 8764, and its reflectivity was measured to be 97.3% when immersed in LXe [83].

After the interaction occurs, a fraction of the electrons will be liberated, and they will drift away from the location of the interaction toward the gas region. Later, in the extraction region, they will be extracted from the liquid phase to the gas phase. In order to this become true, a downward electric field must exist, so the electrons drift upwards. Another strong electric field must also be localized in the extraction region, making the extraction to the gas phase possible. The first one is called drift field and the latter is the extraction field. In this experiment, three electrode grids are used to achieve this. These grids are called the anode, gate and cathode grids, and they are identified in Figure 3.5. Since the bottom PMTs could not operate close to the high potential of the cathode [88], then another grid, the bottom grid, is required between these two components. This last one operates at a much lower potential than the cathode. Between the cathode and this bottom grid is what is called the reverse field region, with a strong field (3.5 kV/cm [88]) in the upward direction and 13.75 cm of height.

Above the reverse field region, we have the drift region, it is in this 145.6 cm long region where the interaction occurs and from where the electrons drift away due to the electric field. This region is bounded by the gate grid at the top and the cathode grid at the bottom. The potential used for each grid can be changed, as we will see in Section 3.4, thus the fields created due to these potential differences can also be varied. All the values mentioned during this section will be the values initially thought to be used, however, in Section 3.4, we will discuss the values used during the SR1. The former is 0.5 cm below the separation of the gas-liquid phases and operates at -5.75 kV [88]; the latter is also localized in the liquid phase[9], and operates at -50 kV [88]. So, if we do the calculation by making use of the potential difference between these two grids and the distance separating both of them, we can obtain the strength of the electric field created in this region. It is approximately a 304 V/cm[10] [88] electric field, with a downward direction.

The next region is the extraction region, which is where the electrons will be extracted to the gas phase. This is possible through the extraction field created due to the potential difference between the anode and gate grids. Both usually operate with the same absolute potential, but with different signs. The anode operates at 5.75 kV [88], whereas the gate operates at -5.75 kV [88]. In this region, we have an extraction field with 5 kV/cm in the liquid phase and 10 kV/cm in the gas phase (electroluminescence field) [88].

3.2.2 Xenon Skin

The TPC is not the only place where LXe is present in this experiment. Beyond the quantity in the TPC, there are also 2 tonnes of xenon placed next to it, in the denominated skin, as is illustrated in Figure 3.6. This skin surrounds the TPC, and

[9] As we can see by Figure 3.5, the only grid localized in the gas phase is the anode grid.

[10] In this calculation we divide the potential difference of the grids by the distance between them.

to ensure that both of them are at a constant temperature[11], they are enclosed in a low radioactivity titanium inner cryostat vessel. This cryostat is placed inside of an outer cryostat vessel, also made from low radioactivity titanium. These two cryostats are separated by a vacuum region for thermal insulation.

The xenon skin region ensures dielectric insulation between the TPC and the inner cryostat vessel, and is extremely useful to detect coincident gamma-rays, so it will be the innermost veto detector [90].

This skin [90] is divided into two regions, a side skin with 4 cm of LXe at the top of this region and 8 cm wide near the cathode, and a dome skin region below the TPC. Different PMTs are used in the skin with respect to the TPC. In the side skin, two types of PMTs are used. The top half is viewed by 93 1-inch Hamamatsu R8520-406 PMTs, whereas in the bottom half is used a 20 2-inch R8778 assembly. In the dome region, 18 of the latter type of PMTs are also used, and we can see in Figure 3.6 how the lower side and dome regions' PMTs were assembled.

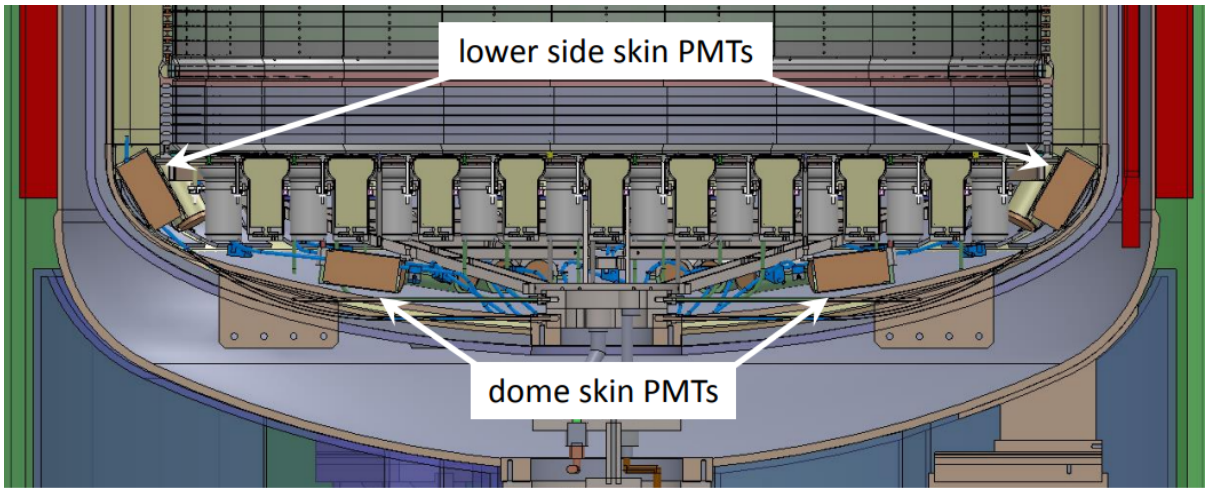

Figure 3.6: Assembly of the PMTs in the lower side and dome skin regions. Figure from [90].

3.2.3 Outer detector

Surrounding all the detector elements mentioned up to now, namely the outer cryostat vessel, we have an outer detector. It is filled with 17.3 tonnes of gadolinium-loaded liquid scintillator, where the liquid scintillator, in this case, consists of a linear alkyl benzene solvent doped at 0.1% by mass with gadolinium. This liquid is distributed inside the 10 acrylic vessels that constitute the outer detector [90]. The structure of the outer detector is illustrated in Figure 3.7, where we can see the 3 vessels on the bottom and the 2 on top all in blue, the 4 larger vessels on the sides in green, and finally, water displacers in red.

As in the other veto detector, in this case, the main goal of the outer detector is also to diminish the background. Specifically, neutrons associated with nuclear recoils in the

[11]By this I mean that they will be thermally isolated, and cooled using liquid nitrogen thermosyphons to make sure it is maintained at ∼175 K.

TPC, which is the same process assigned to the signal by WIMPs. Thus, these particles would raise the background levels of our search.

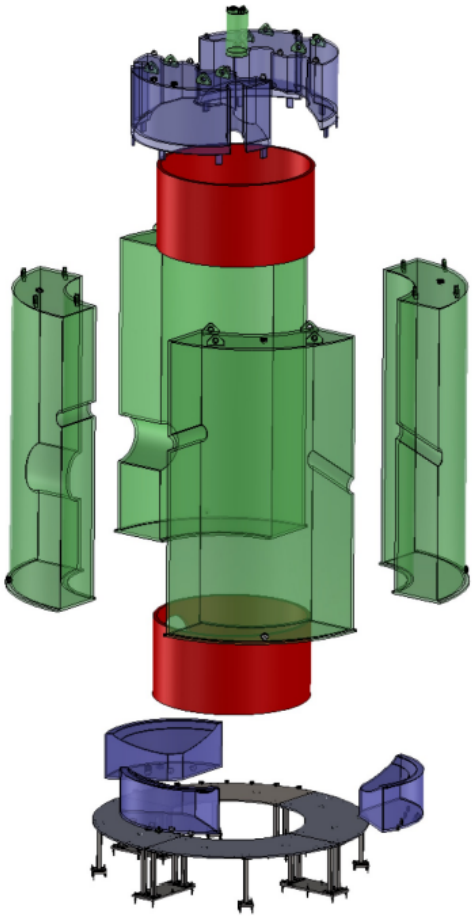

Figure 3.7: Illustration of the outer detector, with its constituents: 3 vessels on the bottom and the 2 on top all in blue, the 4 larger vessels on the sides in green and finally water displacers in red. Figure from [90].

In this experiment, neutrons for the most part are detected via capture of the isotope ${}^{155}_{64}\mathrm{Gd}$ after thermalising in the scintillator, given by Equation 3.7 [83], and ${}^{157}_{64}\mathrm{Gd}$, presented in Equation 3.8 [83],

$$ {}^{155}_{64}\mathrm{Gd} + {}^{1}_{0}\mathrm{n} \rightarrow {}^{156}_{64}\mathrm{Gd} + \gamma, \tag{3.7} $$

$$ {}^{157}_{64}\mathrm{Gd} + {}^{1}_{0}\mathrm{n} \rightarrow {}^{158}_{64}\mathrm{Gd} + \gamma. \tag{3.8} $$

From these processes, a gamma-ray cascade is emitted with 7.9 MeV and 8.5 MeV in total, respectively [83].

Further scintillation caused by these particles emitted is going to be viewed by a set of 120 Hamamatsu 8–inch R5912 PMTs placed in the water tank. This water tank has a diameter of 7.62 m and 5.92 m in height, filled with 228 tonnes of pure water [90], this tank can also be seen in Figure 3.4. The water tank surrounds all of this experiment's detectors, and its primary purpose is to diminish further the background caused by gamma-rays and neutrons and is used as a Cherenkov muon veto detector.

3.3 Detector calibrations

We have now described the detector, and in this section, we will see how we can interpret its results. In order to achieve this, a set of calibrations were used during the time of this experiment. Previous to its application, these calibrations were simulated for the sake of a better understanding of the sources used and results.

The main goal of this specific process is to get to know our detector very well, namely, to understand the interaction of particles and the properties of these interactions. The interaction of a dark matter particle is regarded as causing a nuclear recoil [87], so one of the main focuses of these calibrations is to examine the electron recoil and nuclear recoil responses.

In this section, we will see internal sources, and gamma-ray and neutron external sources. Internal sources are dissolved in the LXe, external sources of gamma-rays are encapsulated and placed inside the outer cryostat using one of three source tubes [90]. We can resort to neutron sources in two different modes, through external sources or using beam sources where energetic particles situated outside of the detectors are fired [90]. Some of the sources used in these calibrations are listed in Table 3.1.

Table 3.1: Different calibrations sources used in LZ, alongside its deployment strategy, type of emitted particles and half-life decay time. Table adapted from [90].

Source	Deployment	Type	Half-life time
CH_3T	Internal	β	12.3 y
^{83m}Kr	Internal	β/γ	1.83 h
^{131m}Xe	Internal	γ	11.8 d
^{220}Rn	Internal	$\alpha/\beta/\gamma$	10.6 h
^{241}AmLi	External	Neutron (α, n)	432 y
^{252}Cf	External	Neutron (fission)	2.65 y
^{57}Co	External	γ	0.74 y
^{228}Th	External	γ	1.91 y
^{22}Na	External	γ	2.61 y
^{88}YBe	External	Neutron (γ, n)	107 d
^{124}SbBe	External	Neutron (γ, n)	60.2 d
^{205}BiBe	External	Neutron (γ, n)	15.3 d
^{206}BiBe	External	Neutron (γ, n)	6.24 d
DD	Beam	Neutron	—

3.3.1 Internal sources

In every experiment, there is always a certain level of compromise when the constituents of the detector are selected. All components have good qualities that are going to help us in this search, but they will also have downsides. As we know, the LXe has excellent self-shielding qualities [91], allowing the existence of a central region with very low background. Without this, a dark matter search would be much more difficult, however, if we want to make electron recoil calibrations within this volume at low energies[12], an external source would be an impractical solution. This is the outcome of the self-shielding qualities of our xenon, therefore gaseous sources are mixed with the LXe so they mix uniformly and can reach the innermost region of volume [90].

Tritiated methane, CH_3T, is an essential calibration source to understand the detector's response at low energies [90], in the WIMP search region. A set of energies are accessible to this source, ranging from 0 keV up to its endpoint localized at 18.6 keV [90]. From its long half-life time, 12.3 y [98], arises two important properties of this compound. First of all, because of this long decay time, it will be practically unchanged after the calibration time. Therefore, it will have time to spread uniformly in the volume[13], an important condition to study the detector's response [90]. However, if not completely removed, it would represent a long-term background for this experiment. Fortunately, the getter, which is responsible for the purification of the xenon and during the SR1 the full xenon was continuously purified at 3.3 tonnes/day, can efficiently remove this compound after being used in calibrations [90].

The remaining three internal sources ^{83m}Kr, ^{131m}Xe, and ^{220}Rn have a much shorter half-life time. Their parent nuclides are stored in a compact form and emanate these calibration sources [83]. We used ^{83}Rb, ^{131}I, and ^{228}Th as parents of ^{83m}Kr, ^{131m}Xe, and ^{220}Rn, respectively [83]. ^{83m}Kr is used to calibrate position response, however, due to its two consecutive decays [90], recombination response and electric field calibrations are also possible. These two decays occur with a decay half-life of 154 ns [90]. It has a very short half-life decay time, 1.83 h [90], so this source may not be able to distribute itself uniformly. So it is not the best calibration source for the position reconstruction, as we discussed in the tritiated methane case. For this reason, another source, ^{131m}Xe, is also used due to its longer half-life time, 12.0 d [99]. This is a more suitable candidate for a fully evenly distribution through the active volume of LXe. However, this is a source with a single energy line at 164 keV [90] instead of the 41 keV [90] of the previous source. Lastly, a ^{220}Rn source is also used, mainly to calibrate the S1 signal in the xenon skin region.

3.3.2 Gamma-ray external sources

A vacuum region separates the inner cryostat vessel from the outer cryostat vessel. In this region, there are three source tubes, which are used to transport the external sources. These sources can be moved up and down within these tubes through a deployment system and will have a precision in their final position of ± 5 mm [90]. This precision will be very important, as we shall see briefly.

[12] This kind of calibrations are usually made at low energy regions, in the WIMPs search regions.

[13] As we shall see in the later chapters of this thesis, during SR1 a mixing problem in xenon was detected, so maybe it will not be a totally uniformly source.

We have discussed the influence of the self-shielding properties of xenon in the external sources. Despite this, calibrations using external gamma-rays have a relevant role. Especially in the outer detectors and near the TPC walls [90]. A ^{228}Th source of 2.615 keV [83] is used in signal fidelity calibrations in the further out region of the TPC and calibrations in the outer detector.

An important calibration is the calibration of the energy scale, where a study of the z position as a function of the number of measured photons detected is made. In Figure 3.8, we can see this study made for the outer detector, where a ^{228}Th source was used, and the number of measured photons detected as a function of z position for the skin, using a ^{57}Co source. Therefore, it is evident the necessity for good precision in the final position of the source.

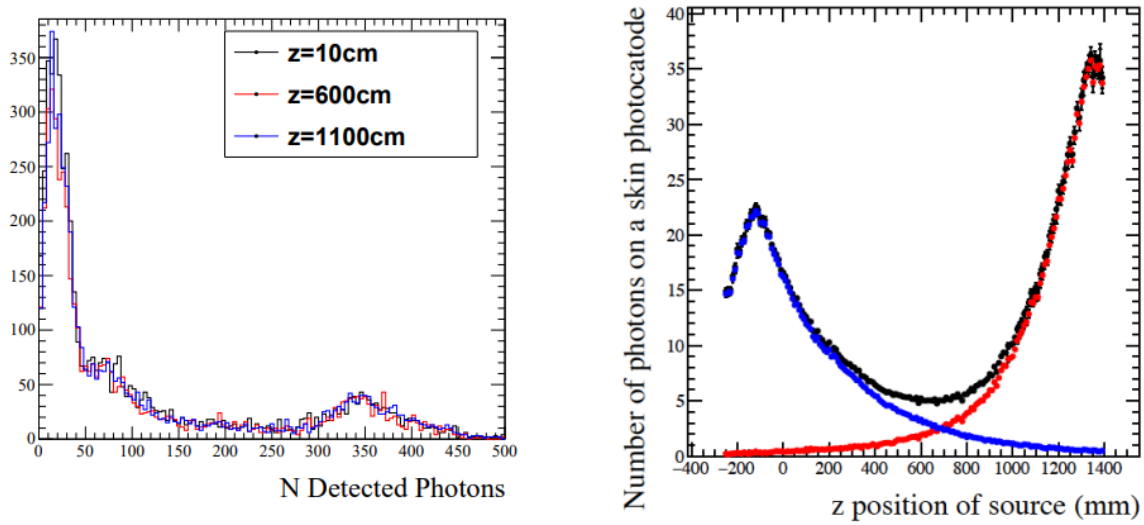

Figure 3.8: Energy scale study as a function of the number of photons detected, for three different z values, using a ^{228}Th source for the outer detector on the left. Number of photons detected versus z position, using a ^{57}Co source in the skin. Figure from [90].

The remaining source, ^{22}Na, produces back-to-back 511 keV gamma-rays [83], due to positron annihilation, in its decay process. Since they can be seen in the outer detector, in the skin and in the TPC, it allows for timing calibration between the three detectors.

3.3.3 Neutron sources

Calibrations using neutron sources are one of the most important types of calibrations [90]. In the specific case of a rare decay study, as is intended in this thesis, they become the most concerning one, since neutrons enter our detector. This importance arises from the neutron activation, in xenon isotopes, namely in ^{124}Xe which is the main topic of this thesis. From this activation, an increment of the background will be observed in the region we are interested in [93], as will be discuss in Chapter 5.

These sources break into three larger groups: (α, n) sources, photoneutron sources and deuterium-deuterium neutron sources [90]. This experiment makes use of (α, n) reactions, and more specifically the ^{241}AmLi source, which is a really good neutron source in calibrations regarding dark matter. The main reason for this is the endpoint for the

neutron in Equation 3.9 [83], which is near 1.5 MeV [83], so it is considered a value somewhat low. It will be such a good dark matter calibration source since the nuclear recoils yielded in this reaction are predominantly in the dark matter search region [90]:

$$\alpha + {}^{7}\mathrm{Li} \rightarrow {}^{10}\mathrm{B} + n. \tag{3.9}$$

Photoneutron sources on the other hand, utilize (γ, n) reactions in order to produce neutrons. The reaction of these processes that use beryllium, as is the case of all these sources, is given by Equation 3.10 [83],

$$\gamma + {}^{9}\mathrm{Be} \rightarrow {}^{8}\mathrm{Be} + n. \tag{3.10}$$

These sources generate almost monoenergetic[14] neutrons with low energy equal to 152 keV, 22.5 keV, 88.5 keV, and 47 keV for the ^{88}YBe, ^{124}SbBe, ^{205}BiBe, and ^{206}BiBe sources, respectively [83]. They are used to calibrate nuclear recoils at low energy ranging from below 1 keV to near 4.6 keV [83]. It is a vital calibration because it is localized in the expected energy depositions of coherent scattering from ^{8}B solar neutrinos [83]. Through this type of calibration, we can understand the response of the detector and avoid another relevant background to this experiment because they can be mistaken with WIMPs. However, usually the cross-section of this type of process, (γ, n) reactions, is very small [90]. So, very strong sources are required to create a sufficiently large neutron flux. However, due to the high activity, there is an absurd number of gamma-rays, near 10^4 gamma-rays for each neutron emitted [83]. This would result in a significant background if it was not for the tungsten shielding that reduces the gamma-ray rate to the detector.

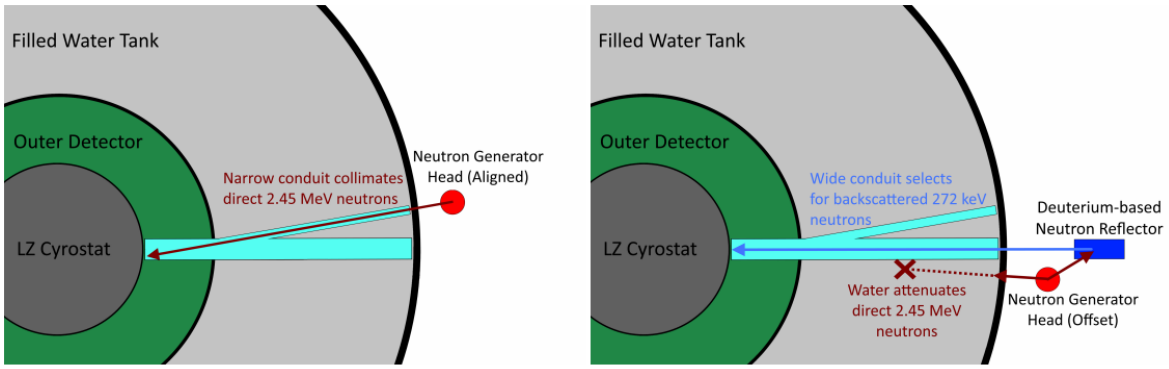

Figure 3.9: Setup of the deuterium-deuterium neutron source with its two neutron conduits. Using the leaning conduit, the neutrons with 2.45 MeV go directly from the generator to the detector, on the left image. On the right, we have the alternative layout where the initial 2.45 MeV beam will be reflected in deuterium oxide, D_2O, thus resulting in 272 keV quasi mono-energetic neutrons. Figure from [90].

Continuing in the field of nuclear recoil calibrations, we have the last type of calibration source that we will look at, the deuterium-deuterium neutron source. In LZ an

[14]These neutrons are almost monoenergetic, because they only have a slight angular dependence in their energetic value. This is calculated through the expression [90] $E_n(\theta) = \frac{M(E_\gamma - Q)}{m+M} + E_\gamma cos(\theta)\sqrt{\frac{(2mM)(E_\gamma - Q)}{(m+M)^3}}$, where m is the mass of the neutron and M the mass of the nucleus. The energy of a neutron emitted at $\theta = 0\,^\circ$ and $\theta = 180\,^\circ$ differ with 4.6 %, thus we can consider these neutrons as monoenergetics.

Adelphi Technologies DD-109 deuterium-deuterium neutron generator was used, which is capable of generating 10^9 neutrons per second [90]. They are monoenergetic neutrons with an energy of 2.45 MeV [90] and will make their way into the xenon volume through two conduits, as shown in Figure 3.9. These conduits will be filled with water during WIMP search, whereas during calibrations they will be filled with nitrogen [90].

The deuterium-deuterium neutron source can be used directly as we can see on the left side of Figure 3.9. Another method is that the neutrons emitted in this source with 2.45 MeV can be reflected into a deuterium oxide target, D_2O, and then collect the neutrons that are reflected at a near-180 degree angle, as is illustrated on the right side of that figure. Through this, they will become a quasi-monoenergetic neutron beam with an energy of 272 keV. Thus, a new lower nuclear recoil energy region will be available, with smaller uncertainties.

3.4 Science Run 1

The commissioning stage, where we try to understand our detector, ended at the end of November. After that, the WIMP search in the SR1 started on December 23rd 2021 and ended on April 18th 2021. During that stage, the detector was stable, and the parameters were kept constant. This first Science Run was intended to be short, the main goal was to observe the quality of its results and see if the detector was running smoothly. After this short first one, others Science Runs will take data for a longer time, and it is expected that the full exposure of the LZ experiment is 1000 days.

As I mentioned in Section 3.1.1, the potential that the grids are working can be changed. Due to this, the electric field created between these grids will also change its magnitude. Instead of the values mentioned in that section, during the SR1, the anode, the gate and the cathode grids operated at +4 KV, -4 KV, and -32 KV, respectively. Therefore, due to these potential differences, it was established a drift field of 193 V/cm between the gate and the cathode grids. Between the anode and gate grids, the extraction field in the gas phase had a magnitude of 7.3 KV/cm.

The temperature and pressure of the LXe were measured to be equal to 174.1 K and 1.791 bar.

Several calibrations occurred during the data-taking period of the SR1, however, only the deuterium-deuterium calibration, where a deuterium-deuterium neutron source was used between January 17th and January 25th, will concern us. Since neutrons enter our detector, further analysis will be needed and this will be discuss in Chapter 5.

Chapter 4

Background in the LZ experiment

This chapter will mainly discuss the background in the LZ experiment that affects our search. Therefore, before that, it is very important to describe the signal we are searching for. We will not only discuss the existing backgrounds but also how can they influence our search. For this, we will do a sensitivity study, including an estimate of the required exposure to obtain different statistical confidence levels. At first, this will be obtained using background values initially measured in the commissioning stage. Finally, two sensitivity studies varying the background levels of ^{222}Rn and ^{85}Kr individually, maintaining the remaining backgrounds constant, are also going to be considered.

4.1 Signal of the ^{124}Xe isotope

We previously discussed neutrino physics, where an important question was raised. Are neutrinos their own antiparticle? If indeed they are, they would have a Majorana nature [58]. This nature is, nowadays, a very important research topic, mainly through neutrinoless processes. These kinds of processes were discussed in Chapter 2, where we also saw their biggest problem. They are expected to have very long half-life decay times, several orders of magnitude longer than the ones in which neutrinos are emitted [59]. Due to this, their detection is challenging, so a good first step in the search for these processes is to study the two neutrino double electron capture process. It is an already seen process in some isotopes such as ^{78}Kr [100], ^{130}Ba [101], and ^{124}Xe [93]. The latter one can decay by electron capture with coincident positron emission, double beta plus decay, and double electron capture. As we will shortly see, the double electron capture with emission of two neutrinos of the ^{124}Xe isotope will be the process studied in this work.

An excellent question is, how can this process help us study the neutrino nature? Because this search must involve a neutrinoless process, however, the half-life of the neutrino emitting processes will be obtained in this study. In turn, these half-lives are related to the underlying nuclear matrix element, $M_{2\nu}$, through the following expression [92]

$$(T_{\frac{1}{2},2\nu})^{-1} = \mathrm{G}_{2\nu}^{2\mathrm{EC}} g_A^4 |m_e c^2 M_{2\nu}|^2, \tag{4.1}$$

where g_A is the axial coupling constant and $\mathrm{G}_{2\nu}^{2\mathrm{EC}}$ is the phase space factor. Relying on these nuclear matrix elements obtained through this expression, we can compare it

with the predictions of nuclear models, which will be crucial information to refine their calculations of the unknown nuclear matrix elements of neutrinoless double beta decay.

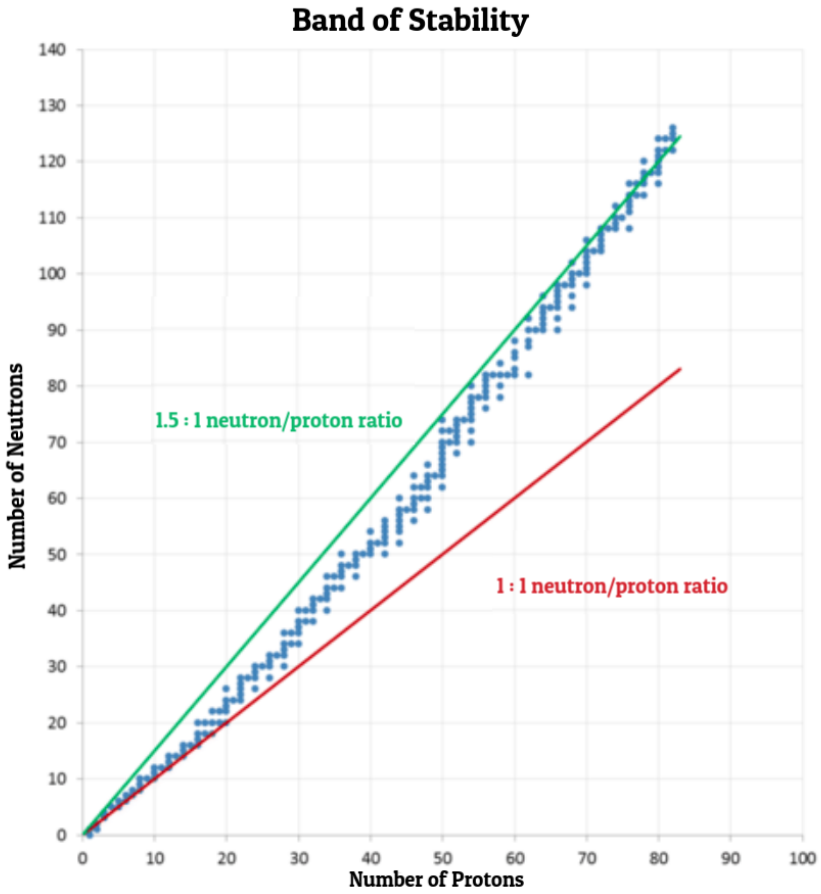

Figure 4.1: Graphical representation of the stability band as a function of the number of protons and neutrons in blue, as well as the 1.5:1 and 1:1 ratios in green and red, respectively. Figure from [102].

The double electron capture process is rather important to achieve precise calculations of nuclear matrix elements on proton-rich elements [93]. But before we explore even further that topic, it is important to understand what is a proton-rich element and especially why those nuclei are unstable. In order to achieve this, we have to look at the stability band. The stability of a nucleus depends on two main elements, the number of protons and neutrons. On the one hand, an increase in the number of protons will cause an increase in the positive charge inside of the nucleus, thus generating an increase in the repulsive force inside of this nucleus. Therefore, this will decrease the stability of the nucleus. On the other hand, an increase in the number of neutrons will increase the mass of the nucleus, making it larger and heavier, thus more unstable. However, the most important aspect is the ratio between neutrons and protons. The best value to this ratio is represented as the stability band, and it will vary with the number of protons. For nuclei with a number of protons lower than 20, the ratio is near 1, because the nucleus does not have a very strong repulsive force that can not be compensated by an equal number of neutrons [102]. However, when this number of protons is between 20 and 83, the ratio increases up to 1.5 [102]. This is due to the very large repulsive force between

the protons that can only be even by a larger number of neutrons that will be making a larger stable nucleus. This ratio increases even further when the number of protons is larger than 83 [102]. In Figure 4.1, the band of stability is depicted in blue as well as the ratio 1.5:1 and 1:1 in green and red, respectively. So, a proton-rich element will be a nucleus with a higher proton number than what was supposed in order for it to be stable. If the nucleus is proton-rich, then it will decay to decrease its number of protons. One of the possibilities is for it to decay by electron capture, where one proton combines with an electron resulting in one neutron and an electron neutrino. However as we have seen in Chapter 2, sometimes the transition (A,Z) $\rightarrow$ (A,Z-2) will happen, instead of the more common (A,Z) $\rightarrow$ (A,Z-1), due to it being more energetically favorable. One of the possibilities for this is the double electron capture process. Therefore, it is time to see the isotope we will be studying in this thesis, the ^{124}Xe isotope, which is in fact a proton-rich element [78].

This study is possible because the LZ experiment uses natural xenon as the target. In this natural xenon, one of the residual constituents is ^{124}Xe, which makes up 0.095% [92] of the total target. There are 7 tonnes of natural xenon in the active region; however, in the LZ analysis is conventional to use a fiducial volume to have a region with much lower background, of about 5.6 tonnes. Therefore, this analysis will be made with only the corresponding 5.32 kg of ^{124}Xe.

This isotope was previously considered stable, mostly due to its long half-life decay time which made its decays very hard to observe. Nowadays, we know that its main decay channel is the double electron capture [92]. This process will be also the one that we are going to search for in this analysis. However, due to its high Q-value (2856.73 keV [78]) all the other processes that reduce the number of protons discussed in Chapter 2 are also available, namely electron capture with coincident positron emission and double beta plus decay [78]. Beyond this point, these processes will be disregarded, as they are not the main focus of this work. These processes have a higher half-life decay time, so they will be harder to search for [92]. Nevertheless, as the LZ enhances its exposure, it is expected to be competitive in the search for those modes [78].

From what was discussed for this process in Chapter 2, an expression for the two neutrino double electron capture of the ^{124}Xe isotope is given by [92]:

$$^{124}\mathrm{Xe} + 2e^- \rightarrow {}^{124}\mathrm{Te} + 2\nu_e. \tag{4.2}$$

In this process, two vacancies will be created in the shells from where the electrons came from. Therefore, in the atomic de-excitation, a cascade of X-rays and possible Auger electrons are emitted as these vacancies are refilled. From the available energy (2856.73 keV), only a small part can be detected as the neutrinos, which avoid detection, carry most of that energy away. The nuclear recoil energy is near 30 eV [92], so it is also impossible to detect. The only energy that can be detected is due to the created atomic cascade and depends on which mode we are in, as we will see now.

Within this process, there are three principal different modes that can occur depending on the origin of the captured electrons. We have seen previously, that this occurs mainly from the K and L shells, so the more likely mode is when both electrons are captured from the K shell (KK) which occurs near 75% of the times, followed by the KL mode with a likelihood of 23%, and the least likely of these processes are the LL mode, which happens only in 1.7% of the times [103].

The total deposited energy for each mode equals to 64.57 keV, 36.7 keV, and 9.8 keV

for the KK, KL, and LL modes, respectively [92]. This difference is due to the binding energy of each shell because it will be the energy of the emitted particles. Despite that, not all energy can be detected because the energy deposition at the end of the cascade is too small to produce ionization or scintillation in the xenon [92], therefore it can not be detected. The only mode that was previously observed was the KK mode, from where we know that its detected energy is 64.3 keV [93], so slightly smaller than the deposited energy. For the remaining modes, it is expected that will be observed the same phenomenon. In this chapter, we are going to discuss sensitivity studies with the three different modes, however, in the following chapters, we will only analyse the KK mode due to the exposure that we already have in the LZ experiment[1].

4.2 Background overview

The LZ experiment aims to study dark matter in the form of WIMPs. This is very hard to achieve, so an extremely low background is required. Due to this, other rare processes can be studied, as is the double electron capture process we will be studying in this work. In the previous section, we saw the predicted signal for the process we are looking for, therefore it is now time to see what can prevent us from seeing it more clearly: the background.

The background will be divided into two primary sources, internal and external. The external background will be the first one discussed because it will give us insight into some of the contributions of the internal background. We will then make our way to the inside of the detector, analysing each background. Finally, simulations for these backgrounds will also be analysed. These simulations were the starting point to develop the work that we shall see in the upcoming sections.

4.2.1 External backgrounds

The first step to having a detector sensitive enough to search for such rare processes is to eliminate most of the background. Installing that detector deep underground reduces the muon flux, one of the biggest backgrounds that would make this search impossible if this was not done, by a factor of one million, in the case of LZ [84]. This provides a good reduction in the muon flux, however, the cavern rocks, that surround the detector, will also make a significant contribution to the background. The biggest source of this background comes from the emission of gamma-rays and neutrons, either by natural radioactivity or by cascades generated by the surviving muons. Despite that gamma-rays and neutrons being already inside the experiment location, their flux will be outstandingly reduced [90, 104] by using the water tank already discussed in Chapter 3.

Utilizing all of this the background in our target will be very low. However as we want to study increasingly rare processes, we have to lower its contribution even further. Sometimes this is very difficult, or even impossible, because there will always be some background. One good alternative is using multiple detectors, with reduced quantities of the target mass to serve as veto detectors. These veto detectors, such as the xenon skin

[1]The LZ experiment will be able to observe the KL mode during its 1000 days of exposure, yet in this early stage that kind of analysis is impossible.

and the outer detector, allied with the increasingly superb spatial and energy resolutions, will allow for the discrimination of the larger part of the external background.

Remains now to be discussed two significant sources of contribution to our background: the construction materials and the neutrinos, which is a contribution impossible to be reduced, however at this low background it is important and can be identified.

Starting with the construction materials, even though they passed through a very comprehensive screening program [90], there will always be contamination from radioactive elements in the constitution of these materials. Due to their proximity to the xenon, they will be a very significant contribution to the background, mainly the PMTs and the TPC which are very close to it.

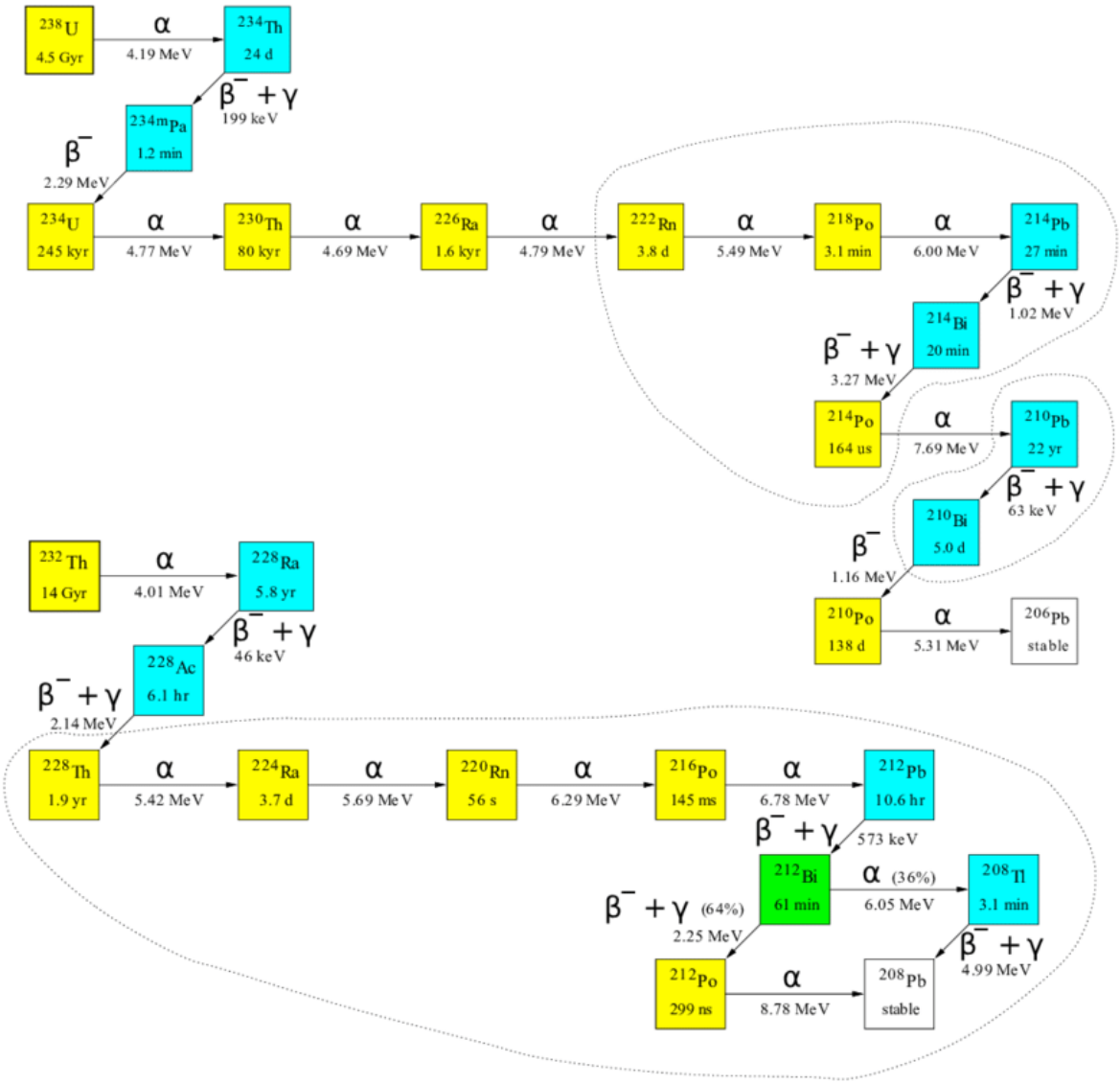

Figure 4.2: Representation of the decay chain for the ^{238}U (above) and for the ^{232}Th (below). It is illustrated their principal decay modes and their half-lives decay time. Figure from [105].

The majority of the radioactivity of these materials is due to traces of ^{238}U, ^{232}Th, ^{40}K, and ^{60}Co. Primarily, this radioactivity is originated in the ^{238}U, and ^{232}Th decay

chains, through the emission of very energetic α, β and gamma particles, as illustrated in Figure 4.2. There are two problematic transitions in these chains: the transition from the ^{214}Pb isotope into the ground state of the isotope ^{214}Bi and the decay from ^{212}Pb to the ground state of ^{212}Bi. Since it will also apply to the ^{222}Rn and ^{220}Rn[2], which are major contributors to the internal background, we shall discuss these transitions in the next subsection.

Despite their contribution, the activity from the component of the detector and from the cavern rocks is well known and understood, and was measured [106]. Therefore, it can be accounted for and introduced in the background model.

The last contribution to the external background is from the neutrinos. As the remaining particles, they can either cause NR or ER. The former is mainly caused by coherent elastic scattering of ^{8}B neutrinos [85] and the latter by neutrinos from the proton-proton chain, ^{7}Be, and CNO chain [107].

In this search, we are more interested in ER interactions, because we are searching for the double electron capture decay of the ^{124}Xe isotope through the X-rays and Auger electrons that are emitted in its decay. Thus, this constitutes only ER interactions.

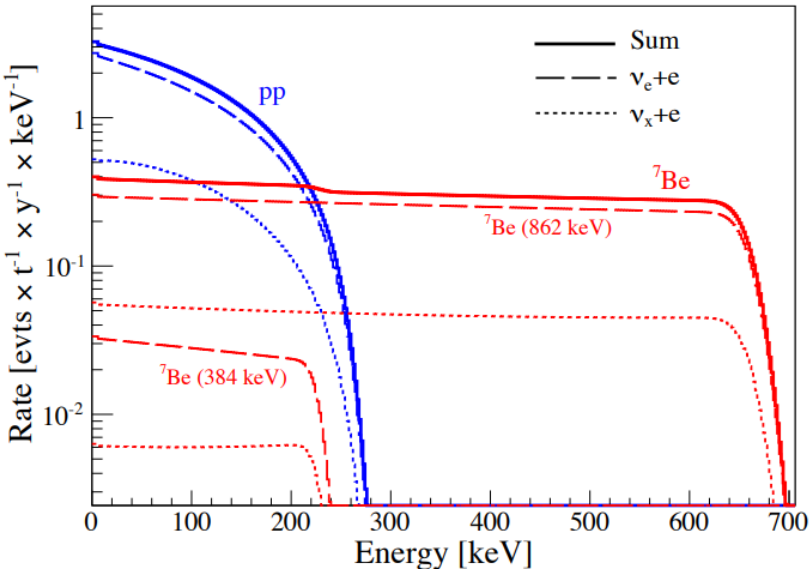

Figure 4.3: Representation of the event rate as a function of energy caused by the proton-proton chain (blue) and from ^{7}Be (red). In dashed lines the contribution of electron neutrinos are shown, whereas the other flavors are in dotted lines. The total contribution is shown in the solid lines. Figure from [108]

In Figure 4.3 it is illustrated the event rate caused by the proton-proton chain and from the ^{7}Be in the electron recoil spectra, which are the two major contributors to the ER in xenon caused by neutrinos in the lower energy region. Together they account for more than 98% of the total neutrino flux predicted by the Standard Solar Model [108]. It is also shown the contribution from electron neutrinos in the dashed lines, and from other flavors in dotted lines, whereas the solid lines represent the sum of the contribution of all flavors.

[2]As matter of fact, this will also apply because these two isotopes are part of the ^{238}U and ^{232}Th chains, respectively.

Currently, atmospheric neutrinos are the largest contributor to NR counts [87], therefore the LZ experiment is approaching the irreducible neutrino background [109]. This proves that the LZ experiment has fewer and fewer background contributions.

4.2.2 Internal backgrounds

Unlike external backgrounds that can come from several sources, internal backgrounds are very restricted and very well known. These backgrounds have three main sources, they are obviously related to the target, in this case, xenon. The first one is related to the chosen target. It was previously mentioned that the target must not be very radioactive, however, there are radioactive isotopes in the constitution of natural xenon. If this experiment did not require a very low background, this would not be relevant, however, at this level, the double beta minus decay of the ^{136}Xe isotope is a serious background. The second source comes from impurities mixed in xenon. Despite the purity of the selected xenon, it will always have some degree of impurities, and a further contributor is the radon emanated by the detector materials that we will discuss in more detail. Finally, the third source of internal background is generated by neutron activation of xenon isotopes. These neutrons can either be originated from the cavern rocks, muon showers or from calibrations, as we have seen in Chapter 3. It is now time to analyse each source individually.

The ^{136}Xe isotope, not too many years ago, was observed to decay through double beta minus decay with a half-life of 2.11×10^{21} yr [96]. If it was not for its low abundance in natural xenon, 8.857% [97], it was possible that it could preclude xenon as a target for rare decay searches. Since it would make natural xenon too much radioactive to be used as such. However, that is not the case due to its low abundance in natural xenon, and it can be used as a target. Nevertheless, this decay represents a significant background to the LZ experiment, as was measured in the SR1 with 15.3 events in the WIMP search region [110].

Regarding contributions from impurities in xenon, we have two main categories: natural impurities which have trace levels in natural xenon, and radon. We will start by discussing the first one. In natural xenon, there are trace levels of ^{85}Kr and ^{39}Ar. Both are dispersed throughout the LXe and decay through beta minus decay. These decays emit β particles, which create ER events. The ^{85}Kr isotope decays to the ground state of the ^{85}Rb isotope with 99.56% probability [107], and thus no gamma will be emitted. This type of decay is called a naked beta. This decay occurs with a half-life decay time equal to 10.76 yr [111]. The ^{39}Ar isotope decays always to the ground state of ^{39}K with a half-life decay time of 269 yr [90] and it is constrained to be less than 10% of the one of ^{85}Kr [90]. For that reason, they will constitute an important background in this experiment. A significant xenon purification campaign was instituted, where chromatography was used to remove some inert impurities such as krypton from the xenon [90]. The $^{\text{nat}}$Kr/Xe concentration, previously to the experiment, was thought to be equal to 300 ppq g/g [107]. However, during the commissioning stage, a value of 123 ppq g/g was measured for this concentration. The first value was used by Susana in her analyses, whereas the latter one was used in this work. Even more, the abundance of ^{85}Kr in natural krypton is equal to 2×10^{-11} [112]. The expected concentration of $^{\text{nat}}$Ar/Xe is 0.45 ppb g/g [87]. Furthermore, the abundance of ^{39}Ar in natural argon is equal to 8.1×10^{-16} [112].

The second category of impurities in the xenon originates from the radon emanation.

Extensive care with the detector materials was required to reduce the contribution from the radon content from the beginning of construction. In this process, residual dust, which contains radon and consequently its daughter nuclei, on surfaces in direct contact with liquid or gaseous xenon will escape and mix in the xenon, however, this contribution is much smaller than the one coming from the detector materials [84]. Moreover, the exposure of these materials to air, where radon is present, during manufacture and assembly will result in plate-out of ^{210}Pb, which leads to an additional NR background due to (α, n) reactions [84].

Due to the construction materials and the cavern rocks, small traces of ^{238}U and ^{232}Th will be present in the detector. From these two decay chains, there will be formed the isotopes ^{222}Rn and ^{220}Rn, respectively, as illustrated in Figure 4.2. Because they are gases, they can diffuse from the materials and mix with the xenon. Through that figure, we can also see that its half-life time is equal to 3.8 days and 56 seconds, respectively. As we have two isotopes that decay very quickly, and they are constantly being formed in two decay chains by isotopes with a long half-life time[3], therefore the level of radon is going to be almost constant throughout the experiment.

As these radon isotopes are a part of the decay chains of ^{238}U and ^{232}Th, it is now time to address the two problematic transitions mentioned in the previous subsection. The first one is the beta decay of the ^{214}Pb into the ground state of the isotope ^{214}Bi, therefore no gamma is emitted. This decay occurs 9.2% of the times and has a 1019 keV endpoint [113]. Without the emission of the gamma, it is very hard to detect it using the single hit approach, and it will pass the criteria cut. The second one happens in the decay from ^{212}Pb to the ground state of ^{212}Bi, which happens 13.3% of the times and has a 569.9 keV endpoint [114]. Due to this, no gamma is emitted as in the previous case. There is also another possible dangerous decay, from the isotope ^{214}Bi to the ground state ^{214}Po, with a branching ratio of 19.67% [115]. However, the daughter nucleus will decay by alpha decay with a half-life decay time equal to 164 μs, as illustrated in Figure 4.2. For that reason, this will be very easy to exclude, thus removing it from the major contributors to the background. So, the ^{222}Rn and ^{220}Rn isotopes are one of the threatening sources of background, because they are very hard to get rid of. Previously to the experiment, the activity of these isotopes was expected to be equal to 1.8 μBq/kg and 0.09 μBq/kg [87]. So, that was the value used by Susana in her analysis. However, during the commissioning part of the experiment, the activity was measured to be 5.3 μBq/kg and 0.27 μBq/kg for the isotopes ^{222}Rn and ^{220}Rn, respectively. Therefore, that was the value used in this work for the initial simulations. However, we were mistaken in one aspect, the ^{222}Rn decay chain was not in equilibrium. These values that I mentioned were measured in the beginning of the chain, thus correspond to the activity for the ^{222}Rn isotope. However, during this decay chain, isotopes between ^{222}Rn and ^{214}Pb can be removed by the getter or plate-out to the grids or walls. Therefore the activity for the ^{214}Pb isotope is significantly lower and was measured to be equal to 3.2 μBq/kg. As we saw previously, this is the concerning isotope for the background, so this value is going to be used in the final sensitivities studies.

There is only one source left to speak of, neutron activation. Almost all natural isotopes of xenon are stable or have a very long half-life. They can, however, interact with neutrons originating from the cavern rocks and calibrations, thus forming unstable

[3]In Figure 4.2, there is also the half-life for the ^{238}U and ^{232}Th isotopes, which is equal to 4.5 Gyr and 14 Gyr, thus a very large decay time.

isotopes. Their consequent decay will contribute to the background of the experiment.

We have to consider now two different regions. In the main region of detection, due to the great depth and to the water tank, the neutron flux will be very reduced, therefore almost no activation occurs inside of the TPC during normal data acquisition. The second region is the Xenon Tower, localized outside of the water tank, which is a part of the circulation system, and will be exposed to a greater neutron flux. However, this will not be very relevant because of the insignificant Xenon mass present there. Although in normal conditions there will be almost no activation from the stable isotopes, since xenon comes from the surface its isotopes will be activated due to the cosmic rays. Therefore, in the initial part of the experiment, we will have an excess of activated isotopes that will decay throughout the experiment, mainly the ^{127}Xe isotope.

The major contributor to neutron activation comes from calibrations, as we discussed in Chapter 3. Calibrations that use neutrons will greatly enhance the neutron flux in the TPC. Due to this, several unstable isotopes are produced. Among them, we have the production of ^{125}Xe, ^{131m}Xe, and ^{133}Xe with a half-life decay time of 16.9 hours, 11.9 days, and 5.3 days, respectively [90].

In Figure 4.4 it is illustrated the S2$_b$ vs S1 signals, from which we can see the events of each population of these isotopes mentioned before. The different populations are ^{127}Xe, ^{125}I, ^{133}Xe, and ^{131m}Xe as we are increasing the event density in Figure 4.4. On the left image, we have the events before a calibration took place, and on the right, it is the events after this calibration where we can see a significant increase in it.

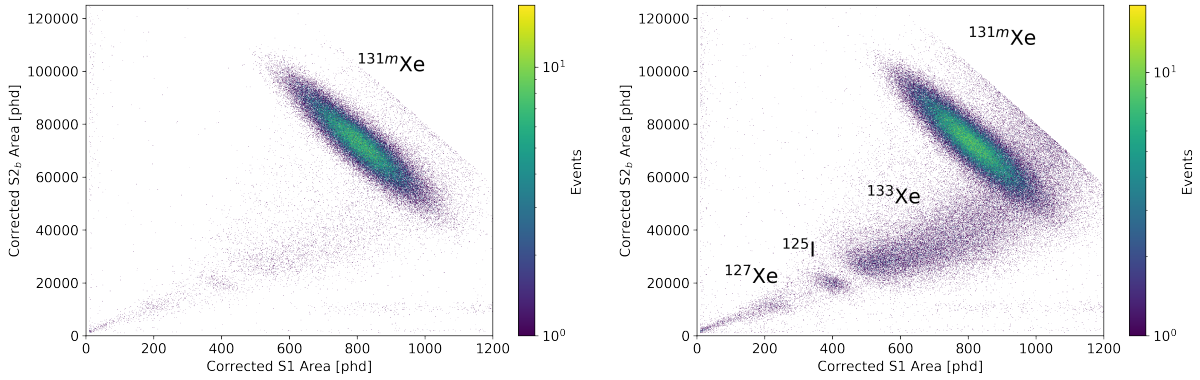

(a) Before calibration

(b) After calibration

Figure 4.4: Graphical representation of the S2$_b$ vs S1 signals before (left) and after (right) a calibration using a deuterium-deuterium neutron source: the color scale represents the correspondent event density. Populations of activated isotopes are visible after the neutrons calibration, as indicated in the figure. ^{131m}Xe is injected regularly as a calibration source, and is thus visible in both periods.

Despite this, they all have reasonably short half-life decay time, therefore will decay very quickly. However, the isotope ^{125}Xe will decay into ^{125}I, which will be the most relevant background to our search. This isotope and its removal will be the subject of the next chapter.

4.2.3 Background simulations

With that theoretical overview of the main sources of background in our mind, it is now time to address a more practical component of this work. In the remaining of this chapter, we will see the simulations that were made by the collaboration and then analysed for the double electron capture case by a colleague, and that will be our starting point to do the sensitive studies that will be discussed in Chapter 4.4. These analyses were made within the scope of her dissertation [116], so the background model that I will be using for the rest of this chapter is entirely from her.

In order to simulate the detector previous to its start, Monte Carlo simulations are usually the best course of action, and it was used in LZ. In the first step of these simulations, LZ resorts to BACCARAT. This package is able to track particles using GEANT4 [117] and will also identify their interactions inside of the detector, thus giving us a perfect understanding of what will happen inside of the detector. Moreover, it allows one to insert each material used in the construction of the detector and see the result before the detector is constructed.

We can take two different routes to use the information acquired in the first step through BACCARAT, as illustrated in Figure 4.5. In these simulations the first chain was the one used, therefore the second will be disregarded in this thesis. The energy depositions inside of the detector, previously obtained, are going to allow us to obtain the S1 and S2 signals using the NEST package [118].

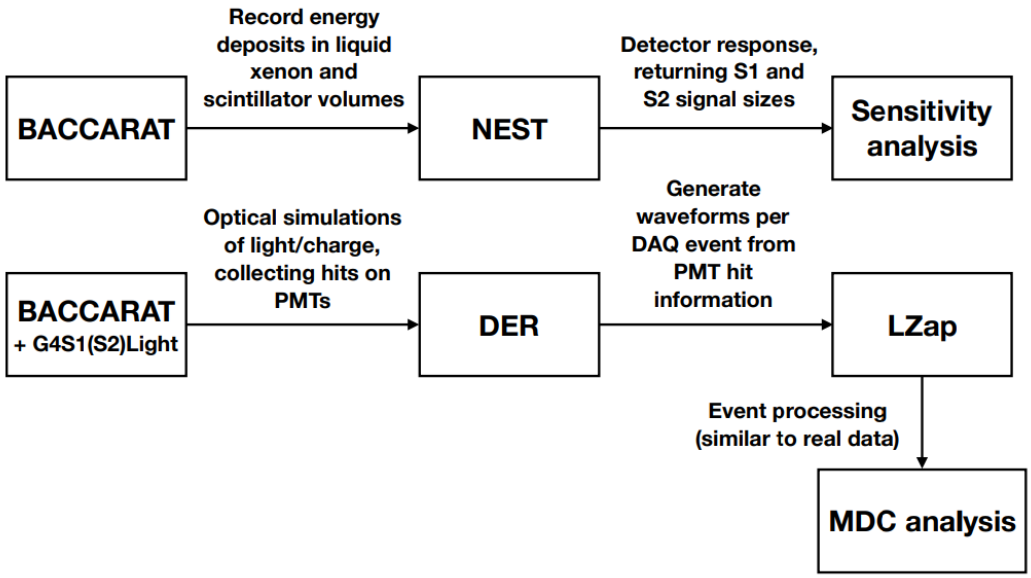

Figure 4.5: Different processing chains for the simulation used to generate data for the sensitivity analyses and Mock Data Challenges analysis. Figure from [84].

The formalism of the NEST package consists of a semi-empirical collection of models, therefore it is based not only on data from experiments, namely calibrations and science data sets but also on theoretical models. It is mainly used to study the response of noble gases, namely liquid or gaseous xenon and argon. This is done by simulating the excitation, ionization, and electron electroluminescence processes in these noble gases, as a function of particle, and interaction type, energy and electric field, among other

parameters. The S1 and S2 signals were modulated using expected light and charge yields [119].

After we understand the simulation's mechanism, it is time to address its results. First, however, we need to apply cuts to optimise these results. These cuts are applied in every search and are very helpful in removing some of the backgrounds, yet conserving most of the data.

The first cut applied is the definition of a region of interest. This will be defined as the region between 0 and 200 keV. This cut also includes the guarantee that the S1 signal has at least three PMTs that observed at least a single photoelectron (to minimize coincidences from dark counts), therefore it is a valid event [85]. The uncorrected S2 signal must be larger than 415 phd, equivalent to 5 extracted from the liquid surface [85]. This removes very small events for which the position reconstruction would not be reliable.

The events that survived this first cut are represented as the rate of the simulated background in Figure 4.6. The sum of all considered backgrounds is illustrated by the black line. The background originating from each individual source is also represented, including the detector components, ^{222}Rn, ^{220}Rn, ^{85}Kr, the double beta decay minus of ^{136}Xe, and the solar neutrinos in the pink, darker blue, green, lighter blue, orange, and yellow lines, respectively.

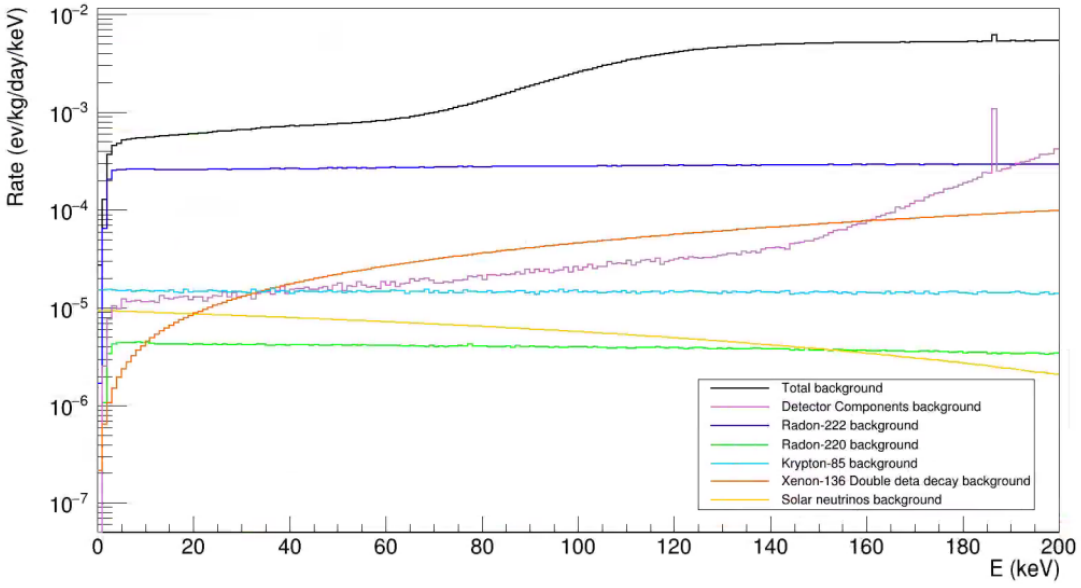

Figure 4.6: Background rate for the individual components and total background with only the region of interest cut applied. Figure from [116].

The next two cuts are applied to remove multiple scattering events, however, they are fundamentally distinct. The first one requires that the energy deposits have a small spatial extent. That means the energy-weighted standard deviation, in the radial and z direction, of any separate NEST clusters must be less than the expected spatial resolution of the detector at low energies. They are defined by Equations 4.3 and 4.4 [120] and are required to be less than 3 cm and 0.2 cm [85], respectively.

$$\sigma_r^2 = \frac{\sum_i E_i(r_i - \langle r_E \rangle)^2 \times \sum_i E_i}{(\sum_i E_i)^2 - \sum_i (E_i)^2} < 3 \text{ cm}, \tag{4.3}$$

$$\sigma_z^2 = \frac{\sum_i E_i(z_i - \langle z_E \rangle)^2 \times \sum_i E_i}{(\sum_i E_i)^2 - \sum_i (E_i)^2} < 0.2 \text{ cm}. \tag{4.4}$$

The second cut makes use of the veto detectors previously introduced. This coincident interaction in the TPC and either in one or in all detectors (OD and Skin) are excluded. For this cut, events in the LXe within an 800 μs coincidence window with energy depositions greater than 100 keV in the Skin and within a 500 μs coincidence window with energy depositions greater than 200 keV in the OD are excluded [84]. The background coming from neutrino interactions and from the double beta minus decay of ^{136}Xe produce single scatters, and thus they will not be affected by these two cuts.

In Figure 4.7, it is illustrated the background that survived the single scatter and veto cuts as a function of radial and z positions inside the xenon. As we discussed previously, it is shown that due to the excellent shielding properties of xenon there is an internal region far from the internal surfaces of the TPC where the background is much lower. It is also relevant to mention that there is more background at the top of the active region than at the bottom due to the xenon present in the reverse field region, which shields the bottom region from the external background (mainly from the PMTs).

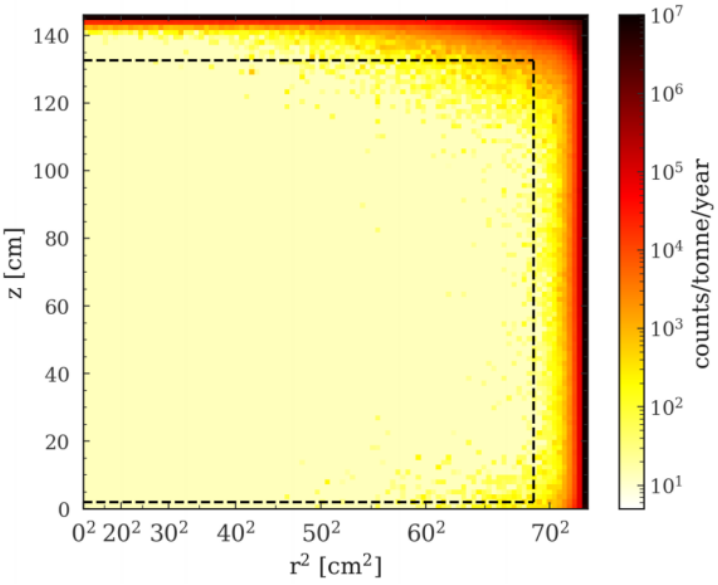

Figure 4.7: Spatial distribution of all ER backgrounds that get through both the single scatter and veto cuts, with energy less than 100 keV. The dashed black line identifies the fiducial region. Figure from [85].

For that reason, the final cut will be the fiducial one, where we choose an inside region with less target mass, although with much less background. This will allow a better search for rare events, such as dark matter and rare decays. This fiducial volume is defined as the events occurring within a cylinder with a radius less than 68.8 cm and a vertical coordinate between 1.5 cm and 132.1 cm, thus making a total target mass of 5.6 tonnes of LXe [85].

Finally, in Figure 4.8, the final background model is illustrated, after all cuts, from the same background sources and represented by the same line colors. Again, there is a clear decrease in the total background rate, where the background from the double beta minus decay of ^{136}Xe and from the ^{222}Rn isotope are dominating. Comparing this rate with the one obtained before the cuts, it is clear that the background coming from the detector component was very reduced using these cuts, and it is now almost negligible.

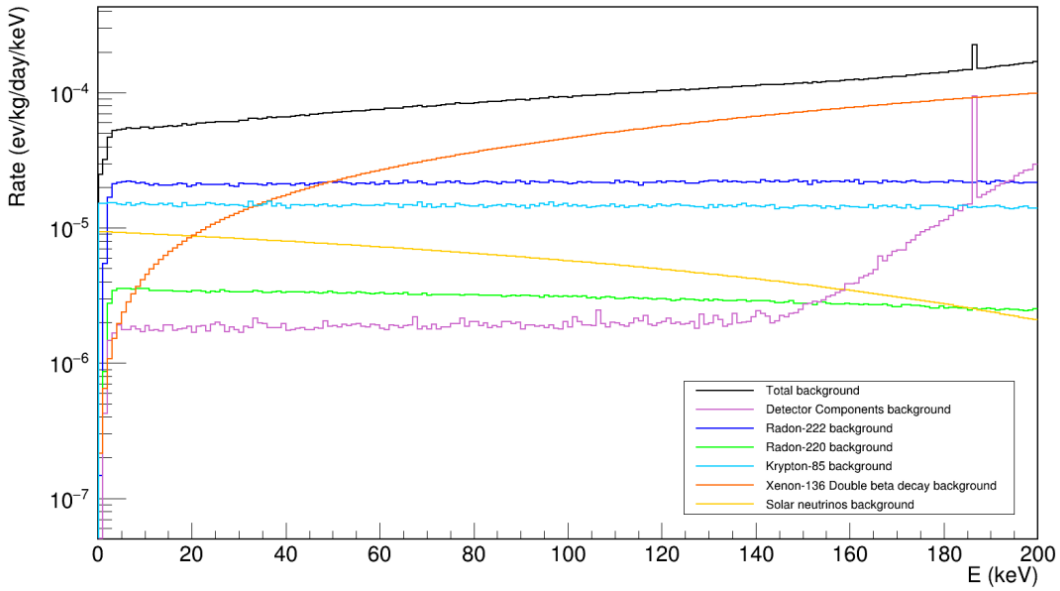

Figure 4.8: Background rate for the individual components and total background after all cuts applied. Figure from [116].

4.3 The Rolke Method

The frequentist statistical approach of Rolke [121] was used to obtain the different potentials in the sensitivity study made for the three modes of the double electron capture of ^{124}Xe within the LZ experiment. More specifically, we use TRolke, which is a C++ implementation of this Rolke method [121]. It allows us to estimate the upper limit of certain signal events, considering uncertainties in the background model and in the signal efficiency [122]. The method allows several different approaches for both the parameters, including no uncertainties, binomial, gaussian, and poissonian distributions for the uncertainties [122].

The background events obtained were considerably large, therefore it was assumed a gaussian approach in the analysis that follows. For that reason, the uncertainty is going to be equal to the square root of the number of events. We have not yet seen how can this upper number of events apply to our study. The half-life of the decay we are searching for is given by [92]:

$$T_{1/2}^{2\nu 2EC} = \frac{\ln(2) a N_a}{A} \frac{M \Delta T}{\mu}, \tag{4.5}$$

where a is the natural abundance of the ^{124}Xe isotope in natural xenon, which is equal to 0.095%, N_a is the Avogadro number, A is the isotope molar mass, which is 123.9 g/mol

[123], M is the fiducial mass, that is 5600 kg and ΔT is the exposure time that will vary and can not be larger than the total exposure time predicted for the experiment which is 1000 days. One parameter remains to be explained and it is the most important one, the μ parameter, which is the only one coming from the use of the Rolke method. To use this method, we will introduce the number of background events obtained for a specific region, and it will estimate the upper limit on the number of signal events that would still be compatible with that background for the confidence level of our choice. We choose to use the 90% confidence level. Besides that, it can also be used to estimate the numbers of events that we need in order to claim an observation or discovery, which are normally claimed when we have a statistical significance of 3σ and 5σ, respectively. The value obtained using the Rolke method, thus corresponds to this μ parameter and can be introduced in Equation 4.5.

One key aspect of TRolke is the lack of uncertainty for the estimate of the number of signal events. In the interest of obtaining said uncertainty, 1000 samples of the background model were used. The expected background obtained in the region that we were searching was the mean value for this distribution, and its standard deviation was the square root of this number of background events. This was done for each one of the three decay modes and for several different exposure time values. The crucial difference between the previous method and this one is that instead of the TRolke being applied only to this mean value[4], it was applied to the 1000 points created from this gaussian distribution. Through this, it was possible to obtain not only the required number of events to reach the 90% confidence level sensitivity (or to claim an observation or a discovery), but also an uncertainty in this number of events. From that, after these numbers were passed through TRolke we would obtain another Gaussian distribution, where its mean value and standard deviation were the required number of signal events that we pretended and its uncertainty, respectively.

After we have the half-life decay time, it can be compared to the experimental values measured to obtain the required time that would take for the LZ experiment to claim the 90% confidence level sensitivity, and the observation and discovery potentials. If for the KK mode we have the measured value, 1.8×10^{22} yr [93], the other modes were not yet observed, therefore we do not know its experimental values. However, the half-life of the other modes, $T_{1/2}^{2\nu x}$, can be obtained starting from the double electron capture, $T_{1/2}^{2\nu 2EC}$, and divided by the likelihood of that decay mode, f_x, and this is given by:

$$T_{1/2}^{2\nu x} = \frac{T_{1/2}^{2\nu 2EC}}{f_x}. \tag{4.6}$$

Starting with the value for the KK mode and multiplying it by 0.75, corresponding to its branching ratio [103], we obtain the half-life of the double electron capture, a value of 1.4×10^{22} yr. Dividing this value by 0.23 and 0.017, respectively, the corresponding branching ratios of the KL and LL modes [103], we obtain the half-life values for each of these modes, which are equal to 6.1×10^{22} yr and 8.2×10^{23} yr, respectively.

[4]Where this mean value, as was said previously, is the number of background events obtained for that specific region.

4.4 Sensitivity studies

In this section, we will be using the half-life decay time for the three modes of the double electron capture, obtained through the Rolke method, in order to obtain the required time for the LZ experiment to reach the 90% confidence level sensitivity, and to claim an observation or a discovery. Since the Xenon1T experiment is very similar to the LZ experiment, therefore throughout this section it was chosen an energy resolution that follows the energy resolution curve obtained for that experiment [124]. For that reason, the energy resolution used is equal to 4.1%, 5.3%, and 10.2%, for the KK, KL, and LL modes, respectively [116].

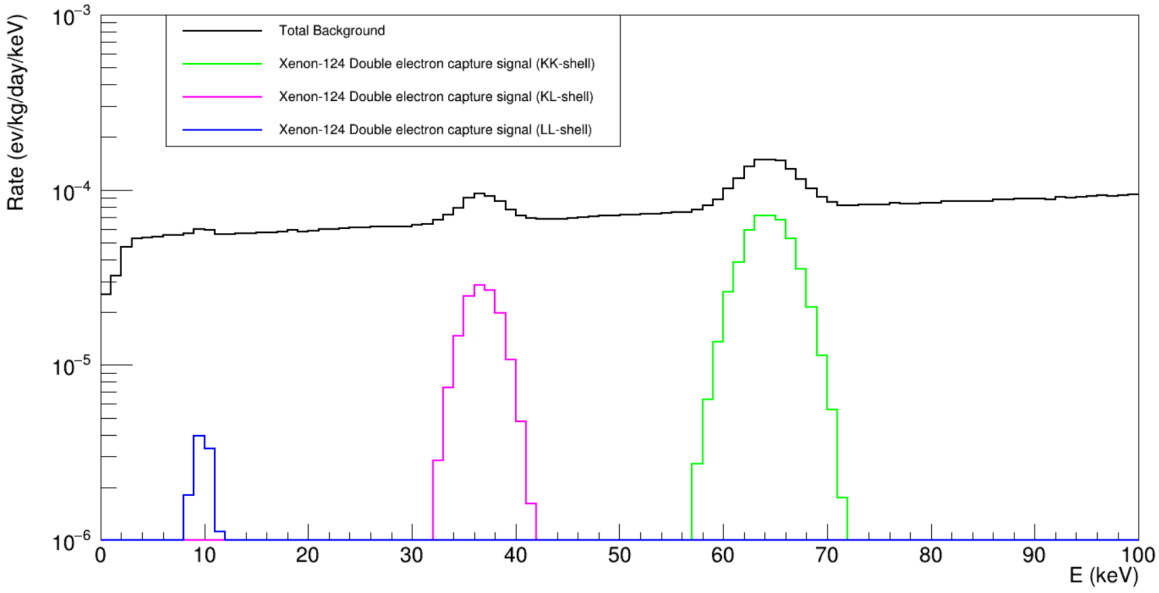

Figure 4.9: The expected rate for the observed signal plus the background sources for the double electron capture of the ^{124}Xe isotope is represented as the black line. In blue, pink, and green it is depicted the expected individual signal for the LL, KL, and KK modes, respectively. It was used the same values as in the previous graph, 1.8 μBq/kg and 0.09 μBq/kg for the activities of ^{222}Rn, and ^{220}Rn, respectively, and 300 ppq g/g for the ^{nat}Kr/Xe concentration.

We will consider a $\pm 2\sigma$ window around the expected signal energy, which is equal to 64.3 keV, 36.7 keV, and 9.8 keV, for the KK, KL, and LL modes, respectively, as our region of interest. This window will correspond to an efficiency of 95.4%. Using the energy resolutions and the expected signal energies for each of the three modes, we obtain our region of interest for these modes, which are equal to [59.03, 69.57] keV, [32.81, 40.59] keV, and [7.80, 11.80] keV for the KK, KL and LL modes, respectively.

To obtain the expected signals for each decay mode, we can do a gaussian distribution where its mean value and standard deviation are equal to the expected energy of that decay mode and its energy resolution, respectively. If we add these signals to the sum of all the background components after all the cuts, represented by a black line in Figure 4.8, we obtain the expected signal observed in the experiment. This is represented by the black line in Figure 4.9. The KK, KL, and LL modes signals are represented in green, pink, and blue, respectively. I did not prolong myself on the topic of scaling in Figures

4.6 and 4.8, however, if we sum the individual components of the background we have to normalize them. This is required because it was simulated a certain number of decays, x, during the simulation stage. However, that isotope will have a number of annual decays, y, therefore our normalization constant will be equal to $\frac{y}{x}$. Nevertheless, it is important to know that to obtain Figure 4.9, each signal was scaled assuming the half-lives, previously mentioned, that are equal to 1.8×10^{22} yr, 6.1×10^{22} yr, and 8.2×10^{23} yr, for the KK, KL and LL modes, respectively.

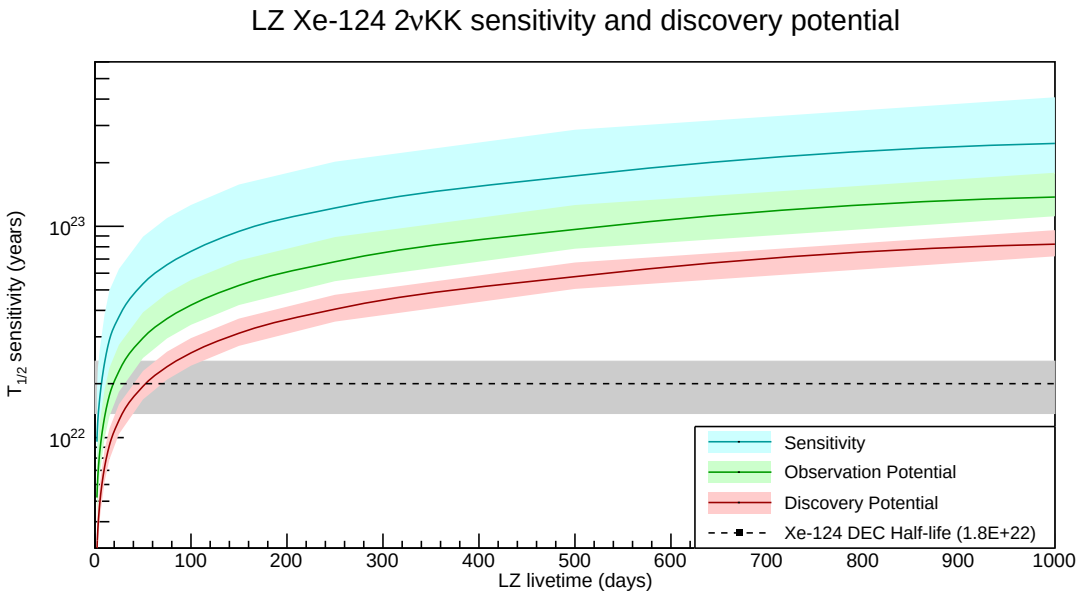

Figure 4.10: Time evolution for the 90% confidence level sensitivity, the observation potential, a statistical significance of 3σ, and discovery potential, a statistical significance of 5σ, for the 1000 days of exposure in the LZ experiment in the KK decay mode represented by the blue, green, and red lines. The bands, which have the same color as their lines, illustrate the uncertainty band at 68% of confidence level, that means a uncertainty of $\pm\sigma$. The dashed black line represents the half-life, measured by Xenon1T, for the KK mode. Its uncertainty is also depicted by the gray area.

Using the method explained in Chapter 4.3, we have now every tool to obtain the required time for the LZ experiment to reach the 90% confidence level sensitivity, and to claim an observation or a discovery. For this study, we used constant values for the background, where the activity for the ^{222}Rn isotope was equal to 5.3 μBq/kg and for the isotope ^{85}Kr was equal to 123 ppq g/g. In the first study, we will maintain these values constant throughout that, however, later we will vary them individually.

Starting with the KK mode, in this decay, there are 64.3 keV of detectable deposits of energy. As we intend to study this signal with an efficiency of 95.4% (2σ), our region of interest will be defined as [59.03, 69.57] keV. In this region we are going to obtain the number of background events that will later, through the Rolke method, give us the upper limit to the number of signal events that would still be compatible with that background.

Figure 4.10 illustrates the expected evolution not only for the 90% confidence level sensitivity, in blue, but also for the observation (3σ) and discovery (5σ) potentials, in green and red respectively, for the KK mode during the 1000 days of exposure in the

fiducial mass. Comparing this with the half-life measured by Xenon1T, represented in the black dotted line, we can find out the required days to obtain such statistical significance. Thus, the LZ experiment is expected to be able to claim an observation, a statistical significance of 3σ, after 20^{+11}_{-9} days of exposure, and a discovery, a statistical significance of 5σ, after 54^{+17}_{-14} days of exposure.

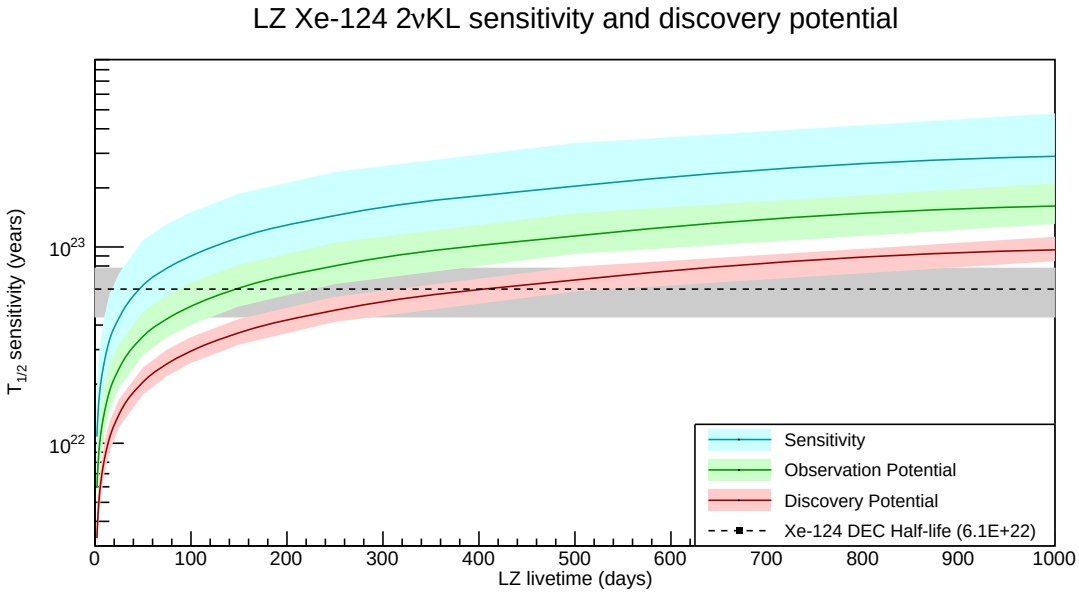

Figure 4.11: Time evolution for the 90% confidence level sensitivity, the observation potential, a statistical significance of 3σ, and discovery potential, a statistical significance of 5σ, for the 1000 days of exposure in the LZ experiment in the KL decay mode represented by the blue, green, and red lines. The bands, which have the same color as their lines, illustrate the uncertainty band at 68% of confidence level, that means a uncertainty of $\pm\sigma$. The dashed black line represents the expected half-life for the KL mode, obtained through the method described in the main text. Its uncertainty is also depicted by the gray area.

As for the KL mode, the expected energy signal is equal to 36.7 keV, thus our region of interest will be given by [32.81, 40.59] keV. In Figure 4.11, it is again illustrated the expected evolution for the 90% confidence level sensitivity, in blue, and for the observation and discovery potentials, in green and red respectively, but this time for the KL mode during the 1000 days of exposure in the fiducial mass. The LZ experiment is expected to be able to claim an observation after 147^{+79}_{-61} days of exposure and a discovery after 416^{+118}_{-110} days of exposure, for the KL decay mode. This will surpass the KK mode of the double electron capture of the ^{124}Xe isotope as the longest directly observed decay.

Finally, for the LL mode, the expected energy signal is equal to 9.8 keV, therefore our region of interest will be defined as [7.80, 11.80] keV. As can be seen in Figure 4.12, during the 1000 days of exposure, the LZ experiment will not be able to claim an observation, much less a discovery.

Besides this study with constant activities from the background contributions, two distinct others were made. In the first one, the background level of the ^{222}Rn isotope was varied, keeping the other contributions constant. The second one is a similar study, where instead of the ^{222}Rn isotope, we varied the background from ^{85}Kr isotope.

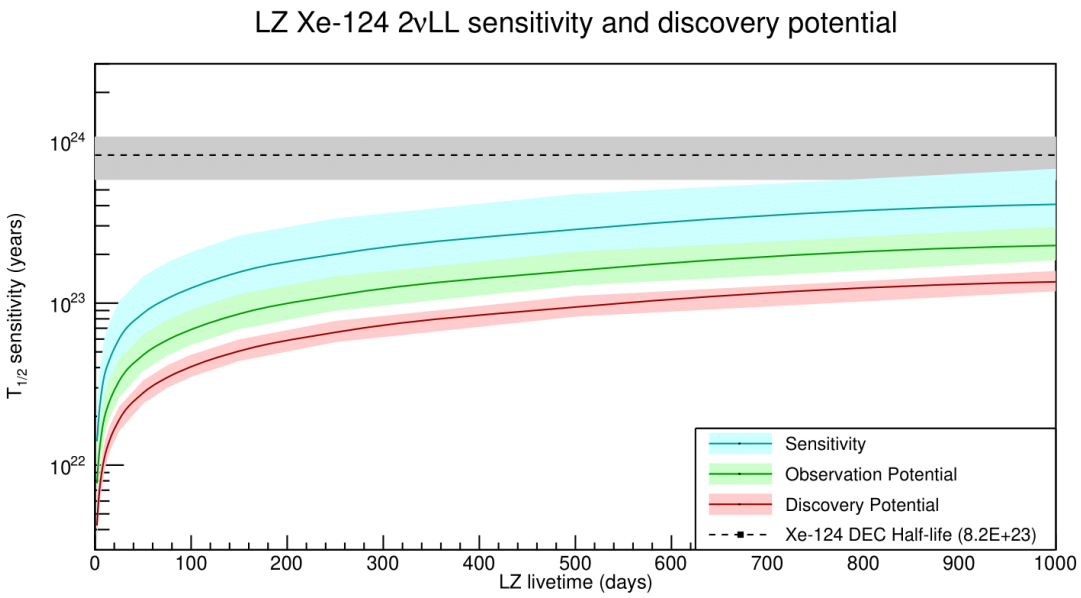

Figure 4.12: Time evolution for the 90% confidence level sensitivity, the observation potential, a statistical significance of 3σ, and discovery potential, a statistical significance of 5σ, for the 1000 days of exposure in the LZ experiment in the LL decay mode represented by the blue, green, and red lines. The bands, which have the same color as its lines, illustrate the uncertainty band at 68% of confidence level, that means a uncertainty of $\pm\sigma$. The dashed black line represents the expected half-life for the LL mode, obtained through the method described in the main text. Its uncertainty is also depicted by the gray area.

In the first one, the different values presented in Table 4.1 were used for the background of the ^{222}Rn isotope, whereas the remaining backgrounds were kept constant. This analysis followed the same approach as the previous ones, where using the Rolke method we estimate the upper limit on the number of signal events that would still be compatible with the background present in a specific region of interest, for the confidence level of our choice. After that, we would compute the half-life decay time and its variance with the different backgrounds for several exposure times. From these values, it was possible to infer the required time to reach the different claims using the value for the half-life time of the KK mode by Xenon1T. In this specific analysis, we were only interested in the discovery potential of the KK mode, and in the observation and discovery potentials in the KL mode. The remaining potentials for the different modes were either impossible in the LZ experiment, as is the case of the LL mode, or not interesting at this stage, as is the case of the 90% confidence level and the observation potential for the KK modes. In this study, the background of the ^{85}Kr isotope was considered as 123 ppq.

In Figure 4.13 it is illustrated the exposure time required for the LZ experiment to reach the discovery potentials for the KK mode, in blue, and the observation and discovery potentials for the KL modes, in green and red, respectively, as a function of the activity of the ^{222}Rn isotope. The vertical dashed black line shows the best estimate, 3.2 μBq/kg, for the activity of the ^{222}Rn isotope during the SR1 of the LZ experiment.

Comparing the required time to claim these different potentials as a function of the activity of the ^{222}Rn isotope and the best estimate during the SR1 of the LZ experiment,

Table 4.1: Different background used for the ^{222}Rn isotope in order to obtain the required exposure time to claim different potentials as a function of its background.

^{222}Rn background (μBq/Kg)
0.1
0.3
0.6
0.9
2
5
8
10

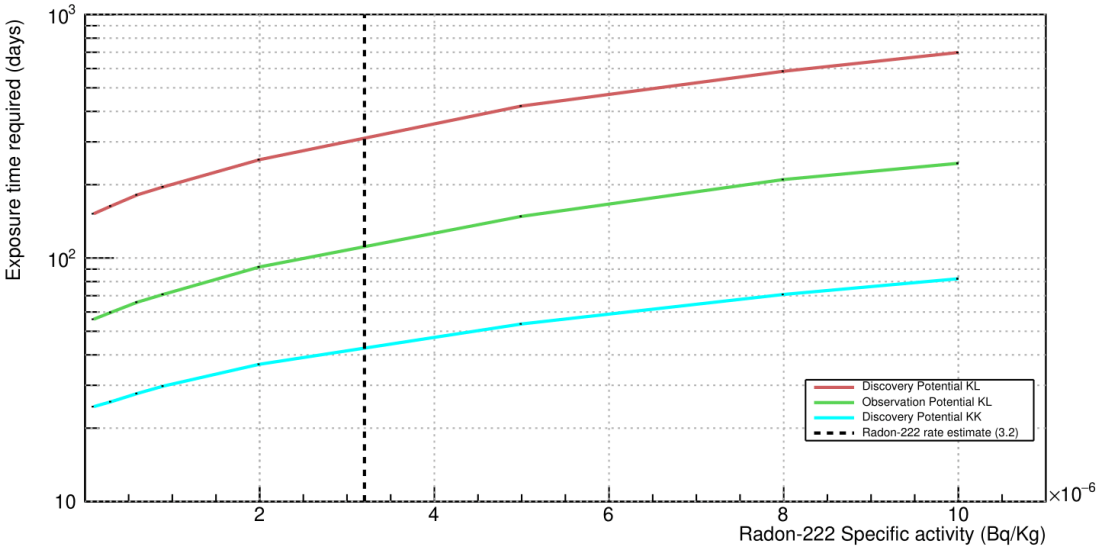

Figure 4.13: Exposure time required for the LZ experiment to reach the discovery potentials for the KK mode, in blue, and the observation and discovery potentials for the KL modes, in green and red, respectively, as a function of the activity of the ^{222}Rn isotope. In the vertical dashed black line it is shown the best estimate, 3.2μBq/kg, for the activity of the ^{222}Rn isotope during the SR1 of the LZ experiment.

we can make a good prediction for the required time to claim such potentials using those values of background. Making that comparison, we obtain that if the background for that isotope maintains the value of the best estimate throughout the experiment, LZ will be able to claim a discovery in the KK mode after 44 days of exposure, whereas it could claim an observation and a discovery in the KL mode after 115 and 321 days, respectively. Furthermore, these values can be compared to the ones obtained in the last study, where now, since the background from the ^{222}Rn isotope is considered lower, the

required time to reach the potentials will be smaller.

In the second study, the different backgrounds for the ^{85}Kr isotope used are displayed in Table 4.2. This was rather similar to the previous one, where it was used the same procedure explained for the case of the ^{222}Rn isotope. Instead of using the value obtained during the commissioning stage, 5.3 μBq/kg, as the background for the ^{222}Rn isotope, it was used firstly the expected value before the beginning of the experiment, 1.8 μBq/kg, and secondly the best estimate for the SR1 of the LZ experiment that we already had. That value, as we have previously seen is equal to 3.2 μBq/kg.

Table 4.2: Different contamination levels used for the ^{85}Kr isotope in order to obtain the required exposure time to claim different potentials as a function of its background.

^{85}Kr background (ppq)
10
100
150
200
250
500

Figure 4.14 compares the required exposure time for the LZ experiment to reach not only the discovery potentials for the KK mode, in blue, but also the observation and discovery potentials for the KL modes, in green and red, respectively, as a function of the activity of the ^{85}Kr isotope for the two activities used for the ^{222}Rn isotope. In the full lines we have the result from using 3.2 μBq/kg, while the dashed lines represent the result obtained by using 1.8 μBq/kg for the activity of the ^{222}Rn isotope. It is also shown the best estimate for the activity of the ^{85}Kr isotope during the SR1 of the LZ experiment in the vertical dashed black line, which is equal to 144 ppq g/g.

Comparing now the required time to claim these different potentials as a function of the activity of the ^{85}Kr isotope and the best estimate during the SR1 of the LZ experiment. Assuming these backgrounds as the ones during all the experiment, we obtain that LZ will be able to claim a discovery after 36 days of exposure for the KK mode, while are required 90 and 246 days to claim an observation and a discovery for the KL mode, respectively, using 1.8 μBq/kg for the activity of the ^{222}Rn isotope. In the other case, where the activity of the ^{222}Rn isotope is 3.2 μBq/kg, the LZ will be able to claim a discovery after 44 days of exposure for the KK mode, while 117 and 329 days are required to claim an observation and a discovery for the KL mode, respectively.

Unfortunately, the background was rather elevated in the experiment comparing it with the initially expected background, as is shown in Figure 4.14. Looking at both of these studies, we can understand that it will take us now more 8, 27, and 83 days to reach the discovery potential in the KK mode, and the observation and discovery potentials for the KL mode, respectively, in comparison with the initial projections.

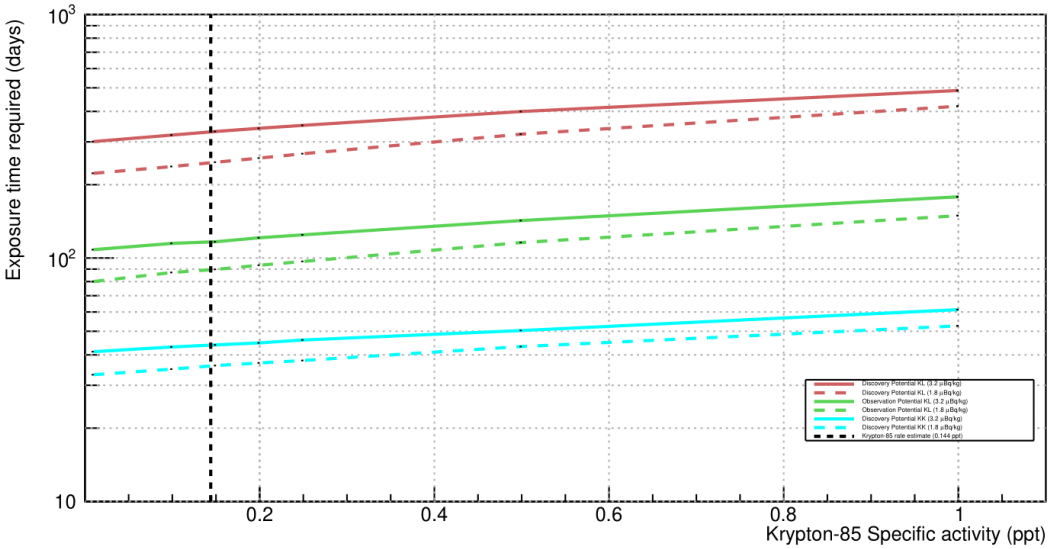

Figure 4.14: Exposure time required for the LZ experiment to reach the discovery potentials for the KK mode, in blue, and the observation and discovery potentials for the KL modes, in green and red, respectively, as a function of the activity of the ^{85}Kr isotope. The vertical dashed black line shows the best estimate, 0.144 ppt, for the activity of the ^{85}Kr isotope during the SR1 of the LZ experiment. The result from using 3.2 μBq/kg for the activity of the ^{222}Rn isotope is represented by the full lines, whereas the one obtained by using 1.8 μBq/kg for the activity of the same isotope is represented by the dashed lines.

Chapter 5

The ^{125}I isotope as a background for the 2ν2EC ^{124}Xe decay search

In this chapter, we will discuss the ^{125}I isotope and its importance in the search for the KK mode of the double electron capture of the ^{124}Xe isotope. We will be starting with an overview of the decay of the ^{125}I isotope, followed by an analysis of this isotope in the LZ experiment and its removal. Finally, this chapter will be ended by analysing the distribution of the ^{125}I isotope in the TPC of the LZ experiment to detect a possible circulation problem with the LXe during SR1.

5.1 Signal of the ^{125}I isotope

Natural xenon is constituted by several isotopes, as we have previously mentioned, which are either stable or with half-lives of several orders of magnitude larger than the age of the Universe. However, these stable isotopes can be activated by neutrons, thus becoming unstable isotopes. From the created isotopes, as we have seen in Section 4.2.2, the most dangerous one for our search is the ^{125}Xe isotope produced through the following process [92]:

$$^{124}\mathrm{Xe} + n \rightarrow {}^{125}\mathrm{Xe} + \gamma. \tag{5.1}$$

The isotope produced, ^{125}Xe, in turn, will decay through electron capture with a half-life of 16.9 hours to an excited state of the ^{125}I isotope. Due to the orbital vacancy created in the shell being filled by the external electron, and from the decay of the atom to its ground state, a cascade of X-rays and Auger electrons will be produced alongside the emission of gammas [92]:

$$^{125}\mathrm{Xe} + e^- \rightarrow {}^{125}\mathrm{I} + \nu_e + \gamma + X, \tag{5.2}$$

where X represents the cascade of X-rays and Auger electron.

Figure 5.1 represents the decay scheme of the ^{125}I isotope. As can be seen, this isotope will decay through electron capture to the 35.5 keV excited state of the ^{125}Te isotope. This decay will occur with a branching ratio of 100%, a half-life of 59.4 days, and with a decay energy of 185.77 keV. The atom will later decay to its ground state, and refill its orbital vacancies, as is normal in this type of decay, thus emitting gammas and a cascade of X-rays and Auger electrons, as we can see by Equation 5.3 [92].

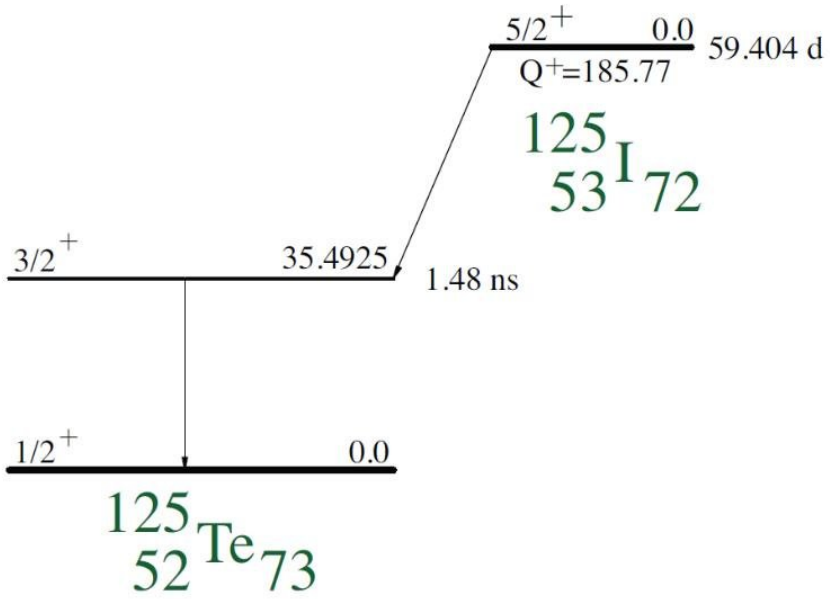

Figure 5.1: Decay scheme of the ^{125}I isotope: ^{125}I decays to the 35.5 keV excited state of the ^{125}Te isotope with a half-life of 59.4 days, which in turn will decay, almost instantly, to its ground state. Figure from [125].

$$^{125}\mathrm{I} + e^- \rightarrow {}^{125}\mathrm{Te} + \nu_e + \gamma + X. \tag{5.3}$$

When the captured electron is from the K shell, which occurs 80.11% of the times [126], the emitted particles in this decay will lead to a deposited energy of 67.3 keV [92]. If we now consider the energy resolution for this energy regime obtained in the LUX experiment, approximately 4% [92], we obtain that this energy deposition is only 1.1σ (3 keV)[1] away from the energy deposit of the double electron capture of the KK mode for the ^{124}Xe isotope, 64.3 keV.

Unlike the other unstable isotopes formed through neutron activation, the ^{125}I isotope is the only one close enough to the deposited energy for the decay we are searching for, and with a long half-life capable of affecting this search, and as such, it could be an important background to our search. In the upcoming section, we will see how is this avoided in the LZ experiment, and a study of its removal will also be analysed.

5.2 The ^{125}I isotope in the TPC

Usually, the flux of neutrons in the TPC is negligible due to the set of conditions applied in this kind of experiment, discussed in Chapter 4, to minimise it. For that reason, almost no activation of the xenon isotopes occurs. However, there is a subsystem where the flux of neutrons could be more dangerous: the Xenon Tower. It is a localized constituent of the circulation system located outside the water tank; thus, the flux of neutrons is larger. In that region, there is always xenon that can be activated and will later enter the TPC, however, the xenon mass is very small making this contribution negligible. Although typically, the flux of neutrons in the TPC is negligible, the same is

[1]Considering this energy resolution, we obtain that 1σ is equal to 2.692 keV.

not true when calibrations using neutrons occur. During these calibrations, a large flux of neutrons will be present in the TPC activating the xenon, and later the ^{125}I isotope will be formed, as we have seen in the previous section. During this section, we will be interested in the rate of the ^{125}I isotope formed during the DD calibration taken between January 17th and January 25th. This isotope should be removed by the getter, as was seen in the LUX experiment; if not it would represent a very significant background to the KK mode of the double electron capture of the ^{124}Xe isotope, both due to the proximity and to the long half-life of the ^{125}I isotope. Therefore, in this section, we will be interested, more specifically, in the removal of this isotope to define the time interval we must exclude in order to search for that decay without having such a large background.

5.2.1 Event selection

One of the first steps in a search for a specific decay is to apply cuts in the data to have the lowest possible background while conserving the most data possible. We have seen in Chapter 4 the cuts applied to the simulated data, and in this analysis, some of those cuts were also used, however, because we are dealing with real data other cuts must also be applied.

The process we are searching for only produces single scatter, since the path travelled by the X-rays and Auger electrons is very short and indistinguishable inside of the detector. Hence, multiple scatter events are excluded and we only consider single scatter events.

We have also seen that the Outer Detector and the Skin can be used as veto detectors. For that reason, a cut for both of these detectors is applied, which include prompt and delayed cuts. Starting with the Outer Detector, the prompt veto is used to catch proton recoils or gamma rays: there must be a coincidence of less than 5 PMTs, and the prompt signal must be outside of a ± 0.3 μs region of the TPC S1 pulse in order to survive this cut. The delayed cut is implemented to catch gammas from neutron captures and removes events with coincidence larger than 5, areas larger than 17.6 phd (photons detected), and with prompt signals within a region between 300 ns and 400 μs of the TPC S1 pulse. This interval is larger due to the thermalisation time of the neutron, therefore a delayed window is required.

The Skin cuts also contain prompt and delayed cuts, where the prompt veto searches for a prompt coincidence from gamma interactions or neutron NR. This cut excludes events with coincidence larger than 2, therefore 3 or more PMTs observe it, areas larger than 2.5 phd within a ± 0.5 μs region of the TPC S1 pulse. The delayed cut is used to catch remains of gammas from the Outer Detector and capture gammas that did not interact in the Outer Detector, where events with coincidence greater than 55 are excluded, and a pulse with an area larger than 50 phd within a region comprised between 500 ns and 400 μs relative to the TPC S1.

One of the most impressive features of this experiment is the reconstruction of the event properties from the two interactions that occur inside the TPC. However, sometimes this reconstruction is not done well and this event must be excluded. Therefore, a cut was applied to remove events with bad reconstructions.

Sometimes high single electron or multi-electron rates from hotspots can cause pile-up. By implementing the hotspot exclusion periods cut we are removing time periods that exhibit flare-ups of grid hotspots. Considering 120-second bins, intervals are removed if

they exceed the mean rate for all SR1 data by at least two standard deviations.

When a muon passes the TPC region, high rate periods will, most likely, follow it, therefore this cut selects high energy events in the Outer Detector that also have a timing coincidence with the skin. Pulse area cuts are applied in the TPC and Skin regions to select the muon. Finally, if an event triggers the cut, a hold-off of 20 seconds will be applied.

For these initial set of applied cuts the bad buffer cut remains to be discussed. The importance of this cut arises from the fact that the DAQ buffers can store a limited set of data post-trigger, around several μs of data. So, if a channel's buffer has no more storage for the post-trigger data, then all the following data will be lost. The event will survive this cut if all buffers are live at the start of the pre-trigger window, if the TPC buffers are live through the end of the main S2, if the skin buffers are live both through the end of the main S1 and through the end of the skin veto window, which in this case was considered to be 400 μs, and, finally, if the skin buffers are live both through the end of the main S1 and through the end of the Outer Detector veto window, which was also considered to be 400 μs.

These cuts were applied in order to identify good events and exclude the rest. The remaining cuts, unlike the other ones, are not applied to eliminate bad events but rather to remove a larger quantity of background and events which we are not interested in, to have a clear signal of the decay we intend to study.

Regarding these types of cuts, the first one is the fiducial volume cut. This cut was extensively discussed in Chapter 4, and pretends to exclude a massive quantity of background while conserving most of the xenon mass as an available target. For this study were considered the same dimensions as in the simulations, where it was considered events occurring within a cylinder with a radius less than 68.8 cm and with a vertical coordinate between 1.5 cm and 132.1 cm. Inside this region are 5.6 tonnes of LXe.

Finally, to focus our search we only considered events with energy lower than 200 keV. Because as we have seen previously our decay occurs with energies lower than 100 keV, therefore with a region of interest up to 200 keV we can do a complete study for the decay analysed in this work.

5.2.2 Population selection

After all cuts are applied, using the S1 and S2 values obtained in this experiment we can depict S2 as a function of the S1 for the period after this calibration during the SR1, as is illustrated in Figure 5.2. In this figure, several populations of the isotopes created during this calibration are located by the different densities of events. Going left to right on the x-axis, we have the ^{127}Xe, ^{125}I, ^{133}Xe, and ^{131m}Xe isotopes.

Since the populations are very accessible and easy to analyze the following steps of this analysis will be done using this parameter space, however, using Equation 3.5 we can obtain the energy reconstruction using these S1 and S2 values. Regarding that equation, a slight change was used because due to high values for S2 the top array of PMTs, where its value is quite larger, can become saturated, therefore the S2 obtained only through the bottom array was used ($S2_b$) and consequently the g2 bottom.

Using that reconstructed energy, we can obtain the energy spectrum for the events occurring after the DD calibration, which is shown in Figure 5.3. It is shown the same populations as in Figure 5.2, where in this case we can identify them either by their

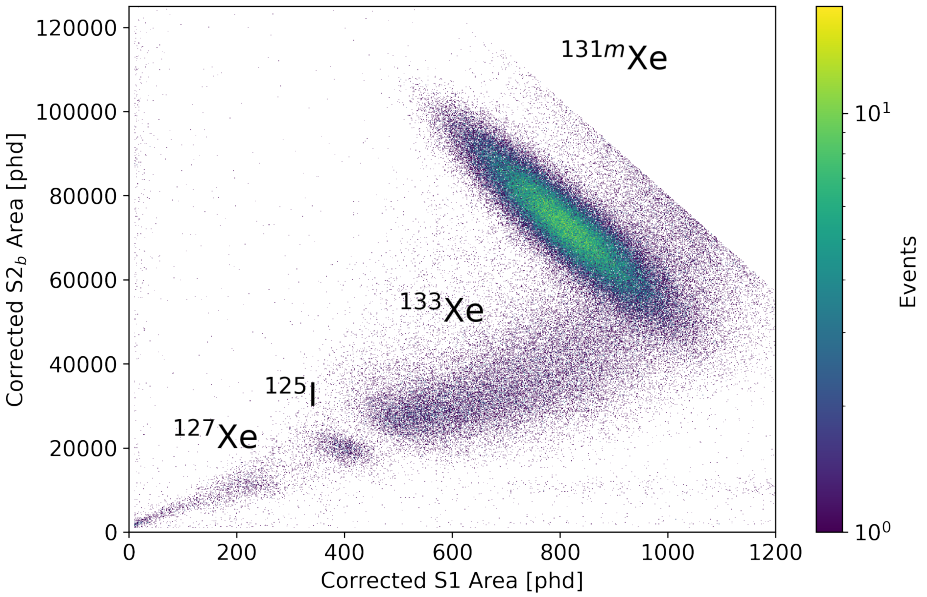

Figure 5.2: Graphical representation of the $S2_b$ vs S1 signals after the calibration that used a deuterium-deuterium neutron source. The correspondent event density is also represented.

energies or by looking at the event density in the previous figure. So, going, once again, from left to right on the x-axis we have the ^{127}Xe, ^{125}I, ^{133}Xe, and ^{131m}Xe isotopes.

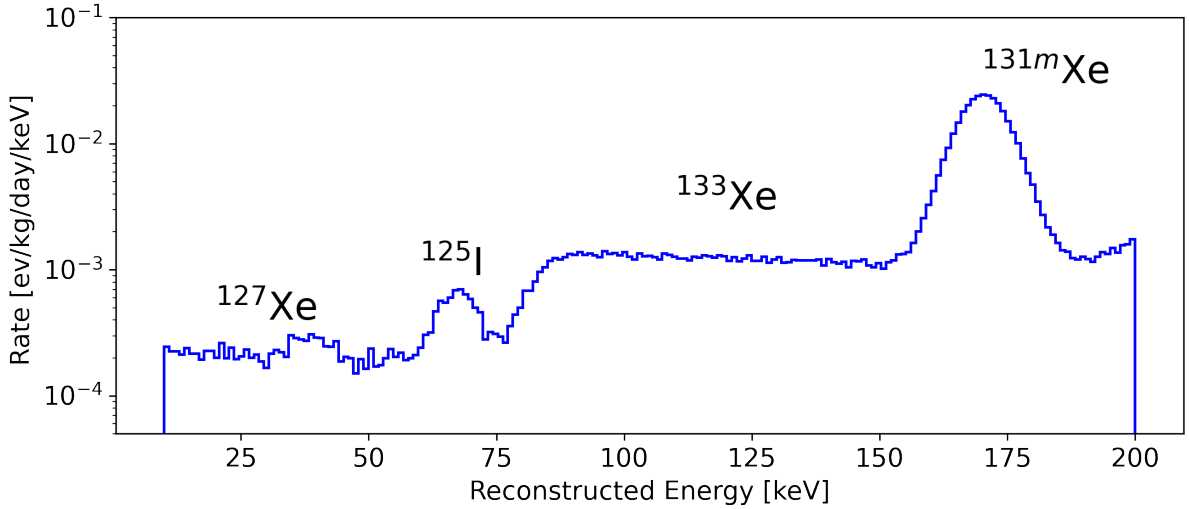

Figure 5.3: Graphical representation of the energy spectrum after the calibration that used a deuterium-deuterium neutron source.

We have now these populations, however, to do this analysis, we have to find and choose the population of the ^{125}I isotope. In this step, we must be very careful and it is required that we know the percentage of this population that is inside of the applied cut. Therefore, the best course of action is to make a 2D Gaussian fit in the S2-S1 parameter space, so that we could know the amount of the population that we were considering. Then, a 2σ cut was applied, so we know that 95.45% of the population was within this

cut, and we could later compensate effectively to estimate the complete population.

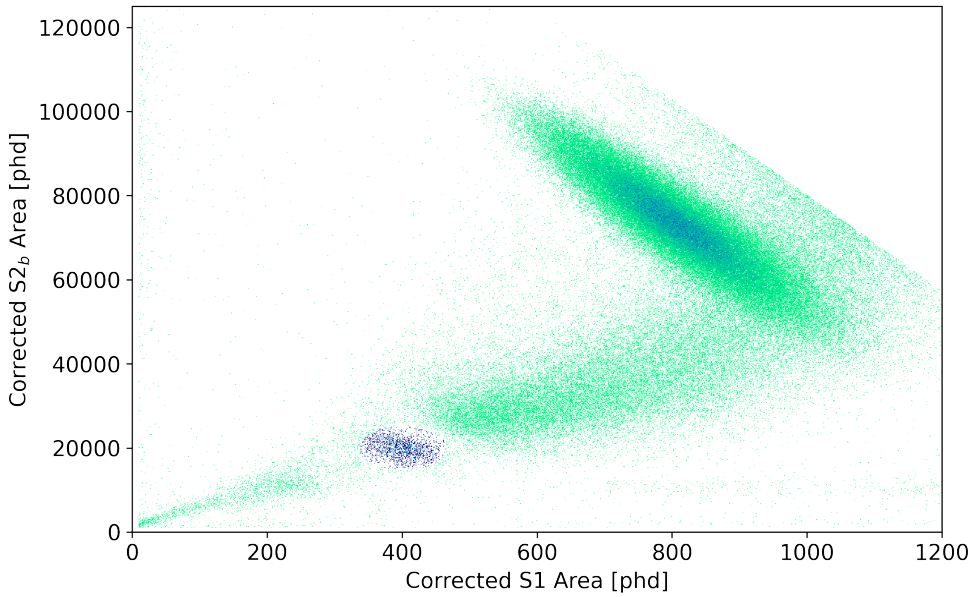

Figure 5.4: Graphical representation of the S2$_b$ vs S1 signal after the calibration alongside of the 2σ cut to the iodine population in blue.

In Figure 5.4, we have the S2$_b$ as a function of S1, with the 2σ cut to the iodine population in blue. It is this population that we are going to use, and we will also compensate for the remaining 4.55% that was excluded from this cut.

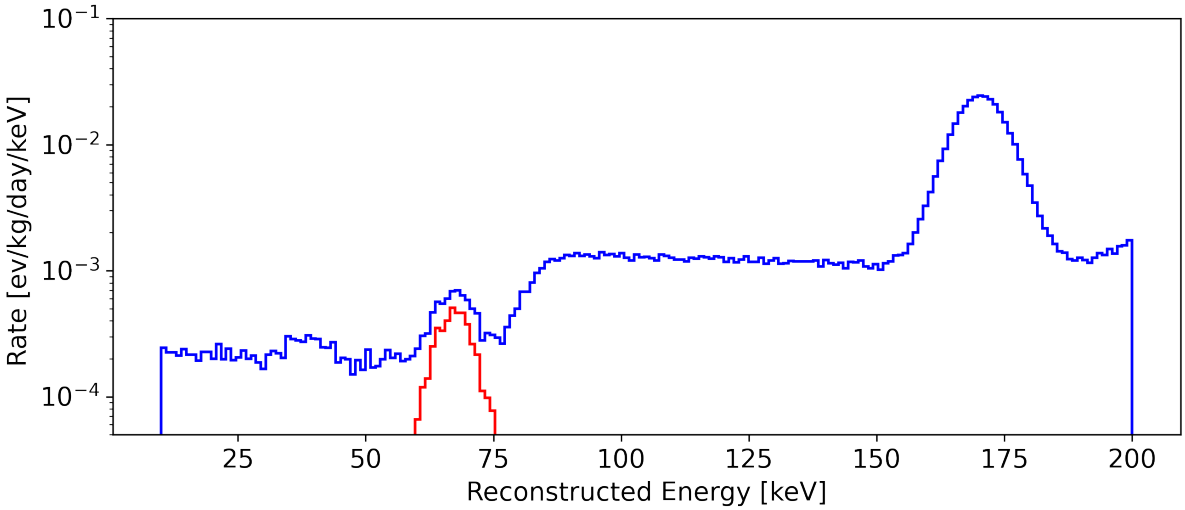

Figure 5.5: Graphical representation of the energy spectrum after the calibration, with the 2σ cut to the iodine population also represented in red.

In Figure 5.5, we have the same cut applied to the energy spectrum, where we have the surviving population in red. As we can see by comparing it with the total spectrum in blue, it identifies almost the totality of the population of the ^{125}I isotope.

5.2.3 Removal time

After correctly identifying the iodine population, we can now obtain the time of removal of this isotope. To achieve this the runs up to 83 days after the calibration were used, and 24-hour intervals were created. The rate for each of these intervals was obtained, normalized to the time the detector was live on each of the intervals.

After that, it is possible to observe how this event rate varied after the calibration, as it is illustrated in Figure 5.6.

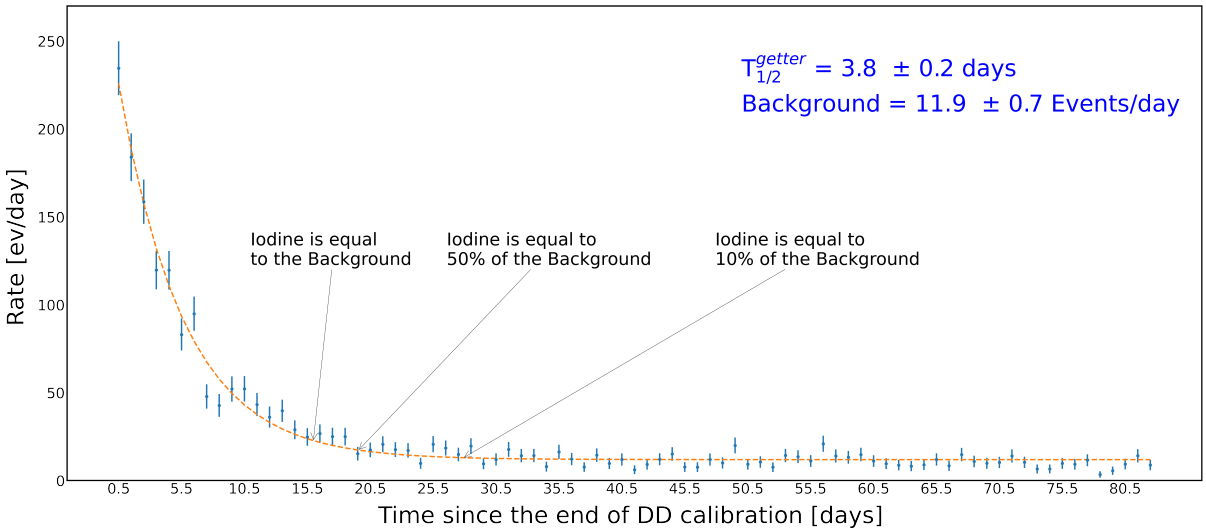

Figure 5.6: Variation of the rate in the ^{125}I isotope region with time after the DD calibration. Exponential fit in orange using the parameters in Equation 5.4, which allowed us to discover the half-life of this removal using the getter and the background present in this region, as we can see in blue. The moments where the ^{125}I isotope is equal to, is 50%, and 10% of the background are also identified, and this happens after 15.5, 19.1, and 27.4 days, respectively.

Since we started taking data right after the end of the calibration, the ^{125}Xe isotope created in this calibration could be still present and not yet decayed entirely into ^{125}I. For that reason, we have to consider two separated terms, one where the ^{125}I isotope is still being created, and the second where it is being removed by the getter and decaying. Therefore, the exponential fit in orange that we observe in Figure 5.6 is given by the following equation:

$$N_{^{125}I}(t) = N_{^{125}Xe}(0)\frac{\lambda_{^{125}Xe}}{\lambda_{^{125}I}^{getter} + \lambda_{^{125}I}^{Natural} - \lambda_{^{125}Xe}}\left(e^{-\lambda_{^{125}Xe}t} - e^{-\left(\lambda_{^{125}I}^{getter}+\lambda_{^{125}I}^{Natural}\right)t}\right) + N_{^{125}I}(0)e^{-\left(\lambda_{^{125}I}^{getter}+\lambda_{^{125}I}^{Natural}\right)t} + background, \quad (5.4)$$

where $N_{^{125}I}(0)$ and $N_{^{125}I}(t)$ are, respectively, the initial and at a time t populations of the ^{125}I isotope, $N_{^{125}Xe}(0)$ is the initial population of the ^{125}Xe isotope, $\lambda_{^{125}Xe}$ and $\lambda_{^{125}I}^{Natural}$ are the decay constants for the xenon and iodine isotopes and take the values 0.98 and 0.01 days, respectively, and, finally, $\lambda_{^{125}I}^{getter}$ is the decay constant associated to the removal of the ^{125}I isotope by the getter.

From that exponential fit, we can obtain the previous unknown variables, and we obtained:

- $N_{^{125}I}(0) = (235.83 \pm 11.01)$ events/day;
- $N_{^{125}Xe}(0) = (0 + 1.64)$ events/day;
- $\lambda_{^{125}I}^{getter} = (0.18 \pm 0.01)$ days^{-1};
- background $= (11.92 \pm 0.72)$ events/day.

From these values, we can conclude the half-life of the removal of the ^{125}I isotope by the getter, which is (3.8 ± 0.2) days. Also, the fit clearly prefers not to have the ^{125}Xe isotope as we initially thought, since the value obtained for the initial population of this isotope is compatible with 0.

In addition, if we plug back the values in Equation 5.4, we can identify the points where the iodine is equal, 50%, and 10% of the background. Using the previous equation again, it is also possible to identify when the ^{125}I isotope is equal to 10% as we saw above, but also 5% and 1% of the background, which happens after 27.4 days, 31.5 days, and 39.4 days, respectively. If we exclude the events up to these points, we will have 6.18, 3.09 and 0.62 iodine events remaining during the rest of the run, respectively.

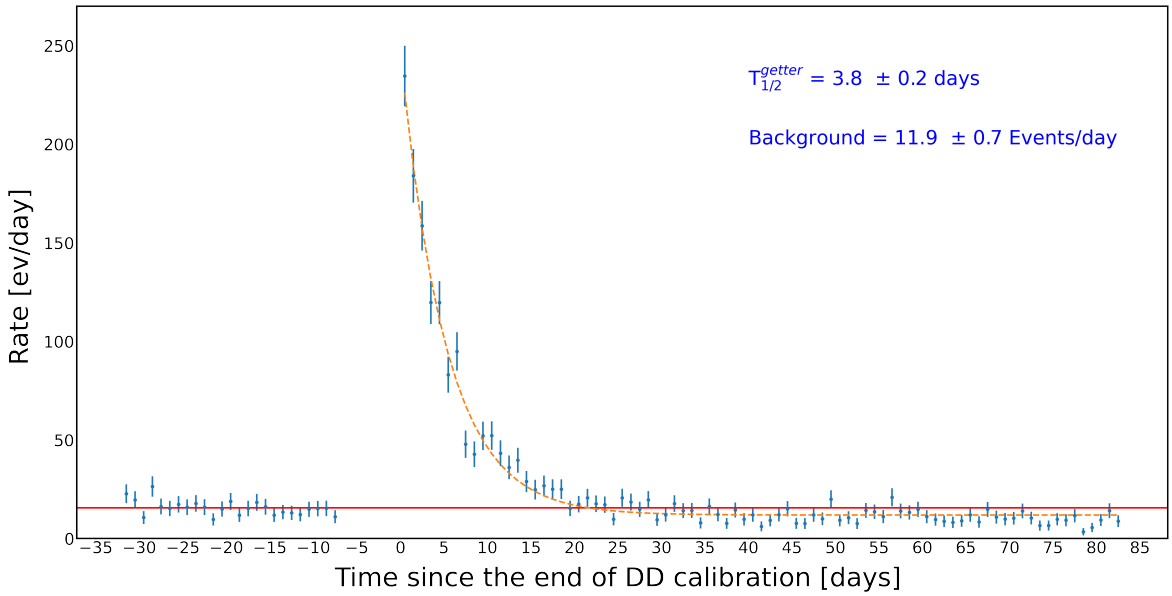

Figure 5.7: Comparison between the rate in the ^{125}I isotope region before and after the DD calibration: the red line is the mean background before that calibration, and it shows that this value is higher than the value obtained for the end part of the events after the calibration.

One important thing that we must do is to see if the background after the calibration corresponds to the background before the calibration and if this was constant. Therefore, we will be able to see if the getter removed all the ^{125}I isotope created during this calibration. To make this comparison, the runs from the 25 days before the start of the calibrations were used, which is illustrated in Figure 5.7.

Using the red line, which is representing the mean value of the background before the calibrations, the background before the calibrations agrees up to a point with the events that occur after the calibration, and after that, the events after the calibration have a lower rate than the events before the calibration. From this, we can conclude that these events before the calibration still had some extra isotopes of the ^{125}I isotope that was created in a previous long calibration campaign that occur during the commissioning in November.

5.2.4 Search period selection

The study analysed during the previous subsection allows us to choose the necessary period we must remove to search for the double electron capture for the KK mode of the ^{124}Xe isotope. However, before we make that choice, we will evaluate the background further, but this time starting at the end of the SR1.

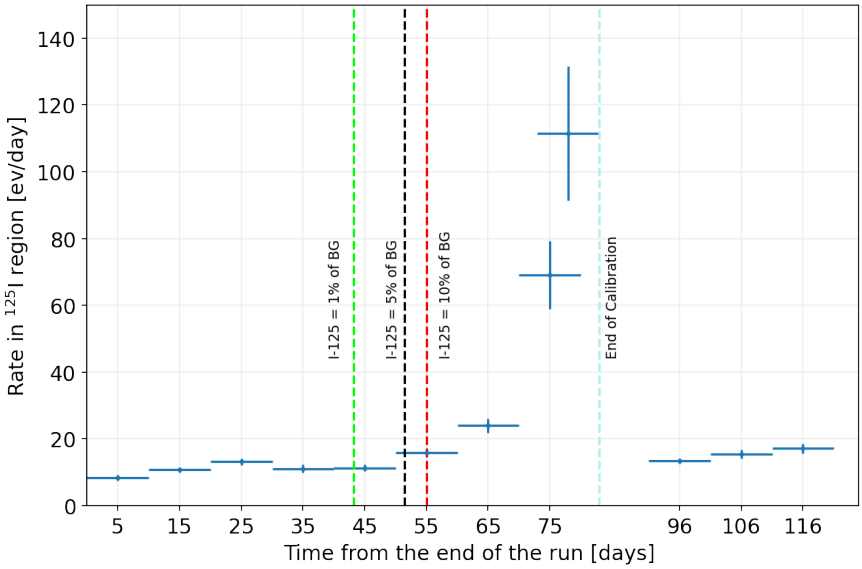

Figure 5.8: Variation of the rate in the ^{125}I isotope region with time for intervals with 10 days starting at the end of SR1. Horizontal bars indicate the bin width, whereas the vertical ones indicate the error associated with the mean background value. The moment where the ^{125}I isotope is 10%, 5%, and 1% of the total background is represented in the red, black, and green dotted lines, respectively, whereas the end of the calibrations is in the blue dotted line.

This study will be done using two distinct approaches. In the first one, we look each time at 10 individual days, where we measured its mean background and the error associated. Doing this to all the data in SR1, we were able to obtain Figure 5.8, which illustrates the variation of the rate in the ^{125}I region as a function of time starting at the end of SR1. The vertical lines represent the error, and the horizontal lines represent the 10 days bin width considered for each interval. It is also represented the beginning of the calibration, as well as the moment where the ^{125}I isotope is 10%, 5%, and 1% of the background, in red, black, and green, respectively.

In the second approach, it was used increasingly larger intervals, we start by considering 10 days, after that 20 days, and so forth until we arrive at 83 days. The results from this study are illustrated in Figure 5.9. In this graphic, we have the same quantities illustrated as in the previous one with the same colour identification.

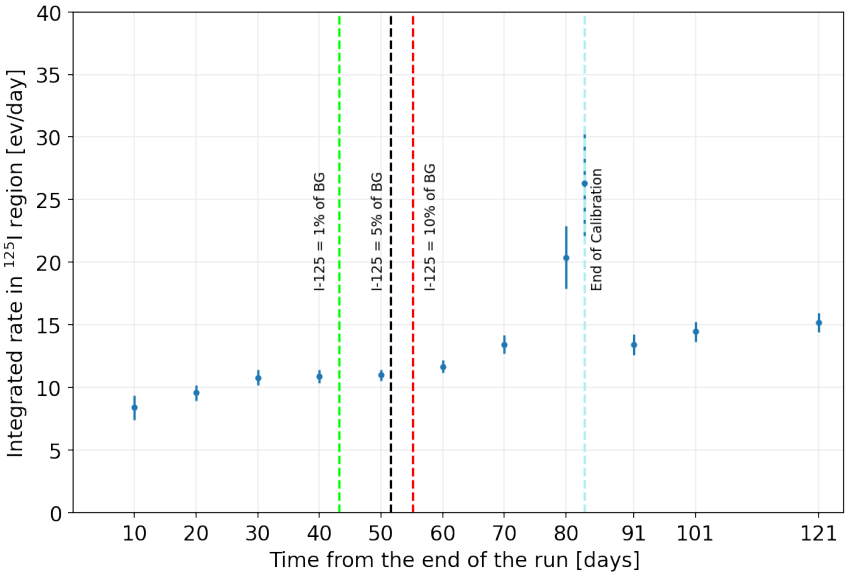

Figure 5.9: Variation of the rate in the ^{125}I isotope region with time for intervals starting with 10 days and increasing 10 days steps until we reach the calibration point, starting at the end of SR1.The vertical lines represent the error associated with the mean background value. The moment where the ^{125}I isotope is 10%, 5%, and 1% of the total background is represented in the red, black, and green dotted lines, respectively, whereas the end of the calibration is in the blue dotted line.

The results obtained in these two studies look to be consistent with the ones obtained in the previous subsection, therefore it seems safe to use the data from the last 50 days of the SR1. Despite this, in Figure 5.9 we observe a slight decline in the rate that could be due to a slow component, however, it was necessary more days at the end of SR1 to analyse this and if that decline in the first bin in Figure 5.8 is real or a fluctuation.

5.3 Position distribution of the ^{125}I isotope in the TPC

In the previous section, we saw how the rate of the ^{125}I isotope changes during the period of the SR1. However, we did not see how it is distributed in the TPC, and this will be our theme for this section. With this study, we intend to analyse a possible circulation problem with the LXe detected during SR1. To select the population of ^{125}I, all the cuts explained in the previous section were also used. Alongside these, all the cuts in order to remove a significant part of the background in our data were also applied, as was also explained in the previous section.

After we had our ^{125}I population selected, we divided our data into 5 distinct intervals, 1 previous to the calibration and 4 others after that calibration. The previous one

covered all selected data from the beginning of SR1 until the calibration, whereas after the calibration were created intervals with data up to 3.5 days, between 3.5 and 14 days, up to 14 days, and finally, after 20 days.

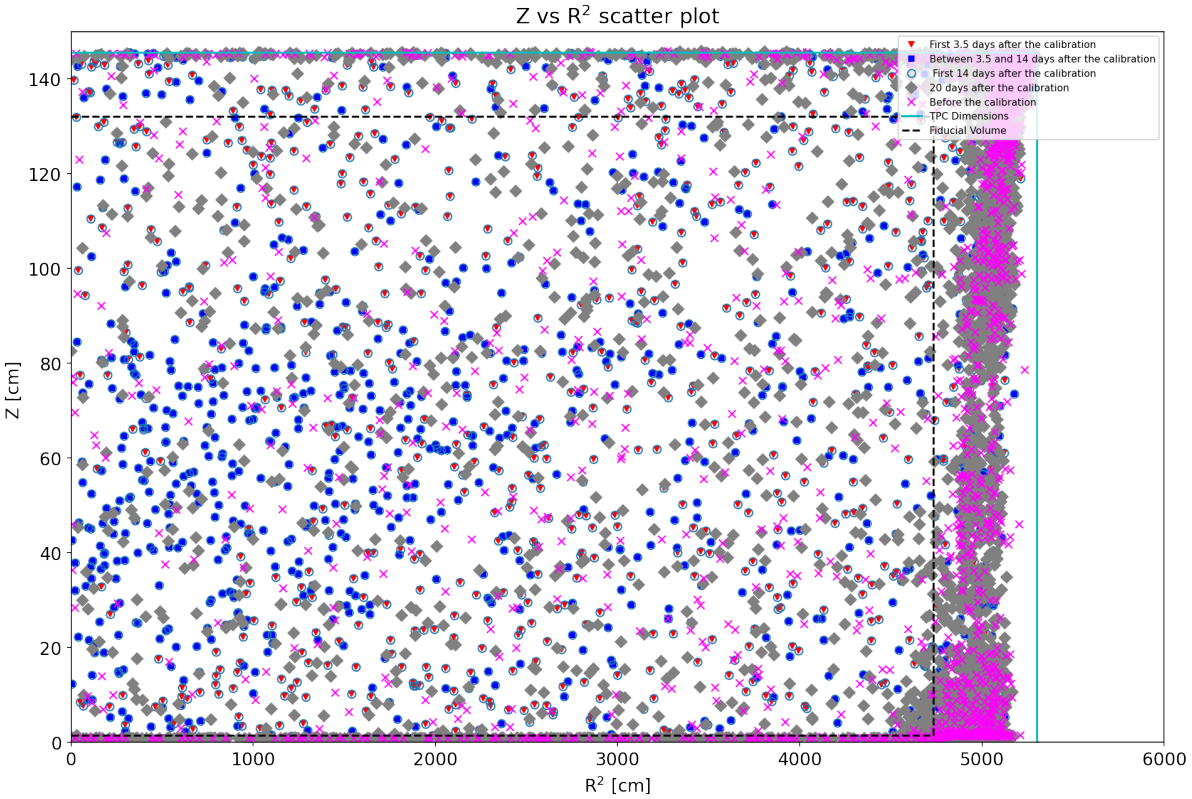

Figure 5.10: Position distribution of the ^{125}I population inside of the detector as a function of the radial and vertical components. The data obtained throughout the SR1 were separated into 5 different intervals. The population obtained previously to the calibration is represented by the magenta crosses, whereas the population for the intervals up to 3.5 days, between 3.5 and 14 days, up to 14 days, and after 20 days is represented by the red down triangle, the blue square, the empty circle, and the grey diamond, respectively. The boundaries of the fiducial volume and the TPC are represented by the dotted black line, and by the blue line, respectively.

In Figure 5.10 these 5 different intervals are shown, where the ^{125}I population previous to the calibration is represented by the magenta crosses and appears to be uniformly distributed. After the calibration, this population for the intervals up to 3.5 days, between 3.5 and 14 days, up to 14 days, and after 20 days is represented by the red down triangle, the blue square, the empty circle, and the grey diamond, respectively. From that figure it is possible to observe a clear concentration of this population in the centre region of the TPC after the calibration, thus corroborating the already known problem of the circulation of the LXe inside the detector. This problem was also observed using other populations, therefore it is well established that it occurred during the SR1 of the LZ experiment, and it is expected to be solved before the start of the following science run.

Furthermore, this figure shows us why it is essential that we use a fiducial volume because, as it is shown, there is a dense concentration of events outside of this fiducial volume near the TPC walls. By doing this, we can remove a significant part of the back-

ground, however, there is still a leakage in the bottom right corner of our fiducial volume. There it is shown a larger concentration of events, nevertheless, this concentration is not due to the circulation problem but to the excess of events outside of this fiducial volume.

Chapter 6

2νECEC decay search for the ^{124}Xe isotope

In this chapter, we arrive at the core of our work, where the search for the double electron capture of the KK mode for the ^{124}Xe isotope is accomplished. This will be a preliminary search, where some approximations regarding the background model in our region were made. However, at that point, I will always explain those approximations.

6.1 Background model

In this preliminary analysis, the background model is based on the background model elaborated by the LZ collaboration for the WIMP search analysis [127]. The model focused on the lower energy regime had to be extrapolated into our region of interest. Comparing simulations of the major background sources, which we will discuss in detail later, with this background model we could predict the rate of the background sources in our region of interest. The first step required for this comparison to be reliable is that the cuts applied by the LZ collaboration in obtaining their background model must be equal to the cuts applied in our analysis. For that reason, beyond those cuts applied in the last chapter, several others were also applied, and these cuts are going to be described in more detail now.

The main focus of these additional cuts is to reduce accidental coincidence events where an isolated S1 and an isolated S2 are accidentally paired, recreating a single-scatter event that would make physical sense. A cut was applied to the width of the S2, since S2 pulses very close to the liquid surface can swallow up the preceding S1 pulses, which would result in isolated S2 pulses that can contribute to accidental backgrounds. Related to these S2 pulses, a form cut was also applied to the S2, because near liquid surface S2 pulses often have characteristically flat tops due to the spontaneous and near-uniform emission of electrons within set time intervals near the extraction region. Therefore, this cut checks if the S2 shape is not too flat. An early peak cut was the next to be applied: extraction region gas events cause merged S1-S2 pulses, however, these are often classified as S2 pulses. This cut eliminates these events using their characteristic shape that typically involves a sharp peak in the early part of the pulse due to the S1 signal. Another cut was also applied because some events have more than one prominent S1 that is identifiable by eye but are not flagged by the interaction finder. This cut checks for other accidental S1 pulses in a given single scatter event and cuts the event

based on the time separation between the S1s. The next cuts events with an excessive area, requiring that the area before the S1 signal and between the S1 and S2 pulses in the event must be less than the area of the S2 signal. It also removes events in noisy waveforms. A cut was also applied to eliminate stinger S1s, where stinger pulses are small S1 pulses that immediately follow Single Electron or S2 pulses. They are caused by electrons that eventually end up on an anode wire. This cut removes events if there is a Single Electron pulse or an S2 pulse within 2000 ns before the S1 pulse. To confirm if a single scatter S2 pulse has a physically reasonable width for its drift time and area, an S2 width cut was applied. Finally, a cut to remove S1 pulses having an abnormally high fraction of light in a single channel was also applied.

The first step is now accomplished; our data has the same cuts applied as the one used for the WIMP search by the LZ collaboration and is expected to be free from spurious events. We have to obtain now our energy resolution, so that we can define a region of interest for our search. For this we need a calibration population in the same energy region as our signal and with a well-defined peak that could be fitted. Therefore, we choose the data within a 5-day period after the DD calibration, since there is a large population of ^{125}I. Applying a gaussian fit to this population, as illustrated in Figure 6.1, we obtain a mean value of 66.3 keV and a sigma of 3.2. Therefore, our energy resolution in this region is equal to 4.8%.

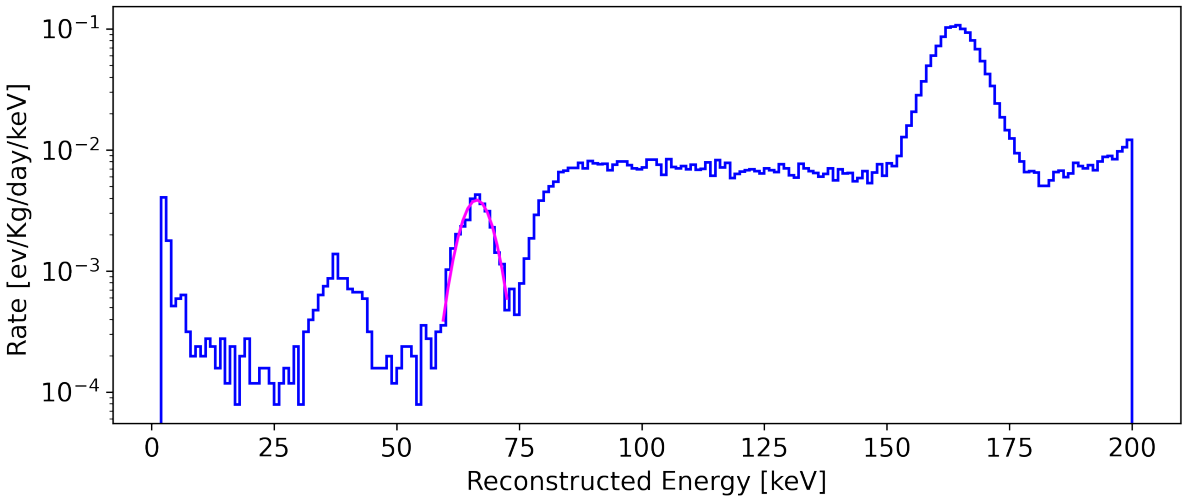

Figure 6.1: Graphical representation of the energy spectrum using the 5-day period after the calibration that used a deuterium-deuterium neutron source, in blue. The gaussian fit to the ^{125}I population is represented in magenta.

Since the detectable energy for the KK mode of the double electron capture for the ^{124}Xe isotope is 64.3 keV, our region of interest will be $\pm 1\sigma$ around this value. Therefore, our region of interest will be comprised between 61.21 and 67.39 keV. We now have all the requirements in order to find out the background events in this region that we are interested in.

In this preliminary search, starting from the background model of the LZ collaboration for lower energies [127] was possible to obtain the background events in our region. The background model is illustrated, in Figure 6.2, for the lower energy regime.

For this search, there are 3 main backgrounds that concern us in our region of interest: the betas from the chains of ^{222}Rn, and ^{220}Rn, and from the ^{85}Kr isotope, the background

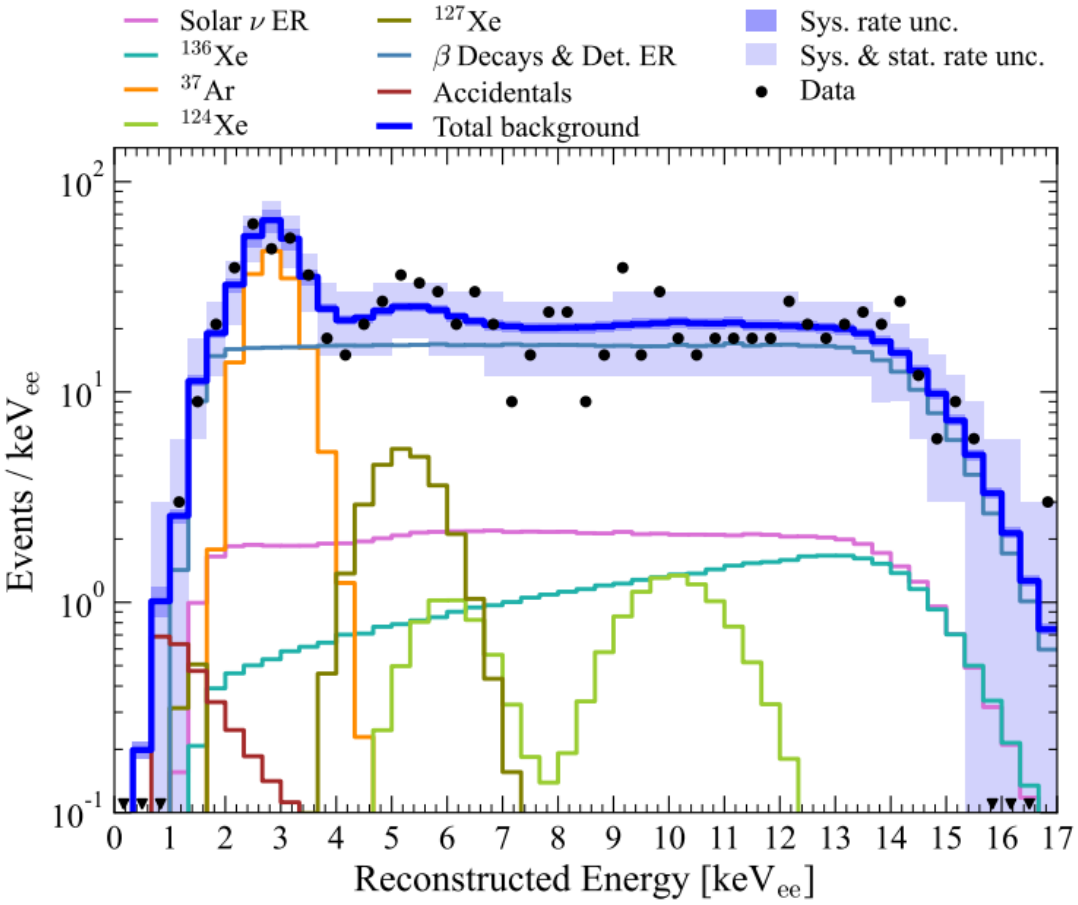

Figure 6.2: Reconstructed energy spectrum of the best fit background model. Data points from the WIMP search are shown in black. The blue line shows the total summed background. Background components are shown in colors as given in the legend. Figure from [127].

from the double beta decay of the ^{136}Xe isotope, and the background coming from the solar neutrinos.

Using all the values measured for the backgrounds during the SR1 of the LZ experiment, it was possible to normalise the simulations. So, for the backgrounds originating from the betas we compared the rate within an interval where this was constant, namely between 6 and 13 keV, with the rate in our simulation. Regarding the uncertainty in this component, it was used the relative error for the beta counting in the region of interest in the WIMP search after the fit. As it is shown in Table VI of the LZ background paper [127], this value was 222 ± 16 events, resulting in a 7.2% relative uncertainty. Therefore, we have a rate of 16.0 ± 1.2 events/keV for the component of the background coming from betas. In our simulations, we obtain a rate equal to 19.5 using 3.26 μBq/kg for the activity of the ^{222}Rn isotope and 144 ppq g/g for the ^{nat}Kr/Xe concentration, for that reason, our spectrum was normalized using a factor of 0.82. Note that in the low energy region the Compton continuum from detector materials gamma rays is indistinguishable from the beta spectra, and thus this normalisation includes both components. Both spectra are flat up to ∼100 keV (see Figure 4.8), therefore the normalisation of the combined spectra is also valid for the energy reason of our search. For the remaining 2

sources, the spectra did not require a re-normalization, since they do not depend on the experiment data.

Having now the background component's spectrum adjusted, we can estimate the events in our region of interest. However, before that, we need to discuss the uncertainties considered for each component. First of all, as was previously discussed, we are going to use 7.2% as the relative uncertainty for the background coming from the betas. The main sources of uncertainty for the solar neutrinos and the double beta decay of the ^{136}Xe isotope are the uncertainty in the neutrino flux and the uncertainty in the half-life of this decay, respectively. There are other smaller contributions that we will disregard in this preliminary estimate. Since, in the solar neutrinos, at these low energies, the flux of neutrinos coming from the proton-proton chain dominates the uncertainty. Therefore, we used the experimental error of 8% measured by the BOREXINO experiment [128]. Regarding the double beta decay of the ^{136}Xe isotope, we have used the half-life measured by the EXO-200 collaboration. Its value is equal to $(2.165 \pm 0.016(\text{stat.}) \pm 0.059(\text{sys.})) \times 10^{21}$ years [129]. These uncertainties were quadratically combined, thus obtaining 6.11×10^{19} years.

In our region of interest, between 61.21 and 67.39 keV, we have a background contribution from the beta component of 97.57 ± 7.03 events. As already mentioned, in this component, we consider the contribution coming not only from the decay chains of ^{222}Rn, and ^{220}Rn, and from the ^{85}Kr isotope but also the contribution coming from the detector components. The second highest contribution comes from the double beta decay of the ^{136}Xe isotope, with $64.80^{+1.88}_{-1.78}$ events. The last contribution considered comes from the solar neutrinos with 16.40 ± 1.31 events in our region of interest. Thus obtaining a value of $178.78^{+7.40}_{-7.38}$ events for the total background. These events are for a 60-day period, corresponding to the live time of the WIMP search. So, this will have to be adapted for the period we use in the search for the double electron capture of ^{124}Xe.

6.2 ^{124}Xe double electron capture (KK mode) search

In the previous chapter, we have seen that it seems safe to use the data from the last 50 days of the SR1 since it is almost free of the ^{125}I isotope. Therefore, we used that data set to perform our search for the KK mode of the double electron capture for the ^{124}Xe isotope. Using the actual live time of the experiment, we obtain that this 50-day interval corresponds to an effective live time of 46.7 days. So, using that data, we can reconstruct the energy spectrum, shown in Figure 6.3. It shows not only the data from the experiment, including the peak for the KK mode of the double electron capture of the ^{124}Xe isotope but also the background coming from the double beta decay of the ^{136}Xe isotope, in blue, the solar neutrinos, in orange, the betas from the ^{222}Rn, the ^{220}Rn, and the ^{85}Kr isotopes, as well as the gammas from the detector materials, in green, and finally, the total background, in red, as well as its statistic and systematic uncertainties. The systematic uncertainty comes from the uncertainties in the fit of the beta spectrum in the WIMP search region, the uncertainties in the half-life of the double beta decay of the ^{136}Xe isotope, and in the uncertainty in the flux of neutrinos coming from the proton-proton chain measured by BOREXINO. For the statistic uncertainty, we considered a Poisson uncertainty in the number of predicted background events in each bin. In magenta, we have a gaussian fit to the excess of events registered above the background model in the region we are searching for this decay, representing the ^{124}Xe signal.

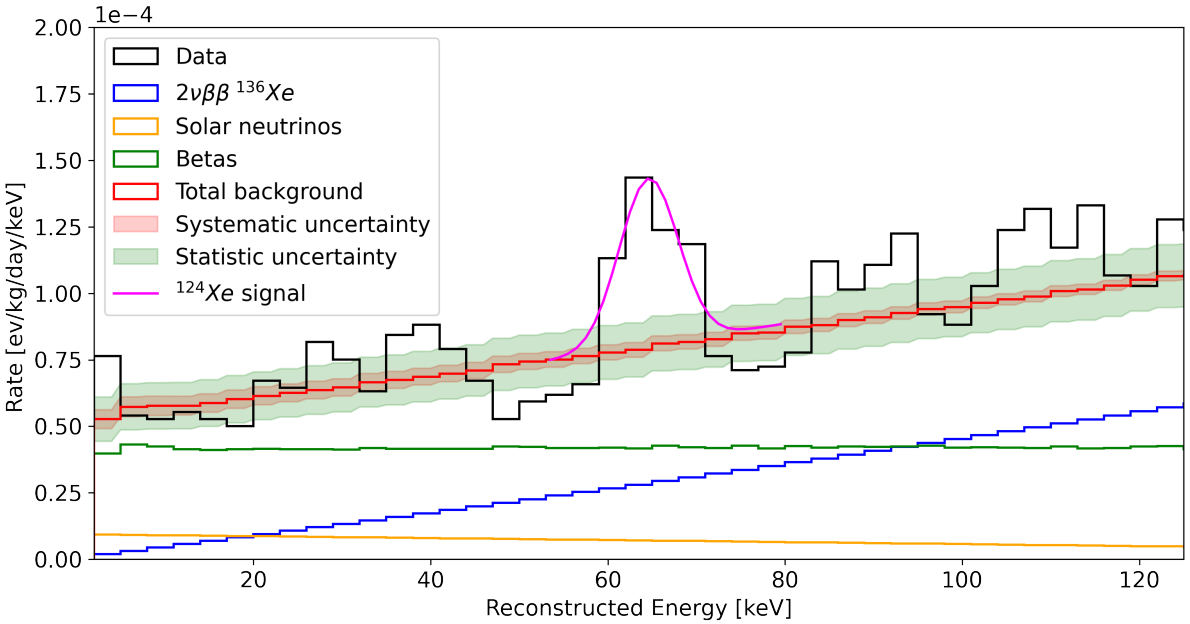

Figure 6.3: Graphical representation of the energy spectrum for the 50-day period. The data are shown in the black line. The background coming from the double beta decay of the ^{136}Xe isotope, in blue, the solar neutrinos, in orange, the betas from the ^{222}Rn, the ^{220}Rn, and the ^{85}Kr isotopes, in green, and finally, the total background, in red, are also shown. The systematic uncertainty in the background is shown by the red band around the mean, and the statistic uncertainty by the green band. The magenta line is a gaussian fit to the excess of events in the signal region, representing the observed ^{124}Xe signal.

However, if we look at the region just outside of our region of interest, we see that our background is overestimated for the data obtained. This may be caused by an efficiency penalty from one or more of the applied cuts, which must be studied in more detail. To be able to perform this preliminary study we decided to scale our background to the observed data. For this, we approximate the total background in the region we are looking to a straight line with the same slope as the background model. This is then combined with a gaussian in a simultaneous fit to the signal and background in this region. This function will be delimited within the region [50,80] keV since outside of that region, we have the signal for the ^{127}Xe isotope on the left, and the signal for the ^{133}Xe isotope on the right. Within this function, the only parameters that are free to change are the amplitude of the gaussian fit and the point where the straight line would intercept the y-axis. The last is kept free since we have to know the scaling factor for our background. The gaussian mean is fixed at the energy of the signal, the standard deviation is estimated using the energy resolution from the fit to the ^{125}I peak, and the slope of the straight line is that of the background model in this region. Integrating the resulting gaussian within that interval, we obtain the number of events for the decay of the KK mode of the double electron capture for the ^{124}Xe isotope, which is equal to 158.5 events.

Integrating now the region underneath the straight line within the same energy interval, we can obtain the value for the background. This value was measured to be

619.1 events. Using now the ratio between the points where the straight line intercepts the y-axis before and after the fit we can find out the scaling factor for our total background, which is equal to 0.8. Scaling the total background we obtain a very similar graphic as the previous one, as we can see in Figure 6.4.

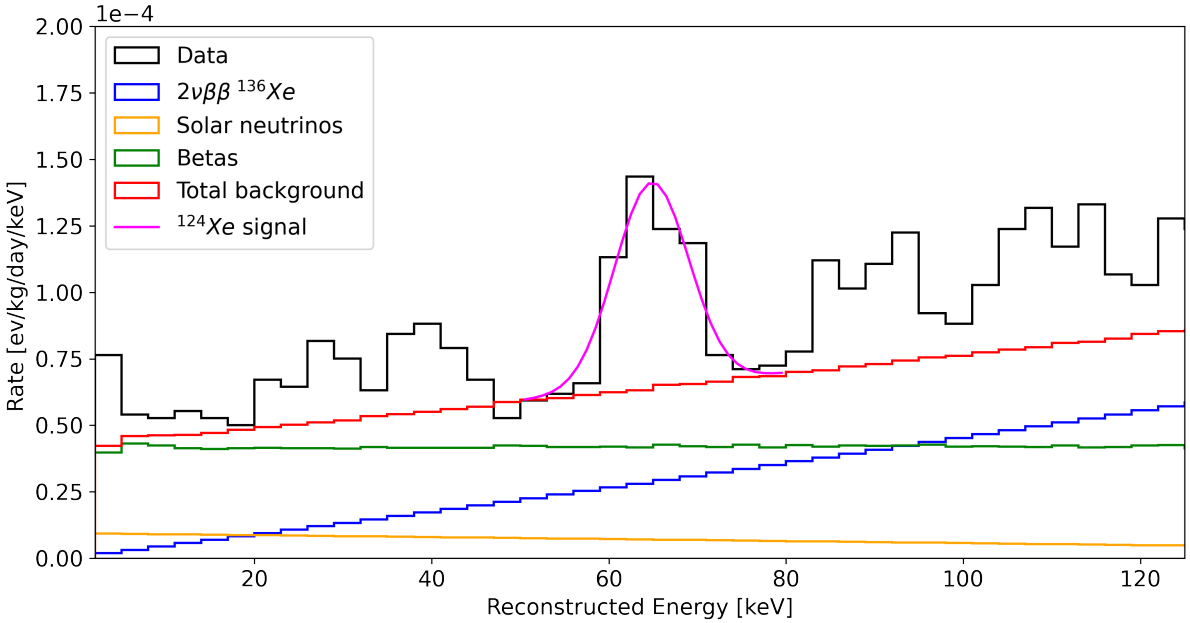

Figure 6.4: Graphical representation of the energy spectrum for the 50-day period. The data are shown in the black line. The background coming from the double beta decay of the ^{136}Xe isotope, in blue, the solar neutrinos, in orange, the betas from the ^{222}Rn, the ^{220}Rn, and the ^{85}Kr isotopes, in green, and finally, the total background scaled with a factor of 0.8, in red, are also shown. The magenta line is a gaussian fit to the excess of events in the signal region, representing the observed ^{124}Xe signal.

In Section 3.3, we showed in Equation 4.5 how to obtain the half-life decay time. Therefore if we plug in all the values and the number of signal events we just estimated, 158.5 events, the value for the half-life of the KK mode of the double electron capture for the ^{124}Xe isotope is:

$$T_{1/2}^{2\nu 2EC} = (1.4 \pm 0.1(stat.) \pm 0.2(sys.)) \times 10^{22} \text{ yr}. \tag{6.1}$$

In doing the calculation of the uncertainty to this value, we only consider uncertainty in the number of events as we disregarded uncertainties in the abundance and in the molar mass of the isotope, and in the fiducial mass. Regarding the systematic uncertainty, we considered three sources of uncertainty. The mean value, the region limitation, and the uncertainty inherent to the gaussian's amplitude. To study the two initial parameters, we change individually their values by one unit, and with we obtain that the uncertainty of number of signal events is 22.0, and 21.7 events, for the upper and lower uncertainties, respectively.

This value agrees very well with the very recently published result by the XENON1T experiment for this decay mode, where they obtained a half-life of
$(1.5 \pm 0.3(\text{stat.}) \pm 0.1(\text{sys.})) \times 10^{22}$ yr [130], and also with the one even more recent from the XENONnT experiment [131]. Therefore, even though this is a preliminary search,

and several approximations were done regarding the background, we should be satisfied with our results.

To finish this search, we need to calculate the statistical significance of our result. For this we are going to use the following expression for a counting experiment with known background [132, 133]:

$$\sqrt{2\left((s+b)\ln\left(1+\frac{s}{b}\right)-s\right)}, \tag{6.2}$$

where s is the number of events for the decay of the KK mode of the double electron capture for the ^{124}Xe isotope and b is the number of background events. The values for these variables are equal to 158.5 events and 619.1 events, respectively. Therefore, if we insert them into that equation, we obtain that our result has a statistical significance of 6.1σ, so we reach the discovery potential.

This result is extraordinary because, in Chapter 4, we predicted that the LZ experiment needed 44 days of exposure to reach the discovery potential for the KK mode of the double electron capture for the ^{124}Xe isotope. So, as a matter of fact, we did reach the discovery potential within the days we had previously predicted, which is remarkable.

Chapter 7

Conclusion

In this thesis, a preliminary search for the KK mode of the double electron capture decay of the ^{124}Xe isotope using data from the SR1 of the LZ experiment is conducted. The work developed for this thesis is divided into two main parts: in the first one, we performed several sensitivity studies to obtain the required time to reach selected statistical significance levels in the different modes of the double electron capture decay of the ^{124}Xe isotope using data from simulations and expected background rates. In the second part, we used the real data from the LZ experiment to search for this decay.

The first sensitivity study was done using the background values measured during the commissioning phase, where the activity for the ^{222}Rn isotope was equal to 5.3 μBq/kg, and the contamination of ^{85}Kr in the used xenon was 123 ppq g/g. From this, we could infer that the LZ experiment would be able to claim an observation and a discovery for the KK mode after 20^{+11}_{-9} and 54^{+17}_{-14} days of exposure, respectively. Whereas in the KL mode, the observation and discovery potentials were expected to be reached after 147^{+79}_{-61} and 416^{+118}_{-110} days of exposure, respectively. Unfortunately, the LL mode is expected to have a much longer half-life decay time, so it is not expected that the LZ experiment reaches either one of these potentials during its 1000 days.

Different from the first study, where the background was considered constant, two distinct others were made, varying only one of the components of the background, and will be denominated from now on as second and third study. In the second study, the background level of the ^{222}Rn isotope was varied, whereas, in the third study, we varied the background from the ^{85}Kr isotope. The results of the second study are presented in Figure 4.13, and considering that the background for the ^{214}Pb isotope, which is the concerning isotope in the ^{222}Rn chain for the background and this chain is not in equilibrium, maintains the value of the best estimate throughout the SR1, 3.2 μBq/kg, LZ is expected to be able to claim a discovery in the KK mode after 44 days of exposure, whereas it could claim an observation and a discovery in the KL mode after 115 and 321 days, respectively. The Third study, where we varied the background from the ^{85}Kr isotope, yet keeping the remaining backgrounds constant, was done using two distinct values for the activity of the ^{222}Rn isotope. It was used firstly the expected value before the beginning of the experiment, 1.8 μBq/kg, and its results are depicted in Figure 4.14. Secondly, it was used the best estimate for this background using the data from the SR1, 3.2 μBq/kg, and the results are illustrated in the same figure. Using the best estimate for the background of the ^{85}Kr isotope, 144 ppq g/g, we obtain that LZ would be able to claim a discovery after 36 days of exposure for the KK mode, while 90 and 246 days are

required to claim an observation and a discovery for the KL mode, respectively, if the background of the ^{222}Rn isotope was equal to the one initially expected. Doing the same approach for the second value, 3.2 μBq/kg, it was obtained that the LZ experiment could claim a discovery after 44 days of exposure for the KK mode, while 117 and 329 days are required to claim an observation and a discovery for the KL mode, respectively.

In the second stage of this work, real data from the LZ experiment to search for the KK mode of the double electron capture decay of the ^{124}Xe isotope. The first step was calculating the necessary time for the getter to remove the ^{125}I isotope, one of the most concerning isotopes for our search. The isotope removal was calculated to be done with a half-life of 3.8 days by the getter. For that reason, we decided to use the last 50 days of the SR1 for our search.

Using data from this period, we search for the KK mode of the double electron capture decay of the ^{124}Xe isotope. That data set has 46.7 days of live time, and we were able to obtain the half-life for this decay, $T_{1/2}^{2\nu 2EC} = (1.4 \pm 0.1(stat.) \pm 0.2(sys.)) \times 10^{22}$ yr, with a statistical significance of 6.1σ. This value agrees very well with the very recently published result by the XENON1T collaboration, where they obtained a half-life of $(1.5 \pm 0.3(\text{stat.}) \pm 0.1(\text{sys.})) \times 10^{22}$ yr [130].

This search was done using only a small portion of data that the LZ experiment will be able to record during its running time. Therefore, this significance is expected to increase even further in the future. Moreover, claiming the discovery of the KL mode is also expected during the full 1000 day duration of the experiment. In conclusion, these searches represent the first steps in an effort for the observation of neutrinoless processes.

Bilbiography

[1] Tom W. B. Kibble. *The Standard Model of Particle Physics*. 2014. DOI: 10.48550/ARXIV.1412.4094. URL: https://arxiv.org/abs/1412.4094.

[2] J. J. Thomson M.A. F.R.S. "XL. Cathode Rays". In: *The London, Edinburgh, and Dublin Philosophical Magazine and Journal of Science* 44.269 (1897), pp. 293–316. DOI: 10.1080/14786449708621070. URL: https://doi.org/10.1080/14786449708621070.

[3] G. Aad et al. "Observation of a new particle in the search for the Standard Model Higgs boson with the ATLAS detector at the LHC". In: *Physics Letters B* (Sept. 2012). DOI: 10.1016/j.physletb.2012.08.020. URL: https://doi.org/10.1016%2Fj.physletb.2012.08.020.

[4] Shashi Chaturvedi and Shyamal Biswas. "Fermi-Dirac statistics: Derivation and Consequences". In: *Resonance* 19 (Jan. 2014). DOI: 10.1007/s12045-014-0006-1.

[5] Standard Model of Elementary Particles. In: *Acessed in 31/05/2022* (2019). URL: https://no.wikipedia.org/wiki/Fil:Standard%5Ctextunderscore%20Model%20%5Ctextunderscore%20of%5Ctextunderscore%20Elementary%5Ctextunderscore%20Particles.svg.

[6] M.I. Ojovan and W.E. Lee. "2 - Nuclear Decay". In: *An Introduction to Nuclear Waste Immobilisation (Second Edition)*. Ed. by M.I. Ojovan and W.E. Lee. Second Edition. Oxford: Elsevier, 2014, pp. 7–19. ISBN: 978-0-08-099392-8. DOI: https://doi.org/10.1016/B978-0-08-099392-8.00002-4. URL: https://www.sciencedirect.com/science/article/pii/B9780080993928000024.

[7] S. Bilenky. "Neutrino oscillations: From a historical perspective to the present status". In: *Nuclear Physics B* 908 (2016). Neutrino Oscillations: Celebrating the Nobel Prize in Physics 2015, pp. 2–13. ISSN: 0550-3213. DOI: https://doi.org/10.1016/j.nuclphysb.2016.01.025. URL: https://www.sciencedirect.com/science/article/pii/S0550321316000353.

[8] John Ellis. "Physics Beyond the Standard Model". In: *Nuclear Physics A* 827.1-4 (Aug. 2009), pp. 187c–198c. DOI: 10.1016/j.nuclphysa.2009.05.034. URL: https://doi.org/10.1016%2Fj.nuclphysa.2009.05.034.

[9] Tom Kibble. "The Standard Model of Particle Physics". In: *European Review* 23 (Dec. 2014). DOI: 10.1017/S1062798714000520.

[10] Subhankar Roy and Sagar Tirtha Goswami. *Leptons and other forces of Nature*. 2021. DOI: 10.48550/ARXIV.2106.06045. URL: https://arxiv.org/abs/2106.06045.

[11] T. Editors of Encyclopaedia Britannica. *Beta decay Encyclopedia Britannica*. 2021. URL: https://www.britannica.com/science/beta-decay.

[12] Koray Karaca. "The construction of the Higgs mechanism and the emergence of the electroweak theory". In: *Studies in History and Philosophy of Science Part B: Studies in History and Philosophy of Modern Physics* 44.1 (2013), pp. 1–16. ISSN: 1355-2198. DOI: https://doi.org/10.1016/j.shpsb.2012.05.003. URL: https://www.sciencedirect.com/science/article/pii/S135521981200041X.

[13] The ATLAS Collaboration. "A detailed map of Higgs boson interactions by the ATLAS experiment ten years after the discovery". In: *Nature* (2022). DOI: https://doi.org/10.1038/s41586-022-04893-w. URL: https://www.nature.com/articles/s41586-022-04893-w.

[14] Johannes Bergstrom. "Predictions of Effective Models in Neutrino Physics". In: *Acessed in 3/10/2022* (2011). URL: https://www.diva-portal.org/smash/get/diva2:426447/FULLTEXT01.pdf.

[15] Quark model of an atom. In: *Acessed in 31/05/2022* (2020). URL: https://onheaven.co.in/2020/11/24/quark-model-of-an-atom/.

[16] Alfredo Macías and Abel Camacho. "On the incompatibility between quantum theory and general relativity". In: *Physics Letters B* 663.1 (2008), pp. 99–102. ISSN: 0370-2693. DOI: https://doi.org/10.1016/j.physletb.2008.03.052. URL: https://www.sciencedirect.com/science/article/pii/S0370269308003936.

[17] Albert Einstein and Robert W. Lawson. "Relativity: the special and general theory". In: *New York: Holt* (1921).

[18] N. Aghanim et al. "Planck 2018 results". In: *Astronomy and Astrophysics* 641 (Sept. 2020), A6. DOI: 10.1051/0004-6361/201833910. URL: https://doi.org/10.1051%2F0004-6361%2F201833910.

[19] P. Athron et al. "Dark matter candidates in the constrained exceptional supersymmetric standard model". In: *Phys. Rev. D* 95 (3 Feb. 2017), p. 035023. DOI: 10.1103/PhysRevD.95.035023. URL: https://link.aps.org/doi/10.1103/PhysRevD.95.035023.

[20] SCIENCE alert. In: *Acessed in 31/07/2022* (2017). URL: https://www.sciencealert.com/scientists-have-concluded-that-the-universe-shouldn-t-really-exist.

[21] CERN. In: *Acessed in 31/07/2022* (2022). URL: https://home.cern/science/physics/matter-antimatter-asymmetry-problem.

[22] M. Sajjad Athar, A. Fatima, and S. K. Singh. *Neutrinos and their interactions with matter*. 2022. DOI: 10.48550/ARXIV.2206.13792. URL: https://arxiv.org/abs/2206.13792.

[23] G. Rajasekaran. "Fermi and the theory of weak interactions". In: *Resonance* 19.1 (Jan. 2014), pp. 18–44. DOI: 10.1007/s12045-014-0005-2. URL: https://doi.org/10.1007%2Fs12045-014-0005-2.

[24] Satoshi Shirai and Masahito Yamazaki. *Is Gravity the Weakest Force?* 2019. DOI: 10.48550/ARXIV.1904.10577. URL: https://arxiv.org/abs/1904.10577.

[25] Western Oregon University. In: *Acessed in 31/07/2022* (2021). URL: https://wou.edu/chemistry/courses/online-chemistry-textbooks/ch103-allied-health-chemistry/ch103-chapter-3-radioactivity/.

[26] Andromeda Geek. In: *Acessed in 31/05/2022* (2015). URL: https://andromedageek.wordpress.com/2015/02/11/neutrinos-part-1-hypothesis-and-discovery/.

[27] "Wolfgang Pauli's letter for the convention in Tübingen 4th of December". In: (1930).

[28] W. Pauli. "The Connection Between Spin and Statistics". In: *Phys. Rev.* 58 (8 Oct. 1940), pp. 716–722. DOI: 10.1103/PhysRev.58.716. URL: https://link.aps.org/doi/10.1103/PhysRev.58.716.

[29] Hans-G Hildebrandt. "Theory and reality on the experiment of Reines/Cowan 1956". In: (July 2015). DOI: 10.13140/RG.2.1.3655.5364.

[30] book reviews. "The singing neutrino Nobel laureate who nearly bombed Nevada". In: *Nature.com* (2021). URL: https://www.nature.com/articles/d41586-021-01318-y.

[31] D.S. Akerib et al. "The LUX-ZEPLIN (LZ) experiment". In: *Nuclear Instruments and Methods in Physics Research Section A: Accelerators, Spectrometers, Detectors and Associated Equipment* 953 (Feb. 2020), p. 163047. DOI: 10.1016/j.nima.2019.163047. URL: https://doi.org/10.1016%2Fj.nima.2019.163047.

[32] Wick Haxton. "The Scientific Life of John Bahcall". In: *Annual Review of Nuclear and Particle Science* 59.1 (Nov. 2009), pp. 1–20. DOI: 10.1146/annurev.nucl.010909.083722. URL: https://doi.org/10.1146%2Fannurev.nucl.010909.083722.

[33] Raymond Davis. "A review of the homestake solar neutrino experiment". In: *Progress in Particle and Nuclear Physics* 32 (1994), pp. 13–32. ISSN: 0146-6410. DOI: https://doi.org/10.1016/0146-6410(94)90004-3. URL: https://www.sciencedirect.com/science/article/pii/0146641094900043.

[34] Arnon Dar and Giora Shaviv. "The solar neutrino problem – an update". In: *Physics Reports* 311.3 (1999), pp. 115–141. ISSN: 0370-1573. DOI: https://doi.org/10.1016/S0370-1573(98)00094-5. URL: https://www.sciencedirect.com/science/article/pii/S0370157398000945.

[35] N. Tolich. "Final results from SNO". In: *J. Phys. Conf. Ser.* 375 (2012). Ed. by Lothar Oberauer, Georg Raffelt, and Robert Wagner, p. 042049. DOI: 10.1088/1742-6596/375/1/042049.

[36] A. Bellerive et al. "The Sudbury Neutrino Observatory". In: *Nuclear Physics B* 908 (July 2016), pp. 30–51. DOI: 10.1016/j.nuclphysb.2016.04.035. URL: https://doi.org/10.1016%2Fj.nuclphysb.2016.04.035.

[37] S. Fukuda et al. "The Super-Kamiokande detector". In: *Nuclear Instruments and Methods in Physics Research Section A: Accelerators, Spectrometers, Detectors and Associated Equipment* 501.2 (2003), pp. 418–462. ISSN: 0168-9002. DOI: https://doi.org/10.1016/S0168-9002(03)00425-X. URL: https://www.sciencedirect.com/science/article/pii/S016890020300425X.

[38] T. Kajita, E. Kearns, and M. Shiozawa. "Establishing atmospheric neutrino oscillations with Super-Kamiokande". In: *Nuclear Physics B* 908 (2016). Neutrino Oscillations: Celebrating the Nobel Prize in Physics 2015, pp. 14–29. ISSN: 0550-3213. DOI: https://doi.org/10.1016/j.nuclphysb.2016.04.017. URL: https://www.sciencedirect.com/science/article/pii/S0550321316300554.

[39] Yoichiro Suzuki. "The Super-Kamiokande experiment". In: *The European Physical Journal C* 79 (Apr. 2019). DOI: 10.1140/epjc/s10052-019-6796-2.

[40] H E Fisk and F Sciulli. "Charged-Current Neutrino Interactions". In: *Annual Review of Nuclear and Particle Science* 32.1 (1982), pp. 499–573. DOI: 10.1146/annurev.ns.32.120182.002435. eprint: https://doi.org/10.1146/annurev.ns.32.120182.002435. URL: https://doi.org/10.1146/annurev.ns.32.120182.002435.

[41] T. Futagami et al. "Observation of the East-West Anisotropy of the Atmospheric Neutrino Flux". In: *Physical Review Letters* 82.26 (June 1999), pp. 5194–5197. DOI: 10.1103/physrevlett.82.5194. URL: https://doi.org/10.1103%2Fphysrevlett.82.5194.

[42] John N. Bahcall. "Neutrinos from the Sun". In: *Scientific American* 221 (July 1969), pp. 28–37.

[43] A. Bellerive et al. "The Sudbury Neutrino Observatory". In: *Nuclear Physics B* (2016). Neutrino Oscillations: Celebrating the Nobel Prize in Physics 2015. ISSN: 0550-3213. DOI: https://doi.org/10.1016/j.nuclphysb.2016.04.035. URL: https://www.sciencedirect.com/science/article/pii/S0550321316300736.

[44] B. Pontecorvo. "Mesonium and antimesonium". In: *Soviet Physics—JETP* 6 (1958), p. 429.

[45] B. Pontecorvo. "Inverse beta processes and nonconservation of lepton charge". In: *Soviet Physics—JETP* 34 (1958), p. 243.

[46] M. Gell-Mann and A. Pais. "Behavior of Neutral Particles under Charge Conjugation". In: *Phys. Rev.* 97 (5 Mar. 1955), pp. 1387–1389. DOI: 10.1103/PhysRev.97.1387. URL: https://link.aps.org/doi/10.1103/PhysRev.97.1387.

[47] Ziro Maki, Masami Nakagawa, and Shoichi Sakata. "Remarks on the unified model of elementary particles". In: *Prog. Theor. Phys.* 28 (1962), pp. 870–880. DOI: 10.1143/PTP.28.870.

[48] B. Pontecorvo. "Neutrino experiments and the question of leptonic-charge conservation". In: *Soviet Physics—JETP* 53 (1967), pp. 1717–1725.

[49] Giles Barr et al. "Particle Physics in the LHC Era chapter 11". In: (Jan. 2016). DOI: 10.1093/acprof:oso/9780198748557.001.0001. URL: https://doi.org/10.1093/acprof:oso/9780198748557.001.0001.

[50] Guido Fantini et al. "The formalism of neutrino oscillations: an introduction". In: (2018). DOI: 10.48550/ARXIV.1802.05781. URL: https://arxiv.org/abs/1802.05781.

[51] S. Westerdale. "Neutrino Mass Problem : Masses and Oscillations". In: (2010). URL: https://web.mit.edu/shawest/Public/8.06/termPaperDraft.pdf.

[52] S. M. BILENKY and C. GIUNTI. "LEPTON NUMBERS IN THE FRAMEWORK OF NEUTRINO MIXING". In: *International Journal of Modern Physics A* 16.24 (Sept. 2001), pp. 3931–3949. DOI: 10.1142/s0217751x01004967. URL: https://doi.org/10.1142%2Fs0217751x01004967.

[53] S Adrián-Martínez et al. "Letter of intent for KM3NeT 2.0". In: *Journal of Physics G: Nuclear and Particle Physics* (June 2016). DOI: 10.1088/0954-3899/43/8/084001. URL: https://doi.org/10.1088%2F0954-3899%2F43%2F8%2F084001.

[54] Joseph Formaggio, André Gouvêa, and R. Robertson. "Direct Measurements of Neutrino Mass". In: (Jan. 2021). URL: https://arxiv.org/pdf/2102.00594.pdf.

[55] Maria Concepcion Gonzalez-Garcia, Michele Maltoni, and Thomas Schwetz. "NuFIT: Three-Flavour Global Analyses of Neutrino Oscillation Experiments". In: *Universe* (Nov. 2021). DOI: 10.3390/universe7120459. URL: https://doi.org/10.3390%2Funiverse7120459.

[56] P. Adamson et al. "Measurement of the Neutrino Mass Splitting and Flavor Mixing by MINOS". In: *Physical Review Letters* 106.18 (May 2011). DOI: 10.1103/physrevlett.106.181801. URL: https://doi.org/10.1103%2Fphysrevlett.106.181801.

[57] X. Qian and P. Vogel. "Neutrino mass hierarchy". In: *Progress in Particle and Nuclear Physics* 83 (July 2015), pp. 1–30. DOI: 10.1016/j.ppnp.2015.05.002. URL: https://doi.org/10.1016%2Fj.ppnp.2015.05.002.

[58] E. Majorana. "Teoria simmetrica dell'elettrone e del positrone". In: *Il Nuovo Cimento* (1937). DOI: 10.1007/BF02961314. URL: https://link.springer.com/article/10.1007/BF02961314.

[59] Michelle J. Dolinski, Alan W.P. Poon, and Werner Rodejohann. "Neutrinoless Double-Beta Decay: Status and Prospects". In: *Annual Review of Nuclear and Particle Science* 69.1 (Oct. 2019), pp. 219–251. DOI: 10.1146/annurev-nucl-101918-023407. URL: https://doi.org/10.1146%2Fannurev-nucl-101918-023407.

[60] Nuclear power. In: *Acessed in 31/07/2022* (2022). URL: https://www.nuclear-power.com/nuclear-power/nuclear-reactions/q-value-energetics-nuclear-reactions/.

[61] M.I. Ojovan and W.E. Lee. "2 - Nuclear Decay". In: (2014). Ed. by M.I. Ojovan and W.E. Lee, pp. 7–19. DOI: https://doi.org/10.1016/B978-0-08-099392-8.00002-4. URL: https://www.sciencedirect.com/science/article/pii/B9780080993928000024.

[62] Assignment Point. "https://assignmentpoint.com/an-electron-shell". In: *Acessed in 31/05/2022* (2022).

[63] William R. Leo. "Techniques for Nuclear and Particle Physics Experiments Chapter 1". In: (1994).

[64] In: *Acessed in 31/07/2022* (2022). URL: https://en.wikipedia.org/wiki/Qvalue(nuclearscience).

[65] "Observation of two-neutrino double electron capture in 124Xe with XENON1T". In: *Nature* 568.7753 (Apr. 2019), pp. 532–535. DOI: 10.1038/s41586-019-1124-4. URL: https://doi.org/10.1038%2Fs41586-019-1124-4.

[66] Warwick. In: *Acessed in 31/05/2022* (2009). URL: https://warwick.ac.uk/study/csde/gsp/eportfolio/directory/crs/phsgbu/research/phdresearch/theory/betadecay/double.

[67] Physics libre texts. In: *Acessed in 31/07/2022* (2022). URL: https://phys.libretexts.org/Bookshelves/Semi-empiricalmassformula.

[68] Ladislav Vala. "Measurement of the 2nubetabeta decay of 100Mo to the excited state in the NEMO3 experiment". PhD thesis. Sept. 2003.

[69] K Zuber. "Double beta decay". In: *Contemporary Physics* 45.6 (2004), pp. 491–502. DOI: 10.1080/00107510412331283540. eprint: https://doi.org/10.1080/00107510412331283540. URL: https://doi.org/10.1080/00107510412331283540.

[70] L. Cardani. "Neutrinoless double beta decay overview". In: *SciPost Physics Proceedings* (Feb. 2019). DOI: 10.21468/SciPostPhysProc.1.024. URL: https://arxiv.org/pdf/1810.12828.pdf.

[71] Frank T. Avignone, Steven R. Elliott, and Jonathan Engel. "Double beta decay, Majorana neutrinos, and neutrino mass". In: *Reviews of Modern Physics* (Apr. 2008). DOI: 10.1103/revmodphys.80.481. URL: https://doi.org/10.1103%2Frevmodphys.80.481.

[72] Sacha Davidson, Enrico Nardi, and Yosef Nir. "Leptogenesis". In: *Physics Reports* 466.4 (2008), pp. 105–177. ISSN: 0370-1573. DOI: https://doi.org/10.1016/j.physrep.2008.06.002. URL: https://www.sciencedirect.com/science/article/pii/S0370157308001889.

[73] V.A. Kuzmin, V.A. Rubakov, and M.E. Shaposhnikov. "On anomalous electroweak baryon-number non-conservation in the early universe". In: *Physics Letters B* 155.1 (1985), pp. 36–42. ISSN: 0370-2693. DOI: https://doi.org/10.1016/0370-2693(85)91028-7. URL: https://www.sciencedirect.com/science/article/pii/0370269385910287.

[74] Peter Arnold and Larry McLerran. "Sphalerons, small fluctuations, and baryon-number violation in electroweak theory". In: *Phys. Rev. D* 36 (2 July 1987), pp. 581–595. DOI: 10.1103/PhysRevD.36.581. URL: https://link.aps.org/doi/10.1103/PhysRevD.36.581.

[75] Pablo F. de Salas et al. "Neutrino Mass Ordering from Oscillations and Beyond: 2018 Status and Future Prospects". In: *Frontiers in Astronomy and Space Sciences* 5 (Oct. 2018). DOI: 10.3389/fspas.2018.00036. URL: https://doi.org/10.3389%2Ffspas.2018.00036.

[76] R. N. et al. Cahn. "White Paper: Measuring the Neutrino Mass Hierarchy". In: (2013). DOI: 10.48550/ARXIV.1307.5487. URL: https://arxiv.org/abs/1307.5487.

[77] University of zurich Physik-Institut. In: *Acessed in 7/06/2022* (2021). URL: https://www.physik.uzh.ch/en/groups/baudis/Research/GERDA.html.

[78] Christian Wittweg et al. "Detection prospects for the second-order weak decays of 124Xe in multi-tonne xenon time projection chambers". In: *The European Physical Journal C* 80.12 (Dec. 2020). DOI: 10.1140/epjc/s10052-020-08726-w. URL: https://doi.org/10.1140%2Fepjc%2Fs10052-020-08726-w.

[79] Christian Wittweg et al. "Detection prospects for the second-order weak decays of ^{124}Xe in multi-tonne xenon time projection chambers". In: *The European Physical Journal C* (Dec. 2020). DOI: 10.1140/epjc/s10052-020-08726-w. URL: https://doi.org/10.1140%2Fepjc%2Fs10052-020-08726-w.

[80] Z. Sujkowski and S. Wycech. "Neutrinoless double electron capture: A tool to search for Majorana neutrinos". In: *Phys. Rev. C* 70 (5 Nov. 2004), p. 052501. DOI: 10.1103/PhysRevC.70.052501. URL: https://link.aps.org/doi/10.1103/PhysRevC.70.052501.

[81] D.S. Akerib et al. "The LUX Experiment". In: *Physics Procedia* 61 (2015). 13th International Conference on Topics in Astroparticle and Underground Physics, TAUP 2013, pp. 74–76. ISSN: 1875-3892. DOI: https://doi.org/10.1016/j.phpro.2014.12.013. URL: https://www.sciencedirect.com/science/article/pii/S1875389214006269.

[82] H.M. Araújo et al. "The ZEPLIN-III dark matter detector: Performance study using an end-to-end simulation tool". In: *Astroparticle Physics* 26.2 (2006), pp. 140–153. ISSN: 0927-6505. DOI: https://doi.org/10.1016/j.astropartphys.2006.05.006. URL: https://www.sciencedirect.com/science/article/pii/S092765050600082X.

[83] D.S. Akerib et al. "The LUX-ZEPLIN (LZ) experiment". In: *Nuclear Instruments and Methods in Physics Research Section A: Accelerators, Spectrometers, Detectors and Associated Equipment* 953 (Feb. 2020), p. 163047. DOI: 10.1016/j.nima.2019.163047. URL: https://doi.org/10.1016%2Fj.nima.2019.163047.

[84] D.S. Akerib et al. "Simulations of events for the LUX-ZEPLIN (LZ) dark matter experiment". In: *Astroparticle Physics* (Feb. 2021). DOI: 10.1016/j.astropartphys.2020.102480. URL: https://doi.org/10.1016%2Fj.astropartphys.2020.102480.

[85] D.S. Akerib et al. "Projected sensitivities of the LUX-ZEPLIN experiment to new physics via low-energy electron recoils". In: *Physical Review D* 104.9 (Nov. 2021). DOI: 10.1103/physrevd.104.092009. URL: https://doi.org/10.1103%2Fphysrevd.104.092009.

[86] Marc Schumann. "Dark Matter Search with liquid Noble Gases". In: (June 2012).

[87] D. S. Akerib et al. "Projected WIMP sensitivity of the LUX-ZEPLIN dark matter experiment". In: *Physical Review D* (Mar. 2020). DOI: 10.1103/physrevd.101.052002. URL: https://doi.org/10.1103%2Fphysrevd.101.052002.

[88] R. Linehan et al. "Design and production of the high voltage electrode grids and electron extraction region for the LZ dual-phase xenon time projection chamber". In: *Nuclear Instruments and Methods in Physics Research Section A: Accelerators, Spectrometers, Detectors and Associated Equipment* (May 2022). DOI: 10.1016/j.nima.2021.165955. URL: https://doi.org/10.1016%2Fj.nima.2021.165955.

[89] V Chepel and H Araujo. "Liquid noble gas detectors for low energy particle physics". In: *Journal of Instrumentation* 8.04 (Apr. 2013), R04001–R04001. DOI: 10.1088/1748-0221/8/04/r04001. URL: https://doi.org/10.1088%2F1748-0221%2F8%2F04%2Fr04001.

[90] B. J. Mount et al. *LUX-ZEPLIN (LZ) Technical Design Report*. 2017. DOI: 10.48550/ARXIV.1703.09144. URL: https://arxiv.org/abs/1703.09144.

[91] Kirill Pushkin. "Direct search for WIMP dark matter particles with the LUX-ZEPLIN (LZ) detector". In: *Nuclear Instruments and Methods in Physics Research Section A: Accelerators, Spectrometers, Detectors and Associated Equipment* 936 (2019). Frontier Detectors for Frontier Physics: 14th Pisa Meeting on Advanced Detectors, pp. 162–165. ISSN: 0168-9002. DOI: https://doi.org/10.1016/j.nima.2018.11.024. URL: https://www.sciencedirect.com/science/article/pii/S0168900218315705.

[92] D S Akerib et al. "Search for two neutrino double electron capture of 124Xe and 126Xe in the full exposure of the LUX detector". In: *Journal of Physics G: Nuclear and Particle Physics* 47.10 (Sept. 2020), p. 105105. DOI: 10.1088/1361-6471/ab9c2d. URL: https://doi.org/10.1088%2F1361-6471%2Fab9c2d.

[93] "Observation of two-neutrino double electron capture in 124Xe with XENON1T". In: *Nature* 568.7753 (Apr. 2019), pp. 532–535. DOI: 10.1038/s41586-019-1124-4. URL: https://doi.org/10.1038%2Fs41586-019-1124-4.

[94] J. D. Lewin and P. F. Smith. "Review of mathematics, numerical factors, and corrections for dark matter experiments based on elastic nuclear recoil". In: *Astropart. Phys.* 6 (1996), pp. 87–112. DOI: 10.1016/S0927-6505(96)00047-3.

[95] J Lindhard et al. "INTEGRAL EQUATIONS GOVERNING RADIATION EFFECTS. (NOTES ON ATOMIC COLLISIONS, III)". In: *Kgl. Danske Videnskab., Selskab. Mat. Fys. Medd.* (Jan. 1963). URL: https://www.osti.gov/biblio/4701226.

[96] N. Ackerman et al. "Observation of Two-Neutrino Double-Beta Decay in Xe-136 with EXO-200". In: *Physical Review Letters* 107.21 (Nov. 2011). DOI: 10.1103/physrevlett.107.212501. URL: https://doi.org/10.1103%2Fphysrevlett.107.212501.

[97] Physics Nist. In: *Acessed in 1/08/2022* (2022). URL: https://physics.nist.gov/PhysRefData/Handbook/Tables/xenontable1.htm.

[98] DOE. In: *Acessed in 1/08/2022* (1999). URL: https://www.nrc.gov/docs/ML2034/ML20343A210.pdf.

[99] Nucleide. In: *Acessed in 29/08/2022* (2014). URL: http://www.nucleide.org/DDEP_WG/Nuclides/Xe-131m_tables.pdf.

[100] Yu. M. Gavrilyuk et al. "Indications of $2\nu2$K capture in 78Kr". In: *Phys. Rev. C* 87.3 (2013), p. 035501. DOI: 10.1103/PhysRevC.87.035501.

[101] A. P. Meshik et al. "Weak decay of Ba-130 and Ba-132: Geochemical measurements". In: *Phys. Rev. C* 64 (2001), p. 035205. DOI: 10.1103/PhysRevC.64.035205.

[102] libretexts. In: *Acessed in 4/08/2022* (1999). URL: https://chem.libretexts.org/Courses/SaintFrancisUniversity/CHEM11%2033AHumanChemistryI28Muino29/133ANuclearChemistry12/13.033AStableandUnst%20ableIsotopes.

[103] E. Aprile et al. "Projected WIMP sensitivity of the XENONnT dark matter experiment". In: *Journal of Cosmology and Astroparticle Physics* 2020.11 (Nov. 2020), pp. 031–031. DOI: 10.1088/1475-7516/2020/11/031. URL: https://doi.org/10.1088%2F1475-7516%2F2020%2F11%2F031.

[104] D.-M. Mei et al. "Early results on radioactive background characterization for Sanford Laboratory and DUSEL experiments". In: *Astroparticle Physics* 34.1 (2010), pp. 33–39. ISSN: 0927-6505. DOI: https://doi.org/10.1016/j.astropartphys.2010.04.003. URL: https://www.sciencedirect.com/science/article/pii/S0927650510000782.

[105] Research Gate. In: *Acessed in 7/08/2022* (2022). URL: https://www.researchgate.net/figure/238-U-and-232-Th-decay-chains-Alpha-b-emitters-are-colored-yellow-teal-For-eachfig1277958988/actions#caption.

[106] D. S. Akerib et al. "The LUX-ZEPLIN (LZ) radioactivity and cleanliness control programs". In: *Phys.J. C 80* (2020). URL: https://doi.org/10.1140/epjc/s10052-020-8420-x.

[107] D. S. et al. Akerib. "Projected sensitivity of the LUX-ZEPLIN experiment to the two-neutrino and neutrinoless double β decays of ^{134}Xe". In: *Phys. Rev. C* 104 (6 Dec. 2021), p. 065501. DOI: 10.1103/PhysRevC.104.065501. URL: https://link.aps.org/doi/10.1103/PhysRevC.104.065501.

[108] L. Baudis et al. "Neutrino physics with multi-ton scale liquid xenon detectors". In: *Journal of Cosmology and Astroparticle Physics* 2014.01 (Jan. 2014), pp. 044–044. DOI: 10.1088/1475-7516/2014/01/044. URL: https://doi.org/10.1088%2F1475-7516%2F2014%2F01%2F044.

[109] J. Billard, E. Figueroa-Feliciano, and L. Strigari. "Implication of neutrino backgrounds on the reach of next generation dark matter direct detection experiments". In: *Phys. Rev. D* 89 (2 Jan. 2014), p. 023524. DOI: 10.1103/PhysRevD.89.023524. URL: https://link.aps.org/doi/10.1103/PhysRevD.89.023524.

[110] J. et al. Aalbers. "First Dark Matter Search Results from the LUX-ZEPLIN (LZ) Experiment". In: (2022). DOI: 10.48550/ARXIV.2207.03764. URL: https://arxiv.org/abs/2207.03764.

[111] GM. et al. Yang. "Analysis of 85Kr: a comparison at the 10-14 level using microliter samples". In: (2013). DOI: 10.1038/srep01596. URL: https://doi.org/10.1038/srep01596.

[112] Philippe Collon, Walter Kutschera, and Zheng-Tian Lu. "TRACING NOBLE GAS RADIONUCLIDES IN THE ENVIRONMENT". In: *Annual Review of Nuclear and Particle Science* 54.1 (2004), pp. 39–67. DOI: 10.1146/annurev.nucl.53.041002.110622. URL: https://doi.org/10.1146/annurev.nucl.53.041002.110622.

[113] nucleide. In: *Acessed in 7/08/2022* (2010). URL: http://www.nucleide.org/DDEP_WG/Nuclides/Pb-214_tables.pdf.

[114] nucleide. In: *Acessed in 7/08/2022* (2010). URL: http://www.nucleide.org/DDEP_WG/Nuclides/Pb-212_tables.pdf.

[115] nucleide. In: *Acessed in 7/08/2022* (2010). URL: http://www.nucleide.org/DDEP_WG/Nuclides/Bi-214_tables.pdf.

[116] Susana Raquel Fonseca Castanheira. "Study of the Sensitivity of the LUX-ZEPLIN Detector to the Double Electron Capture Decay of Xe-124". In: (2021). URL: http://hdl.handle.net/10316/97942.

[117] S. Guatelli et al. "Introduction to the Geant4 Simulation toolkit". In: *AIP Conference Proceedings* 1345 (May 2011), pp. 303–322. DOI: 10.1063/1.3576174.

[118] M. Szydagis et al. "NEST: A Comprehensive Model for Scintillation Yield in Liquid Xenon". In: *JINST* 6 (2011), P10002. DOI: 10.1088/1748-0221/6/10/P10002. arXiv: 1106.1613 [physics.ins-det].

[119] D. S. et al. Akerib. "Calibration, event reconstruction, data analysis, and limit calculation for the LUX dark matter experiment". In: *Phys. Rev. D* 97 (10 May 2018), p. 102008. DOI: 10.1103/PhysRevD.97.102008. URL: https://link.aps.org/doi/10.1103/PhysRevD.97.102008.

[120] Sally Shaw. "Dark Matter Searches with the LUX and LZ Experiments". In: (2016). URL: https://discovery.ucl.ac.uk/id/eprint/1532174/4/SallyShaw_Thesis_UCL_2016.pdf.

[121] Wolfgang A. Rolke, Angel M. López, and Jan Conrad. "Limits and confidence intervals in the presence of nuisance parameters". In: *Nuclear Instruments and Methods in Physics Research Section A: Accelerators, Spectrometers, Detectors and Associated Equipment* 551.2-3 (Oct. 2005), pp. 493–503. DOI: 10.1016/j.nima.2005.05.068. URL: https://doi.org/10.1016%2Fj.nima.2005.05.068.

[122] J. Lundberg et al. "Limits, discovery and cut optimization for a Poisson process with uncertainty in background and signal efficiency: TRolke 2.0". In: *Computer Physics Communications* 181.3 (Mar. 2010), pp. 683–686. DOI: 10.1016/j.cpc.2009.11.001. URL: https://doi.org/10.1016%2Fj.cpc.2009.11.001.

[123] Isotope. In: *Acessed in 10/08/2022* (2022). URL: https://www.buyisotope.com/xenon-124-isotope.php.

[124] E. Aprile et al. "Energy resolution and linearity of XENON1T in the MeV energy range". In: *The European Physical Journal C* 80.8 (Aug. 2020). DOI: 10.1140/epjc/s10052-020-8284-0. URL: https://doi.org/10.1140%2Fepjc%2Fs10052-020-8284-0.

[125] M. Alotiby. "Accurately determining the number of Auger electrons per nuclear decay for medical isotopes". In: (Jan. 2019).

[126] Nucleide. In: *Acessed in 17/08/2022* (2010). URL: http://www.nucleide.org/DDEP_WG/Nuclides/I-125_tables.pdf.

[127] J. Aalbers et al. "A First Backgrounds Model for the LUX-ZEPLIN (LZ) Dark Matter Experiment". In: *Unreleased article* (2022).

[128] O Yu Smirnov et al. "Measurement of Solar pp-neutrino flux with Borexino: results and implications". In: *Journal of Physics: Conference Series* 675.1 (Feb. 2016), p. 012027. DOI: 10.1088/1742-6596/675/1/012027. URL: https://doi.org/10.1088/1742-6596/675/1/012027.

[129] J. B. Albert et al. "An improved measurement of the double beta deacay half-life of Xe-136 with EXO-200". In: *Physical Review C* 89.1 (Jan. 2014). DOI: 10.1103/physrevc.89.015502. URL: https://doi.org/10.1103%2Fphysrevc.89.015502.

[130] E. et al. Aprile. "Double-weak decays of Xe 124 and Xe 136 in the XENON1T and XENONnT experiments". In: *Physical Review C* 106 (Aug. 2022). DOI: 10.1103/PhysRevC.106.024328.

[131] E. et al. Aprile. "Search for New Physics in Electronic Recoil Data from XENONnT". In: (2022). DOI: 10.48550/ARXIV.2207.11330. URL: https://arxiv.org/abs/2207.11330.

[132] Glen Cowan. In: *Acessed in 19/09/2022* (2012). URL: http://www.pp.rhul.ac.uk/~cowan/stat/medsig/medsigNote.pdf.

[133] Robert D. Cousins, James T. Linnemann, and Jordan Tucker. "Evaluation of three methods for calculating statistical significance when incorporating a systematic uncertainty into a test of the background-only hypothesis for a Poisson process". In: *Nuclear Instruments and Methods in Physics Research Section A: Accelerators, Spectrometers, Detectors and Associated Equipment* 595.2 (Oct. 2008), pp. 480–501. DOI: 10.1016/j.nima.2008.07.086. URL: https://doi.org/10.1016%2Fj.nima.2008.07.086.